



UNIVERSITÉ CATHOLIQUE DE LOUVAIN

Study of the stress relieve heat-treatment of additively manufactured AlSi10Mg alloy:

Influence on microstructure and mechanical properties

Dissertation presented by

David DISPAS

and

Arthur BOUILLOT

for obtaining the Master's degree in

Mechanical Engineering

and

Chemical and Materials
Engineering

at Ecole Polytechnique de Louvain (EPL)

Supervisor: Aude SIMAR

Readers: Laurent DELANNAY, Anne MERTENS, Camille VAN DER REST

Academic year 2017-2018

"The gem cannot be polished without friction, nor man perfected without trials."

Confucius

Acknowledgements

Nous tenons tout d'abord à remercier Mme le Professeur Aude Simar, la promotrice de ce travail pour sa direction et ses conseils.

Nous voulons également remercier Mme Camille van der Rest, pour son aide précieuse durant toute l'année.

Nous adressons nos remerciements à Mr le Professeur Pierluigi Mollicone pour son implication pour les tests de contraintes résiduelles via méthode du trou.

Nous exprimons aussi notre gratitude à tous les chercheurs de l'IMAP qui nous ont formés à l'utilisation du matériel ou qui nous ont apporté leur assistance pour les manipulations expérimentales.

Enfin, nous souhaitons remercier nos parents pour leur soutien.

Contents

1	Introduction	1
2	State of the art	3
2.1	Selective laser melting technology	3
2.2	AlSi10Mg alloy	5
2.3	Manufacturing process parameters	7
2.4	As-built mechanical properties	11
2.5	Residual stresses in SLM parts	12
2.6	Post treatments	16
3	Materials and methods	21
3.1	Powder follow-up	21
3.1.1	Sieving	21
3.1.2	Grain size and distribution	21
3.1.3	Composition	21
3.2	SLM manufacturing	22
3.3	Heat treatments	27
3.4	Characterisation	29
3.4.1	Density	29
3.4.2	Microstructure	30
3.4.3	Residual stresses	31
3.4.4	Mechanical properties	32
4	Results	37
4.1	Powder ageing	37
4.1.1	Grain size and distribution	37
4.1.2	Composition	38
4.2	Density and hardness study	40
4.2.1	Optimisation of the SLM parameters	40
4.2.2	Reproducibility	41
4.2.3	Homogeneity along the z direction	48
4.3	In-depth characterisation of the as-built samples	49
4.3.1	Mechanical properties	49
4.3.2	Microstructure	50
4.4	In-depth characterisation of the heat-treated samples	55
4.4.1	Density	55
4.4.2	Hardness	55
4.4.3	Mechanical properties	56
4.4.4	Microstructure	58
4.5	Residual stresses	64

5 Discussion	67
5.1 Powder ageing	67
5.1.1 Grain size and distribution	67
5.1.2 Composition	67
5.2 Density measures assessments	68
5.2.1 Relative optical density image analysis	68
5.2.2 Measures comparison	72
5.3 Density and hardness study	73
5.3.1 Parameters optimisation	73
5.3.2 Reproducibility	75
5.4 Mechanical properties	76
5.5 Microstructure	80
5.5.1 Fractography	80
5.6 Residual stresses	80
6 Conclusion	83
A Batches fabrication and hardness/density measurements details	85
A.1 Process parameters and measured hardness/density properties	85
A.2 Specimens positioning, fabrication orders and sintering times	90
A.2.1 Batch X200-171024	90
A.2.2 Batch X200-180109	91
A.2.3 Batch X200-180220	92
A.2.4 Batch X200-180222	93
A.2.5 Batch X200-180228	94
A.2.6 Batch X200-180313	95
A.2.7 Batch X200-180315	96
A.2.8 Batch X200-180319	97
A.2.9 Batch X200-180417	98
B Tensile properties details	99
B.1 As-built samples	99
B.1.1 Heat treated samples	99
C Extract of Vickers hardness conversion table (HV10)	101
D Procedure for the confidence intervals computation	103
D.1 Apparent relative density	103
D.2 Vickers hardness	104
E Reproducibility study additional plots	105
Bibliography	107

List of Figures

2.1 Selective laser melting technology principle	3
2.2 (a)Research publications on SLM of ceramics, composites and all materials types combined. (b)Research publications on SLM of different metallic materials	4
2.3 Parameters involved in SLM	5
2.4 Phase diagram of Al-Si alloy near the eutectic	6
2.5 Common microstructure of an Al-Si cast alloy	6
2.6 Top view of the microstructure of an Al-Si alloy manufactured by SLM at different scales. Locations of pictures (a), (b) and (c) appear on the top left picture	7
2.7 Process window for SLM of AlSi10Mg, based on the top view of single track scans	8
2.8 Process window for SLM of AlSi10Mg, based on the front view of single track scans	9
2.9 Schematic representation of scanning strategies commonly used in LSM (a) unidirectional long scan track; (b) bi-directional long scan track, and (c) islands	10
2.10 Samples (static tensile) built in different directions: (a) 0° , (b) 45° , and (c) 90°	10
2.11 Measured room-temperature stress-life (S-N) of SLM AlSi10Mg, compared to that of conventional Al 6061. Bending fatigue (rotating beam) at a frequency of 25 Hz.	12
2.12 2D plot of vertical internal stresses measured by the contour method at mid-height, in a vertically-built parallelepiped Inconel718 sample. Vertical stresses are null along the dashed line.	13
2.13 Principal residual stresses as a function of the depth relative to the surface in a AlSi10Mg part. Sample B is built onto an undefined hollow support, while A is not	14
2.14 Non-exhaustive list of residual stresses measurement methods.	15
2.15 Thought process of the contour method analytical step	16
2.16 (a) True strain-stress curves for an AB AlSi12 sample and several heat-treated ones at different temperatures and (b) corresponding mechanical properties	17
2.17 (a) The microstructure of selective laser melted AlSi10Mg after annealing heat treatment and (b) solution heat treatment followed by artificial aging. (c) Schematic representation of the spheroidization process. Si particles gradually grow and concentrate along the cell boundaries, which become less visible	19
2.18 Influence of the cutting parameters on the residual stresses of machined forged aluminium: (a) cutting speed (b) feed per tooth (c) cooling (d) corner radius.	20

3.1	Schematic of the inductively coupled plasma spectroscopy technique set up	22
3.2	ProX DMP 200 printer	23
3.3	Melt pool contours with and without laser compensation (exaggeration)	24
3.4	Laser compensations as a function of the scanning speed (as recommended by the manufacturer)	24
3.5	Dimensions notations for (a) cubic specimens (b) cylindrical specimens (c) parallelepiped specimens (d) tensile specimen	25
3.6	Schematic representation of the hexagonal pattern scanning strategy	25
3.7	Screen capture of the laser scanning pattern for a parallelepiped sample: (a) Layer n (b) Layer $n + 1$ (c) Layer $n + 2$	26
3.8	Screen capture of the laser path for a cylindric sample (a) with contour scanning strategy (b) without contour scanning strategy	26
3.9	Pictures of (a) <i>Labfacility L60 Thermocouple & Fine Wire Welder</i> and (b) <i>Agilent 34972A LXI Data Acquisition/Switching Unit</i>	27
3.10	Temperature curve measured by the T-type thermocouple for the cubic sample annealed at 250°C for 2 hours.	28
3.11	RODIA procedure for specimen X200-180319-cub 1: (a) Original picture of polished section (b) Whole surface isolation with <i>ImageJ</i> (c) Porosities isolation with <i>ImageJ</i>	30
3.12	Implementation of the mean linear intercept method on a SEM picture of an as-built sample.	31
3.13	Schematic representation of the Vickers hardness test	32
3.14	Schematic representation of the tensile test mounting	33
3.15	Tensile stress-strain curve for specimen X200-180417-5 with annotated key features	35
4.1	Evolution of powder size distributions with recycling iterations before ultrasonic treatments.	37
4.2	Evolution of concentration of the recycled powder constituting elements: (a) aluminium mass fraction (b) silicon mass fraction (c) magnesium mass fraction (d) iron mass fraction	39
4.3	Batch X200-171024 samples properties as a function of the energy density: (a) as-built apparent relative density (b) Vickers hardness	41
4.4	Batch X200-180109 scatter plots as functions of the (x,y) position on the manufacturing plate: (a) type ($P=0.75\text{ P}_{max}$; $v_s=1200\frac{\text{mm}}{\text{sec}}$) apparent relative densities (b) type ($P=0.75\text{ P}_{max}$; $v_s=1200\frac{\text{mm}}{\text{sec}}$) hardnesses (c) type ($P=0.75\text{ P}_{max}$; $v_s=900\frac{\text{mm}}{\text{sec}}$) apparent relative densities (d) type ($P=0.75\text{ P}_{max}$; $v_s=900\frac{\text{mm}}{\text{sec}}$) hardnesses	43
4.5	Batch X200-180109 scatter plots as functions of the scan order of (a) the apparent relative densities (b) the Vickers hardnesses	45
4.6	Screen captures of (a) melt pools subdivision from a picture of specimen "8a" (b) <i>ImageJ</i> partitioning from the same picture of specimen "8a" (c) melt pools subdivision from a picture of specimen "8b" (d) <i>ImageJ</i> partitioning from the same picture of specimen "8b"	47
4.7	Histograms of melt pools areas occurrences from <i>ImageJ</i> partitioning of (a) sample "8a" b) sample "8b"	47
4.8	Specimen X200-180417-25 sub-parts and surfaces denomination	48
4.9	Scatter plots of the results for specimen X200-180417-25 surfaces as a function of the vertical position: (a) RODIA based relative density (b) Vickers hardness	49

4.10	Engineering tensile stress-strain curve for specimen X200-180417-2	50
4.11	Microstructure of an as-built sample with the 3 different zones visible, indicating the edge of the melting pool	51
4.12	Fractograph of an as-built tensile sample	52
4.13	"Step-like" structure appearing on the edge of the as-built tensile sample	52
4.14	Close-up shot on the ductile dimples of the as-built fracture surface	53
4.15	View of the smooth fracture surface (on the left). A couple unmelted powder particles are visible	53
4.16	Microstructure damage after rupture. The picture is taken roughly 40 μm below the fracture surface. The loading direction is vertical	54
4.17	Comparison of the heat-treated samples hardness with the as-built.	56
4.18	Engineering stress-strain curves of heat treated tensile specimens of batch X200-180417.	57
4.19	Average stress-strain curves of the tensile specimens of batch X200-180417.	58
4.20	Microstructure of the sample heat-treated at (a) 150°C for 2h and (b) 200°C for 2h	59
4.21	(a) Microstructure of the sample heat-treated at 250°C for 2h and (b) Isolation of the Si particles via the ImageJ software	59
4.22	(a) Microstructure of the sample heat-treated at 300°C for 1h and (b) Isolation of the Si particles via the ImageJ software	59
4.23	(a) Microstructure of the sample heat-treated at 300°C for 2h and (b) Isolation of the Si particles via the ImageJ software	60
4.24	(a) Microstructure of the sample heat-treated at 360°C for 1h and (b) Isolation of the Si particles via the ImageJ software	60
4.25	Fractograph of a 300°C-2h tensile sample	61
4.26	View of the smooth fracture surface of 300°C-2h sample. A couple unmelted powder particles are visible	62
4.27	Close-up shot on the ductile dimples of the 300°C-2h sample fracture surface	62
4.28	View of the smooth fracture surface of 300°C-2h sample. A couple unmelted powder particles are visible	63
4.29	Microstructure damage after rupture of a 300°C-2h sample. The loading direction is vertical	63
4.30	X-Ray diffractogram of a X200-180109 as-built sample	64
4.31	Close-up view on the highest Al peak, for the 5 different samples	64
4.32	Magnitude of principal residual stresses along depth in both the 300°C-2h and the as-built sample, calculated with (a) the power series method, (b) the integral method	66
5.1	5x magnification picture of specimen X200-180319-cub1 and delimitation of the zones A and B	69
5.2	Cumulative porosity fraction bar chart as function of the porosity area from picture of specimen X200-180319 on zone A under (a) 5x magnification (b) 10x magnification	70
5.3	Zone A of specimen X200-180319-cub1: (a) Delimitation from original picture under 5x magnification (b) Porosities isolation from 5x magnification picture (c) Original picture under 10x magnification (d) Porosities isolation of 10x magnification picture	71
5.4	Schematic of a spheric porosity of diameter D in a cubic cell of size length D	71

5.5	Bar chart of the density measurements with the HW (AB and after polishing) and RODIA methods for samples of batch X200-180109	72
5.6	Bar charts of the density measurements with the HW (after polishing) and RODIA methods for samples of (a) batch X200-180319 (b) batch X200-180417	73
5.7	The diagram of keyhole collapse caused by the keyhole instability.	75
5.8	Solubility of hydrogen in aluminium.	76
5.9	Engineering stress-strain tensile curves for as-built specimens of this work (in average) and of <i>Aerostream</i> project	77
5.10	Illustration of the impact of residual stress on the observed tensile stress-strain curve	78
5.11	Schematic representation of dislocation/precipitate interaction under different tempering condition (a) underaged, (b) peak aged	79
5.12	Average ultimate tensile strength for each heat treatment as a function of the Vickers hardness	79
A.1	Specimens positions, order of fabrication and sintering times for batch X200-171024	90
A.2	Photography of the manufacturing plate after completion of the fabrication of batch X200-171024	90
A.3	Specimens positions, order of fabrication and sintering times for batch X200-180109	91
A.4	Photography of the manufacturing plate after completion of the fabrication of batch X200-180109	91
A.5	Specimens positions, order of fabrication and sintering times for batch X200-180220	92
A.6	Specimens positions, order of fabrication and sintering times for batch X200-180222	93
A.7	Photography of the manufacturing plate after completion of the fabrication of batch X200-180109	93
A.8	Specimens positions, order of fabrication and sintering times for batch X200-180228	94
A.9	Photography of the manufacturing plate after completion of the fabrication of batch X200-180228	94
A.10	Specimens positions, order of fabrication and sintering times for batch X200-180313	95
A.11	Photography of the manufacturing plate after completion of the fabrication of batch X200-180313	95
A.12	Specimens positions, order of fabrication and sintering times for batch X200-180315	96
A.13	Photography of the manufacturing plate after completion of the fabrication of batch X200-180315	96
A.14	Specimens positions, order of fabrication and sintering times for batch X200-180319	97
A.15	Photography of the manufacturing plate after completion of the fabrication of batch X200-180319	97
A.16	Photography of the manufacturing plate after completion of the fabrication of batch X200-180417	98

E.1	Average apparent relative density of batch X200-180109 type (P=0.75 P_{max} ; $v_s=1200 \frac{mm}{sec}$) samples as a function of the (a) x coordinate (b) y coordinate	105
E.2	Average Vickers hardness of batch X200-180109 type (P=0.75 P_{max} ; $v_s=1200 \frac{mm}{sec}$) samples as a function of the (a) x coordinate (b) y coordinate	105
E.3	Average apparent relative density of batch X200-180109 type (P=0.75 P_{max} ; $v_s=900 \frac{mm}{sec}$) samples as a function of the (a) x coordinate (b) y coordinate	106
E.4	Average Vickers hardness of batch X200-180109 type (P=0.75 P_{max} ; $v_s=900 \frac{mm}{sec}$) samples as a function of the (a) x coordinate (b) y coordinate	106

List of Tables

2.1	Mechanical properties of SLM built parts and cast + aged parts in literature	11
2.2	Mechanical properties for different plate pre heating temperatures.	11
2.3	Mechanical properties of T6 treated Al6061 alloy	12
2.4	Changes in percentage of the main mechanical properties of SLM AlSi10Mg after T6 treatment, , compared to their as-built state	18
3.1	List of the cubic heat-treated specimens	28
3.2	Polishing routine for Al-Si alloys	30
3.3	Strain limits for interrupted tensile tests of batch X200-180417 specimens	34
4.1	Powder samplings recycling history	38
4.2	Average powder diameter and standard deviation before and after ultrasonic treatment	38
4.3	Composition of the fresh AlSi10Mg powder	38
4.4	Composition of recycled AlSi10Mg powder as a function of the date	39
4.5	Compositions of the chips extracted from samples "5" and "7" from batch X200-171024	40
4.6	Average values and standard deviations for apparent relative densities and hardnesses of the specimens of batch X200-171024	41
4.7	Average values and standard deviations for apparent relative densities and hardnesses of the specimens of batch X200-180109	42
4.8	Minimal and maximal values for apparent relative densities and hardnesses of the specimens of batch X200-180109	42
4.9	Average values and standard deviations for apparent relative densities and hardnesses of the specimens of batch X200-180109, with distinction between the closely packed samples and the others	43
4.10	Minimal and maximal values for apparent relative densities and hardnesses of the specimens of batch X200-180109	44
4.11	Average hardness and relative density measurements for the control cubes of each batch	46
4.12	Summary of the melt pools areas distributions for samples "8a" and "8b"	46
4.13	Relative density and hardness results summary for specimen X200-180417-25 surfaces	49
4.14	Average tensile mechanical properties of the as-built specimens from batch X200-180417	49
4.15	RODIA relative density results for the heat treated cubes	55
4.16	Average tensile mechanical properties of the heat-treated specimens from batch X200-180417	56
4.17	Full width at half-maximum for the cut as-built sample and the 4 cubic heat-treated samples	65

5.1	RODIA results for zones A and B of specimen X200-180317 with 5x and 10x magnification	69
5.2	Optimised manufacturing parameters comparison with literature sources	73
5.3	Vickers hardness results data for aluminium 17-ST alloy.	74
5.4	Relationship between Vickers hardness and ultimate tensile strength	78
A.1	Manufacturing process parameters	86
A.1	Manufacturing process parameters	87
A.1	Manufacturing process parameters	88
B.1	Tensile mechanical properties of the as-built specimens from batch X200-180417	99
B.2	Tensile mechanical properties of the heat treated specimens from batch X200-180417	99
C.1	Extract of Vickers hardness conversion table (HV10)	101

List of Abbreviations

AB	As-Built
AM	Additive Manufacturing
CAD	Computer Aided Design
CI	Confidence Interval
DMLS	Direct Metal Laser Sintering
DMP	Direct Metal Printer
FWHM	Full Width Half Maximum
HAZ	Heat-Affected Zone
HIP	Hot Isostatic Pressing
HPDC	High Pressure Die Casting
HT	Heat Treatment
HW	Hydrostatic Weighing
ICP	Inductively Coupled Plasma
RODIA	Relative Optical Density Image Analysis
SD	Standard Deviation
SEM	Scanning Electron Microscope
SLM	Selective Laser Melting
SR	Stress Relief
US	UltraSounds
UTS	Ultimate Tensile Strength
XRD	X-Rays Diffraction

Symbols

A_0	Initial minimal cross-sectional area	[mm ²]
A_f	Minimal cross-sectional area after fracture	[mm ²]
d_0	Initial minimal diameter	[mm]
d_f	Minimal diameter after fracture	[mm]
D_a	Average particle size	[μm]
E	Young modulus	[GPa]
E_d	Volumetric energy density	[J/mm ³]
F	Force	[N]
h	Hatch space	[μm]
H_v	Vickers hardness	[HV]
\overline{H}_v	Average Vickers hardness	[HV]
L	Extensometer gauge length	[mm]
L_0	Initial extensometer gauge length	[mm]
L_f	Final extensometer gauge length	[mm]
P	Laser power	[W]
p_{O_2}	Oxygen pressure	[mbar]
SD_{HV}	Vickers hardness measures standard deviation	[HV]
$SD_{\rho_{rel}}$	Relative density measures standard deviation	[%]
t	Layer thickness	[μm]
v_s	Scanning speed	[mm/s]
W_a	Specimen dry weight	[g]
W_w	Specimen underwater weight	[g]
ϵ_{eng}	Engineering strain	[%]
$\epsilon_{f,eng}$	Engineering strain at fracture	[%]
$\epsilon_{f,true}$	True strain at fracture	[%]
$\phi_{99\%}$	Laser spot size at the 99% contour	[μm]
λ	Laser wavelength	[nm]
ρ_a	Apparent density	[g/cm ³]
$\rho_{a,rel}$	Apparent relative density	[%]
$\rho_{b,rel}$	Theoretical bulk density	[g/cm ³]
ρ_w	Water density	[g/cm ³]
ρ_{rel}	Relative density	[%]
$\overline{\rho_{rel}}$	Average relative density	[%]
σ_{eng}	Engineering stress	[MPa]
σ_u	Ultimate tensile strength	[MPa]
σ_y	Yield strength	[MPa]

Nous dédions ce travail à nos familles et amis

Chapter 1

Introduction

In highly demanding industries such as aerospace and automotive, cutting edge innovation is a key factor to stay competitive and profitable. Ever more efficient materials must constantly be developed.

Over the last decade, a very promising technology has emerged: selective laser melting (SLM). It presents many appeals compared to other manufacturing processes, such as higher adaptability, better reliability and lower cost. However, a great deal of parameters influence the properties of the manufactured parts. Therefore, substantial research is needed to optimise the process. Studies must be done independently for each material, as the findings for one usually do not transpose to others.

Using SLM with AlSi10Mg and other aluminium alloys has gained in popularity during recent years. The material has several fields of applications due to its light weight and relatively high strength.

Although great progress was made in additive manufacturing of AlSi10Mg, some issues remain unsolved. The ductility and strength of the manufactured parts vary considerably in literature. The causes are not always clearly understood. The inconsistency of the mechanical properties puts a brake on the commercial use of the technique.

The purpose of this thesis is attempt to bring insight on this topic by investigating the residual stresses induced by the manufacturing technique. First, literature will be reviewed et summarized. The manufacturing process parameters will then be presented and optimised so as to maximise density. The effect of heat treatments will finally be discussed, both in terms of mechanical properties and microstructure. A monitoring of the AlSi10Mg powder composition and grain sizes will be carried out as functions of the recycling conditions.

Chapter 2

State of the art

2.1 Selective laser melting technology

Selective laser melting (SLM) - also referred to as direct metal laser sintering (DMLS) - is an additive manufacturing (AM) technique making use of a high power-density laser that locally melts powder materials. When a layer of powder has been melted, a new layer is spread on top of the previous one, and is in turn melted, in order to progressively build a 3D object. The technique is illustrated on figure 2.1 [34]. The materials used include mostly metals but also ceramics and composites. Parts to build must first be drawn in a computer-aided design (CAD) software and broken down in 2D slices, each one corresponding to a powder layer. During the process, the oxygen pressure p_{O_2} must be kept low to prevent the oxidation of the metal. A shielding gas - such as argon - is thus used to fill the build chamber at all time, while p_{O_2} is monitored.

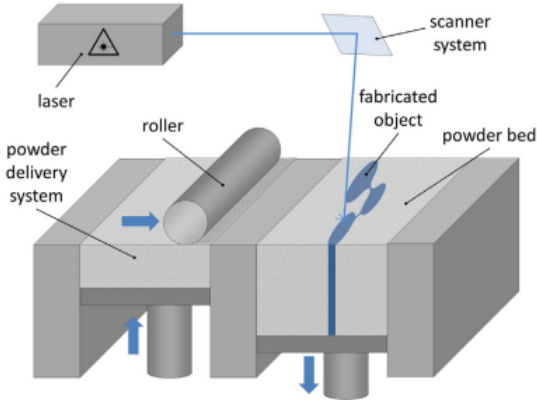


FIGURE 2.1: Selective laser melting technology principle (from Leitz et al., 2017 [34]).

SLM is still a young technology. Its popularity only increased significantly over the last decade, as depicted by figure 2.2. Works concerning AlSi10Mg began to emerge noticeably in 2014. The technique usage spread rapidly in many sectors: biomedical, heat exchangers, aerospace and automotive - to name just a few [70]. This is due to the numerous appeals of SLM compared to the other technologies, including:

- Geometrical flexibility: parts can be designed with thin walls or even with hidden cavities and/or channels. This offers promising prospects regarding light-weight potentials for parts solicited mechanically [38];
- Increased reliability of the parts [21];
- Reduced equipment costs [25];
- Better operational efficiency: the manufacturing is quick and easy which reduces time-to-market as well as assembly times and capital tied up in stocks [25];
- Individual production facilitation [21];
- Reduced material waste and better energy usage: the process is environmentally friendly as a whole [21].

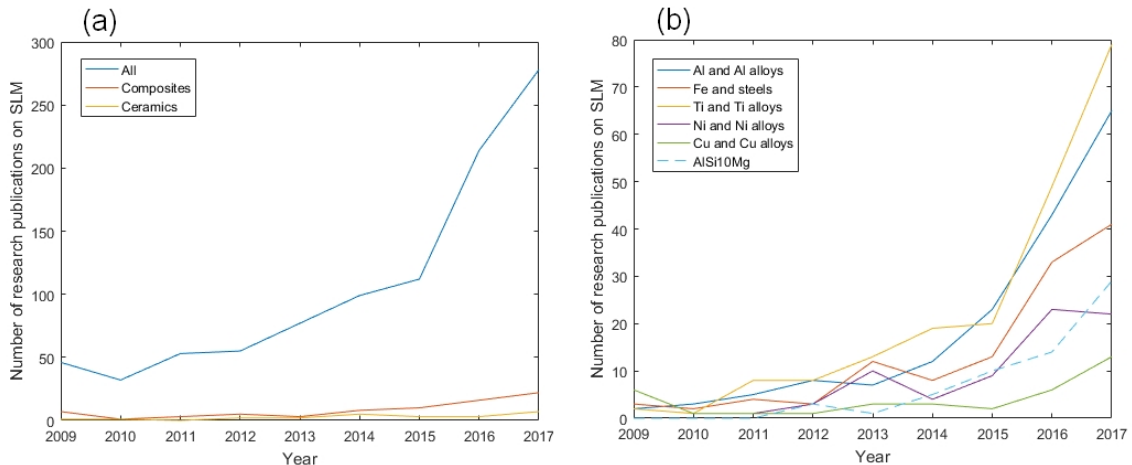


FIGURE 2.2: (a)Research publications on SLM of ceramics, composites and all materials types combined. (b)Research publications on SLM of different metallic materials. Data are derived from the research publications on SLM, LaserCusing and DMLS existing on ScienceDirect website.

The properties of parts produced through SLM stem from the coupled effects of a great deal of parameters (see figure 2.3) [5]. Results are very sensitive to their variations. The process parameters must thus be monitored thoroughly. This complicates the search for their optimisation, still not fully resolved for aluminium alloys.

In recent years, works aiming at facing this challenge multiplied. The minimisation of the porosity is at the center of attention. It is indeed closely related to the quality of the mechanical properties. As porosity contributes to lowering the load-bearing surface, it reduces the apparent material strength. It was also observed to have a critical influence on the fatigue life of the produced parts. Their lifetime is especially diminished if the values of pores amount and size go beyond a certain threshold [12]. Studies investigating the effects of various parameters on the AlSi10Mg manufacturing through SLM abound in the literature.

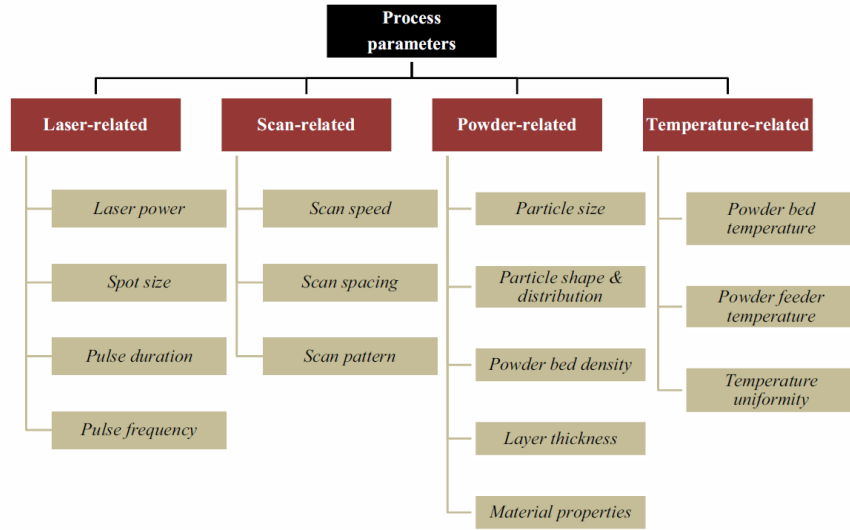


FIGURE 2.3: Parameters involved in SLM (from Aboulkhair et al., 2014 [5]).

2.2 AlSi10Mg alloy

AlSi10Mg is a popular casting alloy. It is well known for its high strength-to-density ratio, thermal properties and post-processing flexibility. This makes AlSi10Mg a material of choice in automotive, aerospace, automation, chemical and food industries [32]. Specific applications contain housings, ductwork, engine parts, production tools and molds, both for prototyping and manufacturing purposes. [41]. Processing the alloy with SLM is quiet easy due to the small difference between its solidus and liquidus temperatures [32]. Nevertheless, high laser power is needed to compensate the energy losses due to the high reflexivity (91%) and the fast heat dissipation resulting from the consequent thermal conductivity ($146 \frac{W}{mK}$) [3].

The most important property of the alloy is its composition. As it can be observed on the phase diagram of figure 2.4, and by assuming that the small concentrations of magnesium and impurities do not displace too much the diagram, AlSi10Mg has an hypo-eutectic concentration. Thus, the first solid to form during cooling is made of $Al - \alpha$ phase, followed by the formation of an eutectic compound. The addition of magnesium also allows the precipitation of Mg₂Si which increases the strength of the material, without affecting significantly the other mechanical properties [32].

Nevertheless, knowing the composition is not sufficient to predict the microstructure of the alloy. It depends heavily on the manufacturing process. As shown in figure 2.5, casting results in the formation of lamellar precipitates of Si-phase, measuring several tens of micrometers and floating in an Al matrix. In the first image of figure 2.6, we can observe a completely different macrostructure for a SLM manufactured sample at the same scale as the cast alloy. It consists of a stacking of successive scan tracks, that solidified following the laser passage, layer after layer. Its exact shape is dictated by the various parameters of the SLM process, which will be discussed in the Section 2.3.

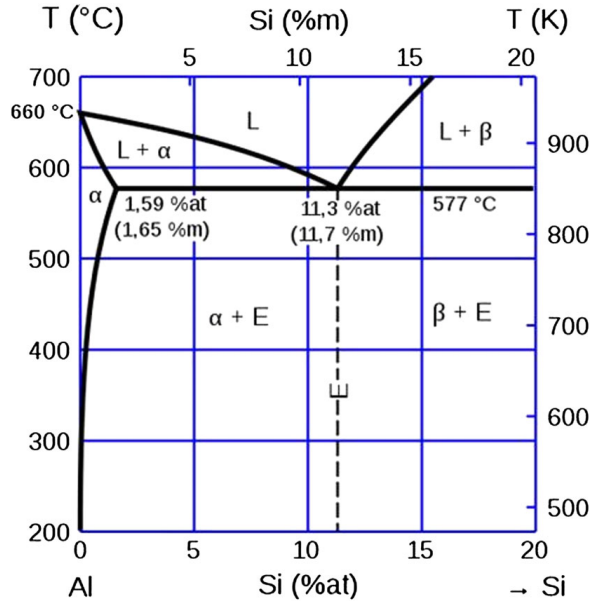


FIGURE 2.4: Phase diagram of Al-Si alloy near the eutectic (from Rosenthal et al., 2014 [52]).

By zooming in, we see that those scan tracks are characterised by a very fine microstructure: cells of Al, measuring $1\mu\text{m}$ or less, separated by a spider web-like network of Si. Those were the two only phases that were detected with XRD by Thijss et al. (2013) [57]. This fineness is due to the intense thermal gradients appearing in the melt pool left behind the laser: they allow a particularly fast cooling (up to 10^5 K/s [49]) and solidification, which do not let time for alloying elements to diffuse over much distance. However, this microstructure is not homogeneous across the whole part: the section of a scan track can be separated in 3 roughly concentric zones.

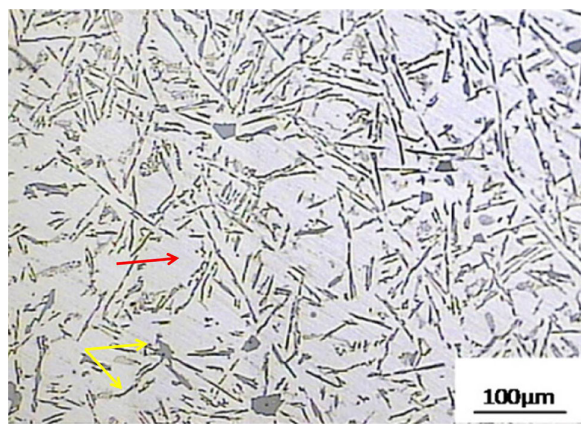


FIGURE 2.5: Common microstructure of an Al-Si cast alloy, with the red arrow pointing to the Al matrix, and the yellow one to the Si lamellae (from Wang et al., 2012 [66]).

First, there is the fine zone which is the result of the melt pool core solidification. The cellular dendrites start to grow from the melt pool edge resulting in elongated

cells, and converge towards the centre where they are more isotropic. Around it, near the boundary, lies the coarse zone with larger cells and thicker lamellae. According to Uzan et al. (2017) [62], the difference of microstructure is simply due to lower solidification rates ; the hot zones in the previous layer reduce the temperature gradient. Just outside the melt pool, in previously solidified tracks, lies a heat-affected zone(HAZ). Although it remains at least partially solid during the previous laser passage, temperature rises enough to allow Si to diffuse and coarsen into globular particles, breaking the cellular structure. It is from this specific microstructure that arise all the mechanical properties of the part, which will be presented in Section 2.4.

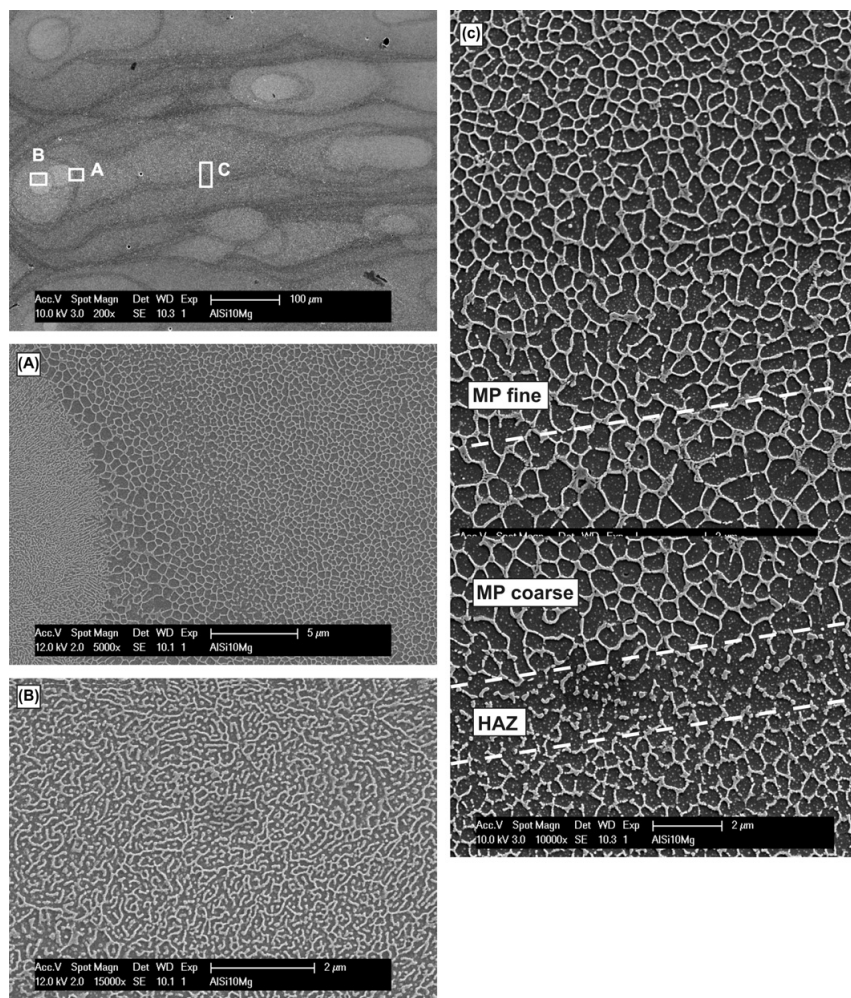


FIGURE 2.6: Top view of the microstructure of an Al-Si alloy manufactured by SLM at different scales. Locations of pictures (a), (b) and (c) appear on the top left picture (from Thijs et al., 2013 [57]).

2.3 Manufacturing process parameters

Let us now investigate the influence of the parameters on the properties of AlSi10Mg parts manufactured with SLM. The analysis of the paired impacts of the laser power P and scan speed v_s provides a first insight. As depicted by figures 2.7 and 2.8, low

P and high v_s lead to an insufficient energy input to melt the powder and re-melt the substrate, which causes the formation of droplets [32]. The opposite leads to good penetration but also to distortions and irregularities. A trend to use both high P and v_s rose in accordance with these findings. Doing so has the advantage to increase productivity. However, it also has multiple downsides including a decrease of the surface quality due to balling, excessive spatter, and an augmented gas induced porosity [44]. Therefore, a trade-off must be found.

A popular approach is to regroup multiple operating parameters into one; the volumetric energy density E_d . It is estimated through the following formula:

$$E_d = \frac{P}{v_s h t}$$

where t is the layer thickness and h is the hatch space. Maximisation of ρ_{rel} is obtained for $E_d \simeq$ ranging from 40 to 90 [$\frac{J}{mm^3}$] [61]. Read et al. obtained a minimal porosity with $E_d \simeq 60$ [$\frac{J}{mm^3}$] [50]. However, choosing a right E_d is insufficient and other phenomena, such as melt pools overlapping, should be considered [56]. Very few studies were carried out to optimize h and t independently. Their values lie generally in the intervals [50 ; 200] [μm] and [20 ; 60] [μm], respectively [3, 12, 32, 44]. It was observed that for $t = 30$ [μm], an optimal set of parameters values in terms of density is $P = 200$ [W], $v_s = 1400$ [$\frac{mm}{s}$] and $h = 105$ [μm] [32]. The apparent relative density $\rho_{a,rel}$ was then above 99.5 [%], considering the theoretical bulk density ρ_b to be equal to 2.68 [$\frac{g}{mm^3}$].

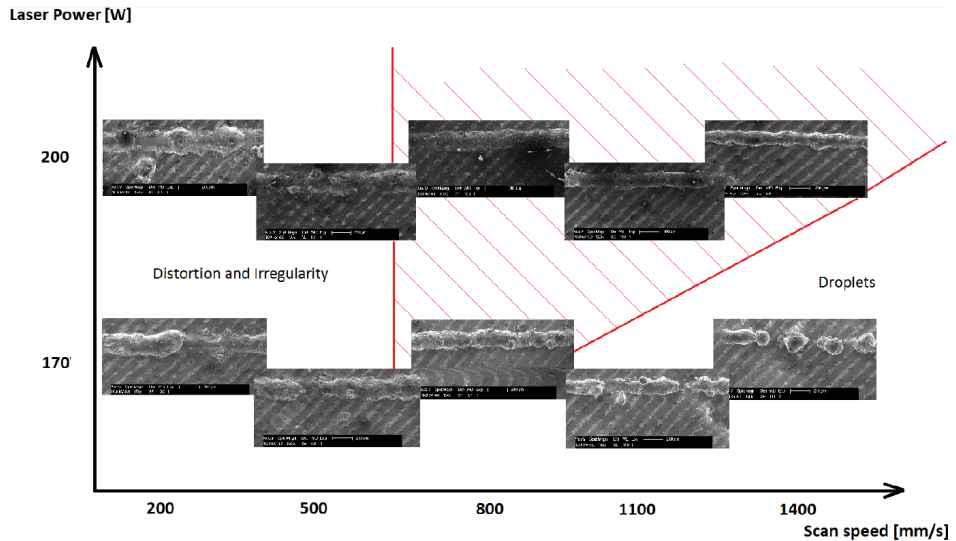


FIGURE 2.7: Process window for SLM of AlSi10Mg, based on the top view of single track scans (from Kempen et al., 2011 [32]).

The other process parameters will be covered for the sake of completeness. Let us first look into the particle-related parameters. The particle size D_a of the powder should be as small as possible to ensure a good flowability and allow for thin layers [32]. Typical values for mean particle size stretch from 15 to 50 [μm] but are more often at around 30 [μm] [12, 32, 45, 62]. The size distribution is more delicate to outline. On one hand, wider distributions often generate better bed density, parts with

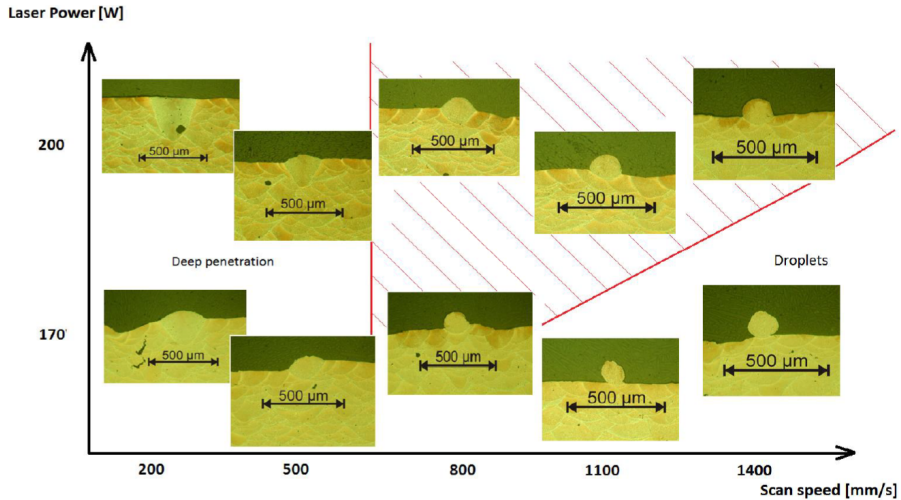


FIGURE 2.8: Process window for SLM of AlSi10Mg, based on the front view of single track scans (from Kempen et al., 2011 [32]).

higher density and better surface finish. On the other hand, narrower ones usually provide better flowability and parts with better strength and hardness [39]. In most cases, a middle ground between the two should be sought. In SLM applications, powder is often successively recycled multiple times. This leads to their progressive contamination with moisture, which causes an increase of hydrogen porosity in the produced parts [68]. The problem can be overcome by drying the powder or using fresh one. Unfortunately - in the case of aluminium alloys - no findings were made regarding the prediction of a threshold at which one should take action [6].

The choice of scan pattern has great importance. There exist a few different strategies. The common ones use unidirectional, bidirectional or islands patterns (see figure 2.9). The scan direction(s) should always be rotated between successive layers to favorise isotropy, especially in the unidirectional case since it causes height variations along a layer [3]. The islands pattern is based on a decomposition in small domains with short scanning tracks. Two usual strategies can be distinguished among this group: the chessboard and the hexagonal one. A study proved the superiority of an island pattern over a bidirectional one in terms of both ultimate tensile stress σ_u and strain at fracture ϵ_f for a 316L stainless steel-Inconel 718 material [71]. It was also shown that it was possible to manufacture pure titanium samples without cracks using an island pattern, and not with a bidirectional one [36]. This is seemingly due to the greater accumulation of internal stresses and to the weaker interlayer bounding in the second case.

Furthermore, dual scanning strategies were proven to be effective. For example, a pre-scan with low E_d can flatten the powder bed before it is consolidated, which leads to a reduction of porosity [44]. It was also shown that scanning the contour of the part being built at lower E_d can better the surface roughness for AlSi12Mg [48]. One should note too that the final properties of the part can strongly depend on the building direction (see figure 2.10) [15]. Further properties comparison is provided in section 2.4.

Other laser-related parameters - the spot size and the pulse properties - can also

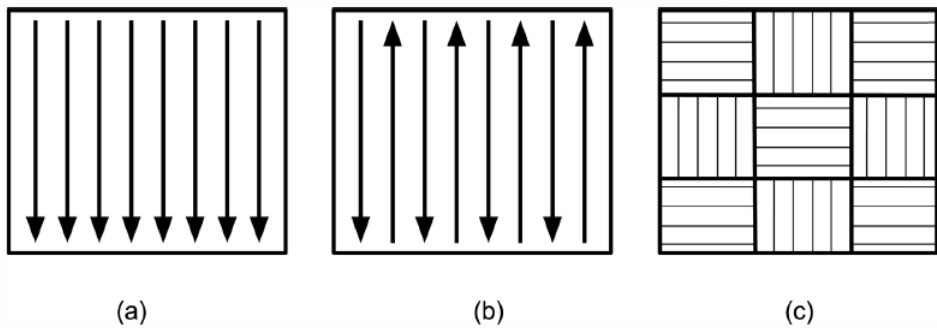


FIGURE 2.9: Schematic representation of scanning strategies commonly used in LSM (a) unidirectional long scan track; (b) bi-directional long scan track, and (c) islands (from Mertens et al., 2017 [44]).

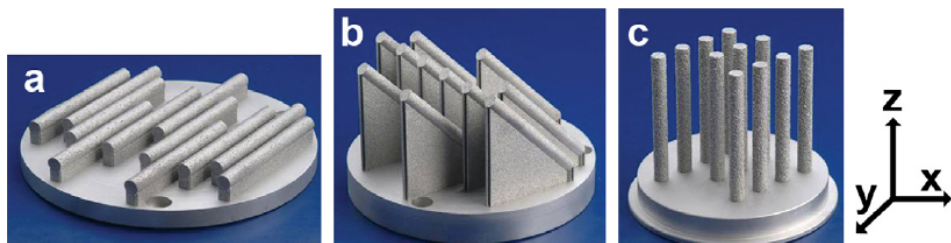


FIGURE 2.10: Samples (static tensile) built in different directions: (a) 0° , (b) 45° , and (c) 90° (from Brandl et al., 2012 [12]).

influence the process. Only the laser spot size at the 99% contour $\phi_{99\%}$ is frequently cited in literature. Its value lies between 20 and 200 $[\mu\text{m}]$ [12, 32, 45]. At this moment, no optimisation study was carried out about this variable. One should expect the optimal value for P , v_s , t , and h to depend on the spot size as it has a direct incidence on E_d .

Finally, the temperature of the powder bed and feeder affect the final properties of the manufactured parts as well. In particular, it was observed that pre-heating the powder at 300°C mitigates the differences of fatigue resistance between tensile specimens built in different directions: it is possible that the operation induces a slower cooling rate which helps reducing the distortions and internal stresses [12].

Once the porosity problem is sorted out, other matters can be addressed such as productivity and surface roughness. The latter is problematic as the surface finish obtained with SLM is typically of such poor quality that all cracks initiate near the surface for a sample with relative density $\rho_{rel} > 99\%$ [12]. As mentioned earlier, it is possible to reduce the surface roughness by mean of a dual scan strategy. However, the only options to obtain significantly better surface finish is currently to machine or polish the parts. This is one of the main weak points of SLM.

2.4 As-built mechanical properties

In a work of Kempen et al., it was concluded that as-built (AB) additively manufactured AlSi10Mg samples can have mechanical properties (Vickers hardness HV , ultimate tensile stress σ_u , fracture strain ϵ_f and impact energy) better or at least comparable to the conventionally casted and high pressure die casted (HPDC) alloy [31]. The tensile specimens built in an horizontal direction (XY) had slightly different characteristics than those built in the vertical direction (Z). The results obtained in the mentioned work are gathered in table 2.1, along with other results and common cast AlSi10Mg properties. The mechanical properties all lie in wide ranges. This illustrates the importance of mastering the process parameters. The best tensile properties measurements found on the web - both in terms of σ_u and ϵ_f - were obtained by EOS with $\rho_{rel} \simeq 99.85$ (ρ_b considered to be equal to $2.67 \left[\frac{g}{cm^3} \right]$) [17]. Unfortunately, the manufacturing conditions were omitted in sources [17], [31] and [35].

Process	E [GPa]	σ_y [MPa]	σ_u [MPa]	ϵ_f [%]	HV [HV]
SLM - XY direction [31]	68 ± 3	-	391 ± 6	5.55 ± 0.4	127
SLM - Z direction [31]		-	396 ± 8	3.47 ± 0.6	
SLM [7]	77 ± 5	268 ± 2	333 ± 15	1.4 ± 0.3	125 ± 1
SLM - XY direction [45]	65.5	227	358	3.9	-
SLM - Z direction [45]	75.4	172	289	2.6	-
SLM - XY direction [17]	75 ± 10	270 ± 10	460 ± 20	9 ± 2	119 ± 5
SLM - Z direction [17]	70 ± 10	240 ± 20	460 ± 20	6 ± 2	
SLM [35]	-	322.2 ± 8.1	434.3 ± 10.7	5.3 ± 0.2	-
Conventional cast and aged [31]	71	-	300-317	2.5-3.5	86
As built HPDC [31]		-	300-350	3-5	95-105
T6 treated HPDC [31]		-	330-365		130-133

TABLE 2.1: Mechanical properties of SLM built parts and cast + aged parts in literature

Furthermore, Wang et al. observed that preheating the manufacturing plate can have great impact on the mechanical properties [65]. This is due to the differences in thermal gradients between the substrate and the built samples, which induces residual stresses. Results obtained for a chessboard pattern are shown in table 2.2. Residual stresses are discussed further in section 2.5.

Plate temperature	σ_y [MPa]	σ_u [MPa]	ϵ_f [%]	ρ_{rel} [%]
80°C	176 ± 6	385 ± 6	3 ± 1.5	98.69 ± 0.19
120°C	257 ± 9	381.3 ± 3.3	2.83 ± 0.33	97.39 ± 0.38
160°C	233 ± 4	363.7 ± 11.3	5.33 ± 0.67	97.01

TABLE 2.2: Mechanical properties for different plate pre heating temperatures (from Wang et al., 2018) [65].

SLM AlSi10Mg is sometimes compared to wrought Al6061. It is also an aluminium-based alloy containing magnesium and silicon as major alloying elements. Its properties (after T6 treatment) are similar to its counterpart's as it is shown in table 2.3. It

could thus be considered as an alternative for given applications. Fatigue properties of SLM AlSi10Mg were observed to be substantially poorer than the other material's: its lifetime was approximately one order of magnitude less for any applied stress amplitude (see figure 2.11) [45]. It was proven that the latter material's defects control its fatigue life. The defects giving rise to failure often locate near the surfaces of the samples.

E [GPa]	σ_y [MPa]	σ_u [MPa]	ϵ_f [%]	HV [HV]
68.9	276	310	12	107

TABLE 2.3: Mechanical properties of T6 treated Al6061 alloy (from Aerospace Specification Metals Inc., 2000 [8])

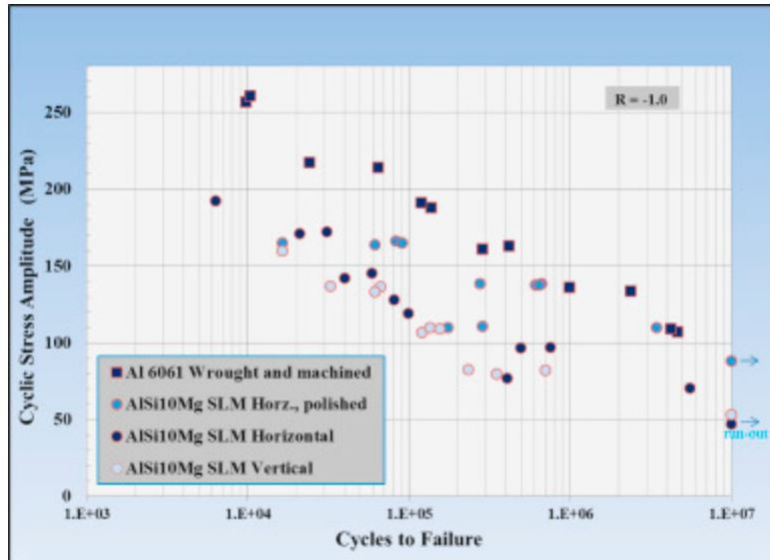


FIGURE 2.11: Measured room-temperature stress-life (S-N) of SLM AlSi10Mg, compared to that of conventional Al 6061. Bending fatigue (rotating beam) at a frequency of 25 Hz. (from Todd Mower and Michael Long, 2016 [45]).

2.5 Residual stresses in SLM parts

After most manufacturing processes, pieces can present residual stresses (both in compression and tension). While they are sometimes sought in some specific applications, they are more often unwanted consequences of the process. Uncontrolled internal stresses can in fact deteriorate dramatically the fatigue behaviour of the piece and cause unacceptable deformation as well as premature failure. They indeed facilitate the initiation of cracks growth [64].

There can be numerous causes to residual stresses, but it always comes down to inhomogeneous plastic strains. Several forming processes, such as cold rolling, can

induce them by applying a non-uniform load. On a more microscopic scale, different reactions to stress between distinct phases or crystal orientations are also able to create those inhomogeneities.

In the case of SLM parts, internal stresses are mostly due to the intense thermal gradients appearing during the scan. After the laser passing, the melt pool cools down and begins to solidify. This solidification causes thermal shrinkage of the molten track, which puts it under tensile condition. The continuous shrinking along the scan track concentrates those tension stresses horizontally, in the direction of the scan vectors. The stacking of layers, with their own tensile stresses, gradually relaxes the buried layers to the point that they begin to undergo compressive stresses below a certain depth. Vertical tensile stresses on the side surfaces, induced by those horizontal stresses at each layer, still remain after the complete manufacturing. An example of the stress distribution in a 2D section of a piece after manufacturing is available in Fig. 2.12. According to the supplier [28], Inconel718 has a yield strength of approximatively 1 GPa. Although residual stresses do not seem to reach it, their value is definitively high enough to completely modify the mechanical behaviour of the piece. In the case of a tensile test, for example, the zone near the surface would enter plasticity way before applying a stress equal to the yield strength.

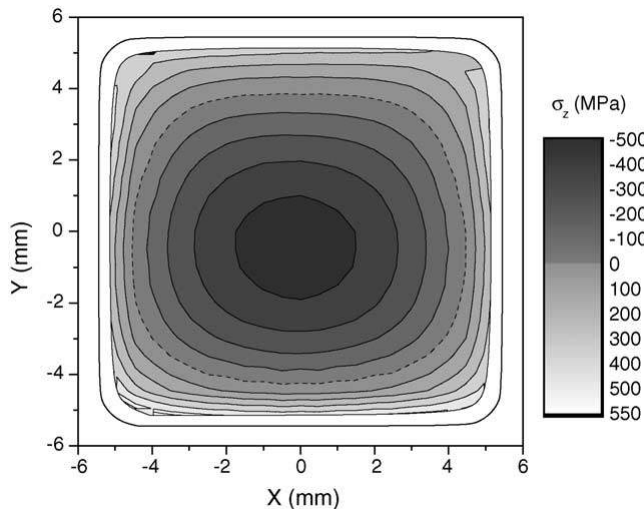


FIGURE 2.12: 2D plot of vertical internal stresses measured by the contour method at mid-height, in a vertically-built parallelepiped Inconel718 sample. Vertical stresses are null along the dashed line (from Vrancken, 2016 [64]).

Even though many process parameters influence the amount of residual stresses in the cooled part, reliable quantitative relations are difficult to obtain. On top of that, phenomena specific to the material used - such as the formation of precipitates or the allotropic transformations - restrain us from applying what is known about the process from one material to another. However, the parameter with the most obvious consequences on residual stresses is the powder bed preheating. While it indeed reduces the thermal gradient around the melt pool, and thus reduces internal stresses as well, it is suggested that the lower yield strength at higher temperature is the strongest stress-reducing factor [64].

Another parameter modifying the macroscopic thermal gradient of the part is the presence of building supports, depending on their ability to conduct heat to the platform. Indeed, a part built on a solid support, or directly onto the building platform, has a heat exchange area equal to its section. A honeycomb or another type of hollow support would reduce this area, because the unmelted powder has a much lower heat transfer coefficient[24]. Heat generated by the laser would thus escape more slowly out of the part, leading to a higher thermal gradient and, in turn, higher residual stresses [54], as it is shown in Fig. 2.13.

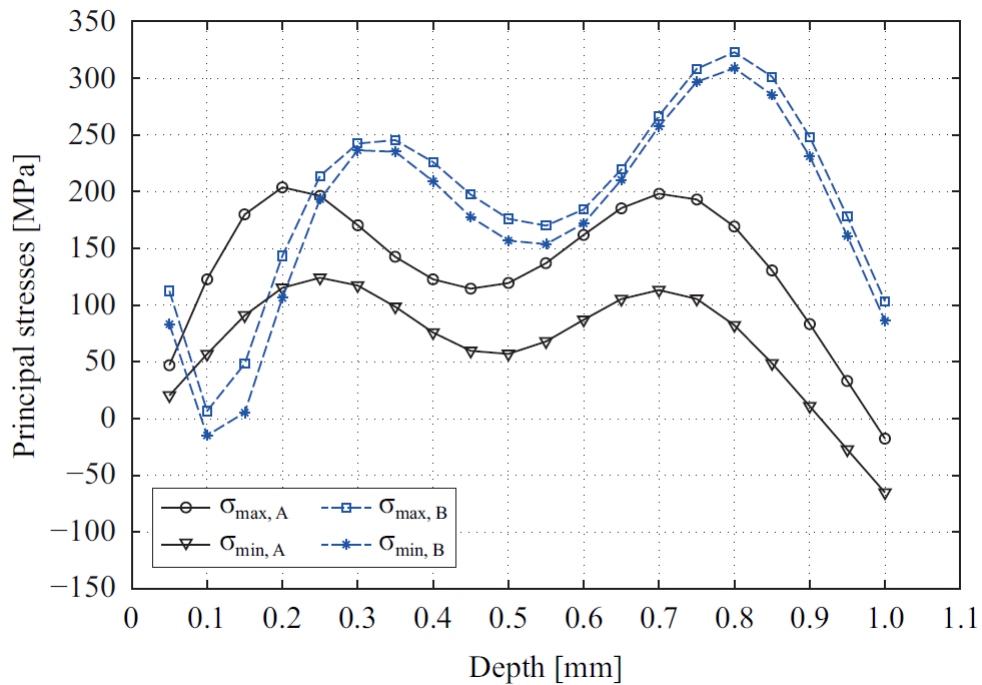


FIGURE 2.13: Principal residual stresses as a function of the depth relative to the surface in a AlSi10Mg part. Sample B is built onto an undefined hollow support, while A is not (from Salmi et al., 2017 [54]).

Scanning strategies also play an important role in the distribution of residual stresses. Both Kempen et al. (2011) [32] and Read et al. (2015) [50] have used an island laser scanning strategy patented by *Concept Laser*, which is supposed to reduce residual stresses in the part [13]. Li et al. (2014) [37] relieved stress by applying a dual scan strategy, where a second scan with lower laser energy follows immediately the main laser passage.

Many methods can be used to measure the residual stresses. They are usually categorised by their destructiveness on the tested part, and their depth of measurement in a reference material; steel. Some of these techniques are presented in Fig. 2.14. The most important non-destructive methods rely on diffraction, which use the lattice deformations at the atomic scale as indicators of the stress the material undergoes. Usual sources of radiation to diffract are X-rays, electrons and neutrons.

A common semi-destructive method is the center-hole drilling. A strain gauge rosette is arranged around a circular area with a diameter of a couple millimetres on

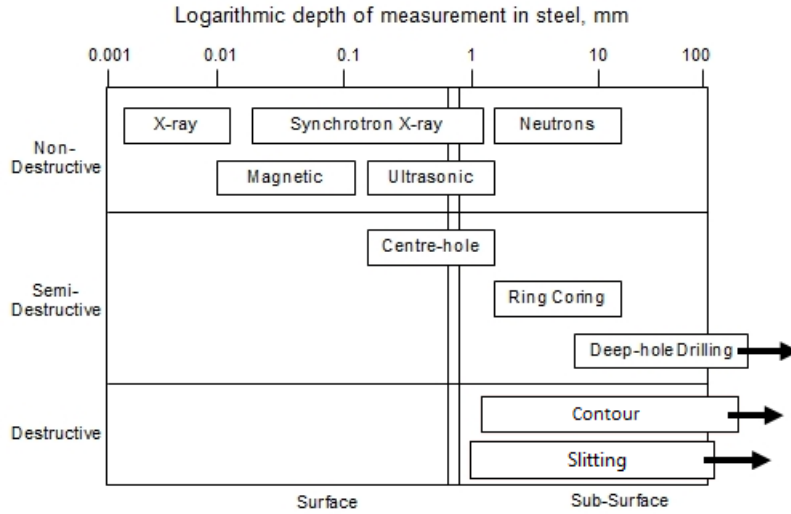


FIGURE 2.14: Non-exhaustive list of residual stresses measurement methods (from Hosseinzadeh [26]).

a part face. In this area, a shallow cylindrical hole is progressively drilled, increment by increment. The new surfaces formed enable the surrounding material to relax, deforming the hole. The strain gauges records this deformation for each increment. By using the ASTM E837-13a standard [10], those distortions allow to calculate the residual stresses present in the area before drilling. This method displays practical advantages such as its speed, versatility in term of materials and its ability to do on-site measurements [19].

A fairly recent destructive technique is the contour method (illustrated in figure 2.12). It was developed in the early 2000s by Los Alamos National Laboratory [40]. The first step, which makes this technique destructive, requires to cut the part in two. The final result of the method is the 2D distribution of residual stresses on the resulting cross-section. This new free surface allows the material to deform and relax some of its stresses. The contour (or shape) of this distorted surface is then measured by using, for example, a Coordinate Measuring Machine (CMM). Then comes the analytical part: a 3D finite-element model of the undeformed cut part is made. A strain with opposite norm to the one measured with the CMM is then applied to the model as a boundary condition, as if we forced the deformed surface back flat. Processing the finite-element results finally gives the stress distribution of the cross section. A visual representation of this calculation is shown in Fig.2.15

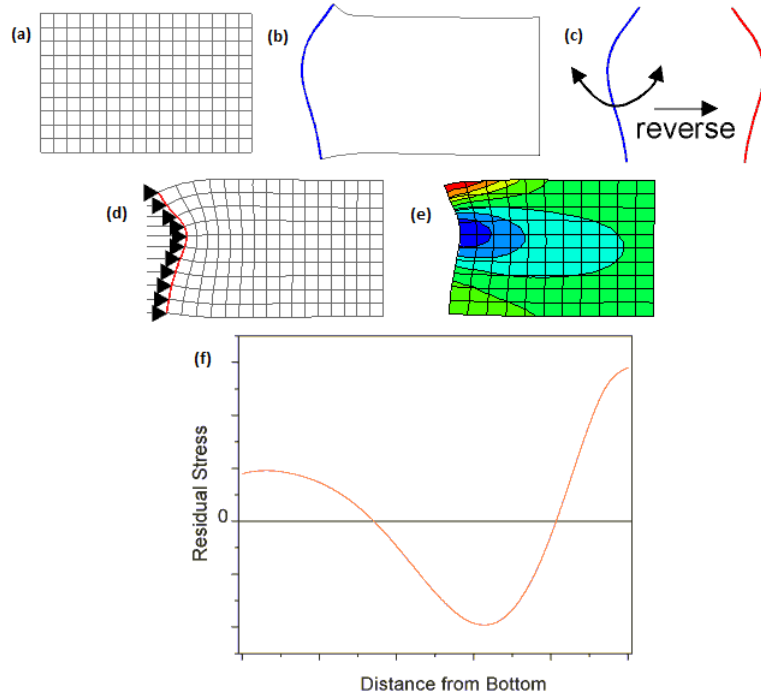


FIGURE 2.15: Thought process of the contour method analytical step: (a) finite-element model of the undeformed part, (b) measured contour of the real part, (c) inversion of strain, (d) application of the strain to the model, (e) resulting stresses in the model, (f) residual stresses normal to the cross section before cutting [40].

2.6 Post treatments

Unfortunately, although residual stresses can be attenuated as it was discussed above, their presence after the manufacturing seems unavoidable. However, cast alloys have known the same problems for their whole history. Various treatments have thus been developed over the years to try to reduce and modify these stresses after the initial manufacturing process. An important part of the literature on SLM alloys has simply studied the effects of those classical heat treatments on AM alloys [44].

If the aim is to remove residual stresses, the go-to treatment for aluminium alloys is an annealing at 300°C during 2 hours. Data on the heating and cooling speeds are scarce in the literature. Its qualitative effect on the mechanical properties of AM parts is pretty well known and consistent in the literature, at least compared to other treatments. A summary of its effects is presented in Fig. 2.16 [49], for different temperatures. The annealing temperature can be varied to obtain a wide spectrum of properties, in order to be better suited for new applications. This treatment reduces strength, both ultimate and yield, while increasing ductility, and this effect is reinforced with rising temperature (at least below 500°C). Mertens et al. (2015)[43] obtained a very good trade-off, when applying an annealing at 250°C for 2 hours with a loss of only 10% of yield strength and barely 2% of UTS, the elongation at break increased by 80%.

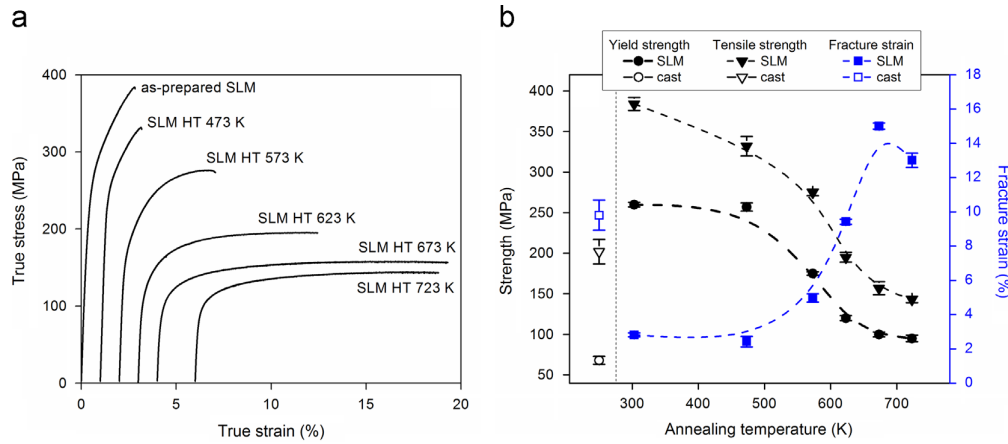


FIGURE 2.16: (a) True strain-stress curves for an AB AlSi12 sample and several heat-treated ones at different temperatures and (b) corresponding mechanical properties (from Prashanth et al., 2014 [49]).

A very common heat treatment of aluminium alloys is designated by the T6 acronym. It consists of a solution heat treatment around 520°C for a variable duration, followed by a water quenching to room temperature and an artificial ageing for several hours between 150 and 190°C. When applied to conventionally processed aluminium-based materials, this treatment usually has a hardening effect. The principle is the following [58]: first step increases solubility of alloying elements in the Al-phase. Water quenching prevents these elements from exiting the phase during cooling, creating a roughly homogeneous super-saturated solution. The artificial ageing finally allows them to slowly diffuse out of the aluminium lattice, forming homogeneously distributed very fine precipitates, hardening the alloy. However, Aboulkhair et al. (2015) [4], as well as others, have shown that AM alloys react very differently to this treatment: softening was observed rather than hardening. They suggested that it is due to the dissimilar starting microstructures. T6 heat treatment forms precipitates, but coarsens the AM alloy microstructure at the same time. The strengthening due to the microstructure refinement outweighs in fact the one due to precipitation. This softening means however a higher ductility, and thus a better fatigue strength. A summary of the consequences of T6 heat treatment can be found in Table 2.4.

The time and temperature parameters during the solutionizing and the ageing seem to remain determinant in the prediction of the final properties of the treated part. Indeed, according to Mertens et al. (2015)[43], a T6-like treatment can result in an increase of ductility - of course - but also of yield strength. To be complete, they obtained a decrease of hardness of 28%, a decrease of ultimate tensile strength by 13%, but an increase of elongation at break of 220% and of yield strength of 30%. The distinct process parameters could explain the differences: 510° C during 6 hours followed by 4 hours at 170° C for Mertens et al. (2015)[43], compared to 1 hour at 520° C and then 6 hours at 160° C. Differences in manufacturing parameters, such as layer thickness and substrate heating, can as well be at cause.

Hot isostatic pressing (HIP) post-treatment is commercially used for cast aluminium and some have tried to transpose it to SLM AlSi10Mg. Sample is put in a furnace at high pressure ($\simeq 100$ [MPa]) and high temperature (above 500°C). These

Property	Effect of heat treatment (%)
Nano-hardness	-(16 ± 1) ↓
Micro-hardness	-(20 ± 1) ↓
Ultimate tensile strength	-(12 ± 5) ↓
Yield tensile strength	-(11 ± 1) ↓
Tensile elongation at failure	+(179 ± 57) ↑
Compressive strength at 25% strain	-(56 ± 0.003) ↓
Yield compressive strength	-(47 ± 2) ↓

TABLE 2.4: Changes in percentage of the main mechanical properties of SLM AlSi10Mg after T6 treatment, compared to their as-built state (from Aboulkhair et al., 2016 [7]).

conditions lead to the emergence of plastic flow which heal the internal porosity. This can enhance the mechanical properties of the alloy and reduce the properties scatter [29]. Mower et al. (2016) [45] applied HIP at 900°C and 102 [MPa] to a Ti6Al4V AM alloy and obtained a large increase of fracture strain and enhanced fatigue strength. Tradowsky et al. (2016) [59] reported the same fracture strain increase for the AlSi10Mg alloy.

Annealing, as well as other heat treatments, alter the mechanical properties through 2 different processes. First, it relieves residual stresses. Indeed, yield strength of materials is inversely correlated to temperature. During heating, residual stresses at some points in the material surpass the declining yield strength. Those points thus deform plastically, lowering the stress they undergo. In the end, the maximum stress remaining in the material is equal to the yield strength at the highest temperature reached. The resulting residual stresses require specific techniques to be assessed as we saw in section 2.5.

Secondly, heat-treating at a sufficient temperature can also modify the microstructure of the alloy. This can be directly observed by optical or electronic microscopy. As described in Fig. 2.17, increasing the temperature allows the diffusion of Si. It is caused by the fast solidification of the alloy, which leaves it in a metastable state. Decrease of Si solubility in the Al-phase during cooling and rate of the process traps Si inside the Al solid phase, which becomes super-saturated [49].

Temperature rise allows the ejection of Si out the Al-phase to form small particles. These particles as well as the Si present at the cells boundaries further diffuse with increase of temperature or holding time. They tend to agglomerate, reducing the total number of particles but increasing their size. This process is called spheroidization.

Non-thermal processes affecting the residual stresses also exist. As we saw in the previous section, tensile stresses near the surface are the most problematic. A purely mechanical treatment able to cancel these is shot-peening. High velocity projectiles, usually metallic or ceramic beads, are used to hit a surface. The impacts deform

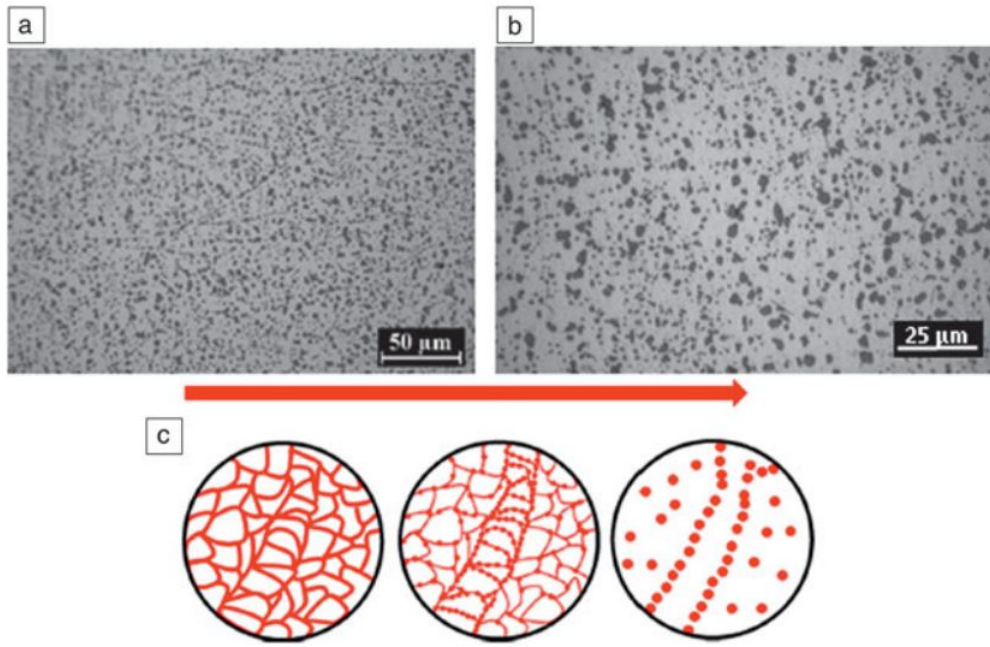


FIGURE 2.17: (a) The microstructure of selective laser melted AlSi10Mg after annealing heat treatment and (b) solution heat treatment followed by artificial aging. (c) Schematic representation of the spheroidization process. Si particles gradually grow and concentrate along the cell boundaries, which become less visible (from Aboulkhair et al., 2017 [6]).

plastically the top of the part, which tries to stretch in the horizontal direction. This is prevented by the material below, which remains undeformed. The surface layer thus finds itself in a compressive state [64]. If tensile stresses were present near the surface, they get cancelled by the important compressive stresses included in the material. While injecting compression near the surface can already be beneficial, by hindering crack initiation for example, Salmi et al. (2017) [54] also obtained a certain degree of homogenization of the stresses all along the examined depth.

Lastly, another well-known drawback of AM parts is their mediocre surface finish compared to cast parts. This roughness, as well as the presence of open porosities, is an important cause of the relatively poor fatigue strength because they constitute privileged points of fracture initiation. However, polishing and machining have shown themselves not very efficient at enhancing fatigue behaviour of AM samples. Mower et al. (2016)[45] had mixed results, where Ti6Al4V parts were improved by machining, while AlSi10Mg ones kept poor fatigue properties after mechanical electrochemical polishing. Aboulkhair et al. (2016) [2] obtained mitigated results as well, with only some improvement at lower stress levels, whereas heat treatments had a much more significant influence. Both concluded that this lack of enhancement was probably due to the numerous defects near the surface, as well as in the bulk, that were impossible to remove through polishing.

Although machining the surface does indeed reduce its roughness, it can also expose buried porosities at the same time which creates sites of choice for fatigue cracking. On top of it, polishing and machining may not always prove themselves

easy, fast or cheap to apply to complex-shaped AM parts. They most probably also impact the residual stresses. Machining was observed to have a tremendous influence for forged aluminium [16]. Cutting speed, feed per tooth and cooling were observed to have notable effects but not as critical as the corner radius's (see figure 2.18). High compression stresses were induced, going up to nearly 300 [MPa].

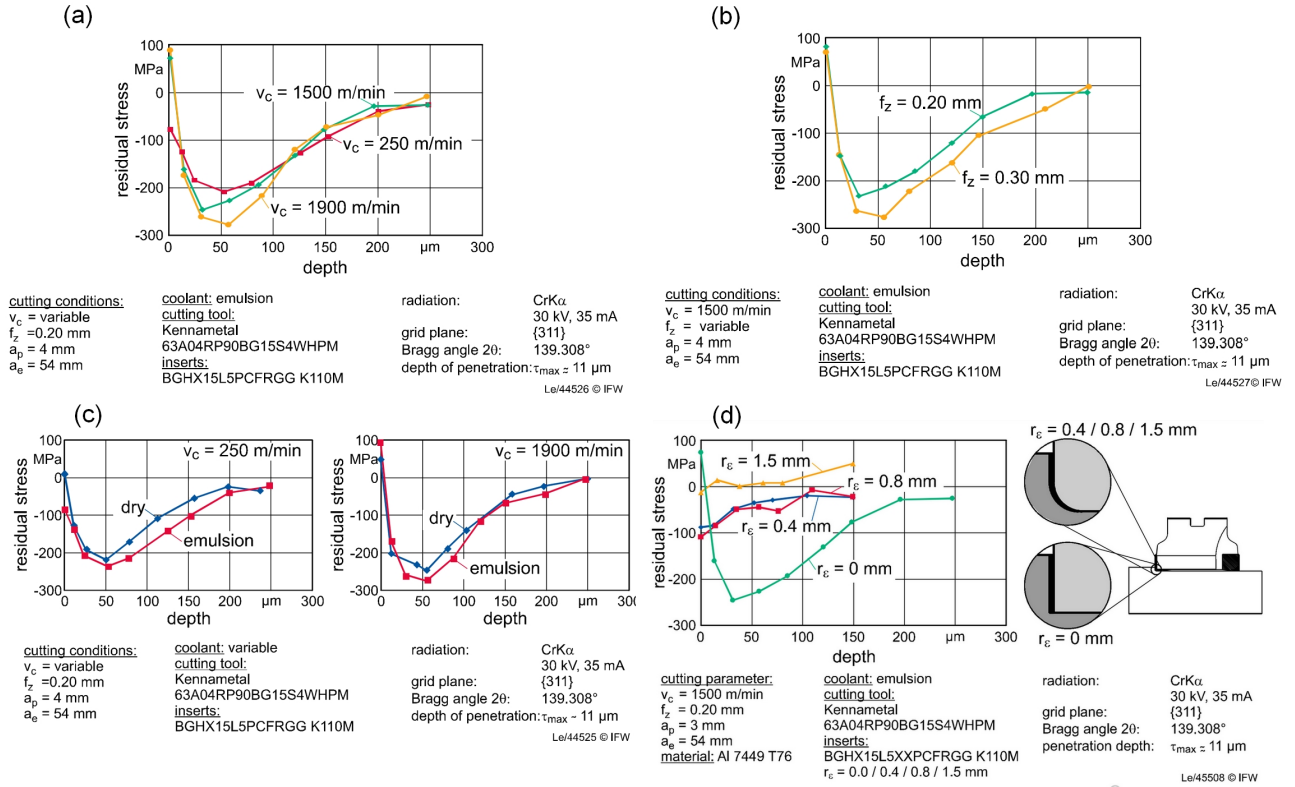


FIGURE 2.18: Influence of the cutting parameters on the residual stresses of machined forged aluminium: (a) cutting speed (b) feed per tooth (c) cooling (d) corner radius (from Denkena et al., 2007 [16]).

Chapter 3

Materials and methods

3.1 Powder follow-up

To avoid wasting material, the non-sintered powder remaining on the plate after the manufacturing and the excess powder swept by the roller for each layer was collected in standard recipients. It was then resieved and reused. The evolution of the powder composition and grain size was monitored during the year to assess its influence on the process and properties.

3.1.1 Sieving

The powder collected from the printer after the process went systematically through a sieving step, with the aim of limiting the size of the particles used for the next batch. A *Phenix Systems PX Box* was used. It consists of a circular vibrating sieving machine with mesh size of 75 [μm] integrated in a handling glove box.

3.1.2 Grain size and distribution

For several manufacturing batches along the year, samples of the powder placed inside the store were taken. Those samples were used to conduct analyses of composition, which will be discussed just after, and grain size.

A *Beckman Coulter LS100Q Laser Diffraction Particle Size Analyzer* [11] with fluid module was used to determine the grain size distributions. The applied procedure is the following: a small amount of powder is immersed in a bath of isopropanol and forms a suspension. It is then exposed to a laser and diffracts it, according to Fraunhofer equation. This method assumes that particles are spherical.

Four consecutive measures were made for each sample. Four additional measures were taken after the powder was exposed to ultrasonic vibrations, intended to break the eventual agglomerates.

3.1.3 Composition

The composition of several samples of fresh and recycled powder was estimated through inductively coupled plasma (ICP) spectrometry, thanks to an *Agilent 5100 ICP-OES*. Chips obtained from the machining of manufactured specimens were also tested with the same method.

ICP is a technique permitting the detection of chemical elements and the measurement of their mass fraction in a material sample. It uses inductively coupled

argon gas plasma to ionise the atoms in presence. The ions are then separated depending on their mass-to-charge ratio. A detector finally computes the different concentrations based on the ions signals [69]. A schematic description of the set up is shown in figure 3.1. ICP cannot detect the following elements: hydrogen, carbon, nitrogen, oxygen, fluorine, chlorine, and noble gases [46].

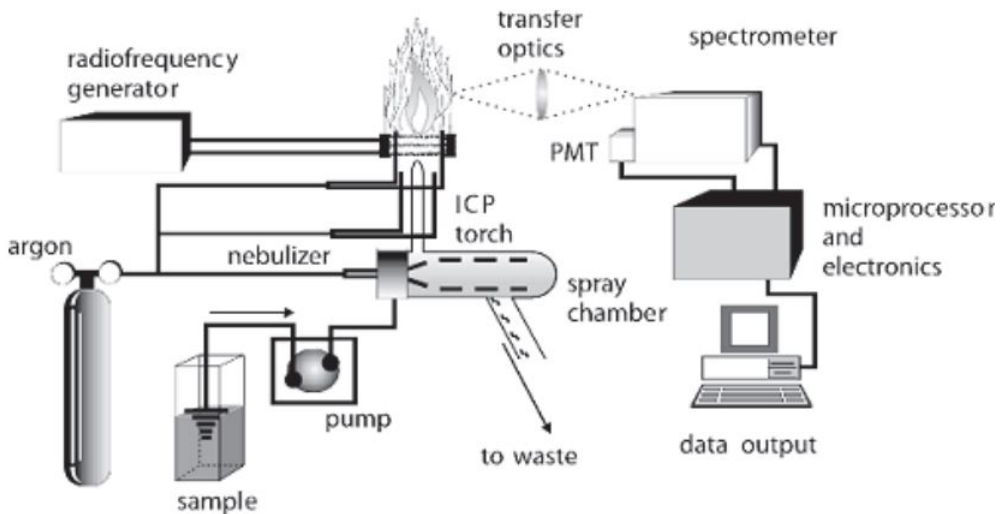


FIGURE 3.1: Schematic of the inductively coupled plasma spectroscopy technique set up (from *Spectro Scientific*, 2017).

3.2 SLM manufacturing

The same direct metal printer (DMP) was used to manufacture all specimens throughout this work. It is a *3D Systems ProX DMP 200* printer (see figure 3.2). It uses a laser with a theoretical maximal power of 300 [W] and wavelength $\lambda = 1070$ [nm] [1]. Its actual maximal power is $P_{max} = 273.6$ [W]. The maximal envelope capacity of the machine ($W \times D \times H$) is $140 \times 140 \times 125$ [mm]. Its typical accuracy is $+/- 50$ [μm] for small parts and $+/- 0.2\%$ for large parts. It allows for the set-up of a protection atmosphere. However, it does not integrate any heating feature for the build bed.

In this thesis, argon was used as shielding gas. The composition of the gas environment was monitored so as to keep $p_{O_2} < 500$ [ppm]. Laser compensations were set to take into account the excess energy at the start and end of the scanning vectors (see figure 3.3). These were chosen in accordance with the manufacturer recommendations (figure 3.4). The 99% contour spot size $\phi_{99\%}$ was set to 75 [μm]. Values for hatch space (h) and layer thickness (t) were respectively set to 100 [μm] and 30 [μm]. The scan speed (v_s) and the laser power (P) were varied in the ranges $[900 ; 1500]$ [$\frac{mm}{s}$] and $[0.75 \cdot P_{max} ; P_{max}]$ respectively, in order to optimise of the built specimens (see section 4.2.1). Educated guesses were made based on literature and previous works done at the UCL. The parameters used are resumed in appendix A.1. Batches were named in the format X200-yyymmdd. The prefix "X200" refers to the DMP used. It is followed by the date of printing (6 digits). Recycled powder was used for every



FIGURE 3.2: ProX DMP 200 printer (from the user's ProX DMP 200 general instructions document).

batch except for X200-180222 and X200-180228. Figures with detailed specimens positions, denominations, scanning orders and sintering durations for all batches are available in appendix A.2.

The batches were first prepared on *DMP ProX Manufacturing*, a dedicated CAD software. It allowed the selection of the values for the parameters previously mentioned, as well as the position of the specimens. Each specimen was built on building supports. After the completion of the process, they were separated from the plate through electro-erosion.

For this thesis, all cylinders and tensile specimens were built vertically. The dimensions notations for the samples types and the tensile specimens detailed geometry are gathered on figure 3.5.

An island scanning strategy was chosen on account of research done on the subject (see section 2.3). It is a hexagonal pattern. The replicated hexagon's smallest width is equal to 5 [mm]. An overlap of 100 [μm] was set, as illustrated on figure 3.6. There is a rotation of 90° and a translation of a third of basis vector between two successive powder layers as depicted by figure 3.7. In the case of a contour scanning strategy, the contours were pre scanned for each powder layer with the same P and v_s used for the bulk (see figure 3.8). The scanning order among the samples was automatically chosen and periodic.

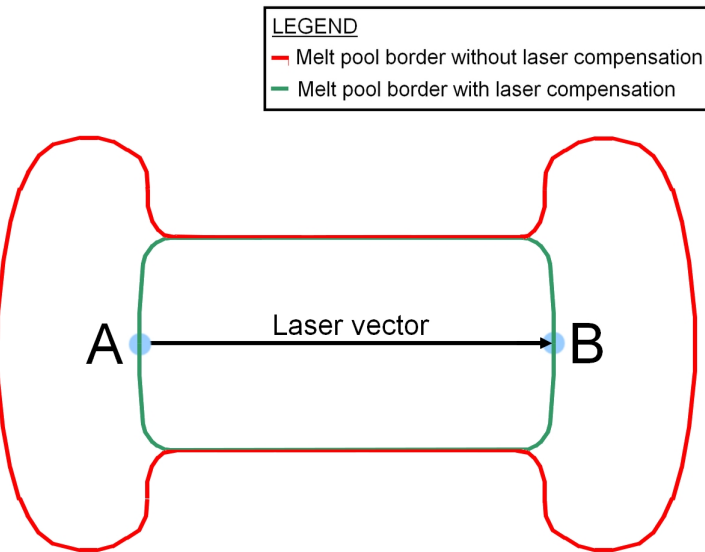


FIGURE 3.3: Melt pool contours with and without laser compensation (exaggeration).

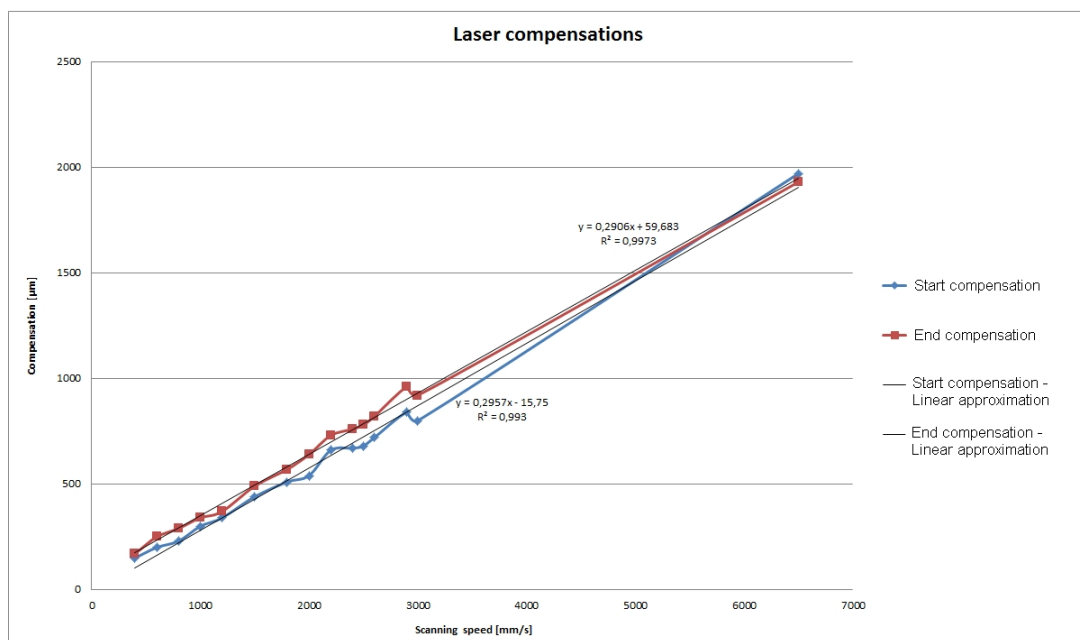


FIGURE 3.4: Laser compensations as a function of the scanning speed (as recommended by the manufacturer).

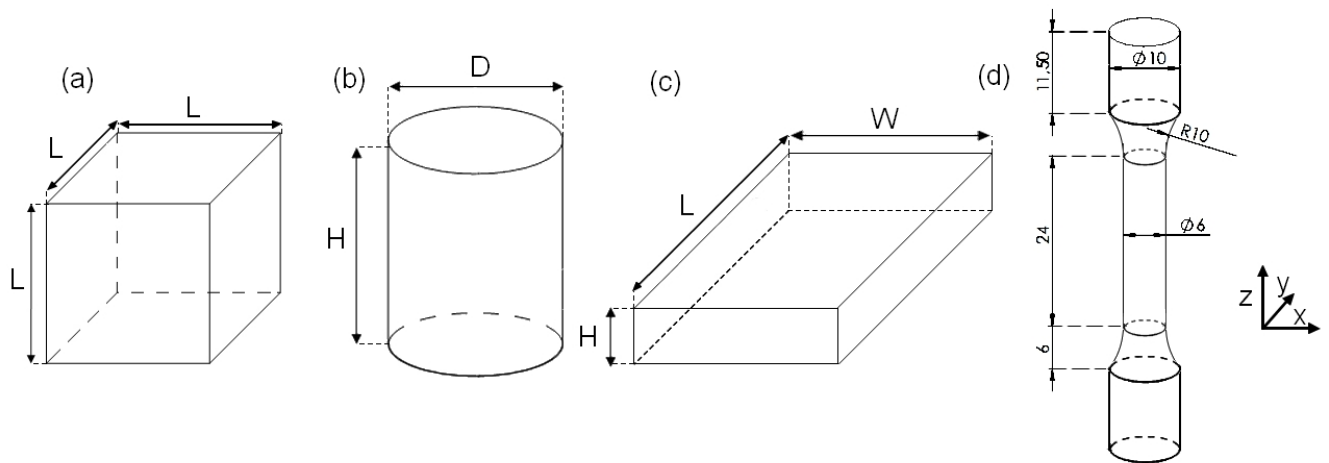


FIGURE 3.5: Dimensions notations for (a) cubic specimens (b) cylindrical specimens (c) parallelepiped specimens (d) tensile specimens with dimensions in [mm]

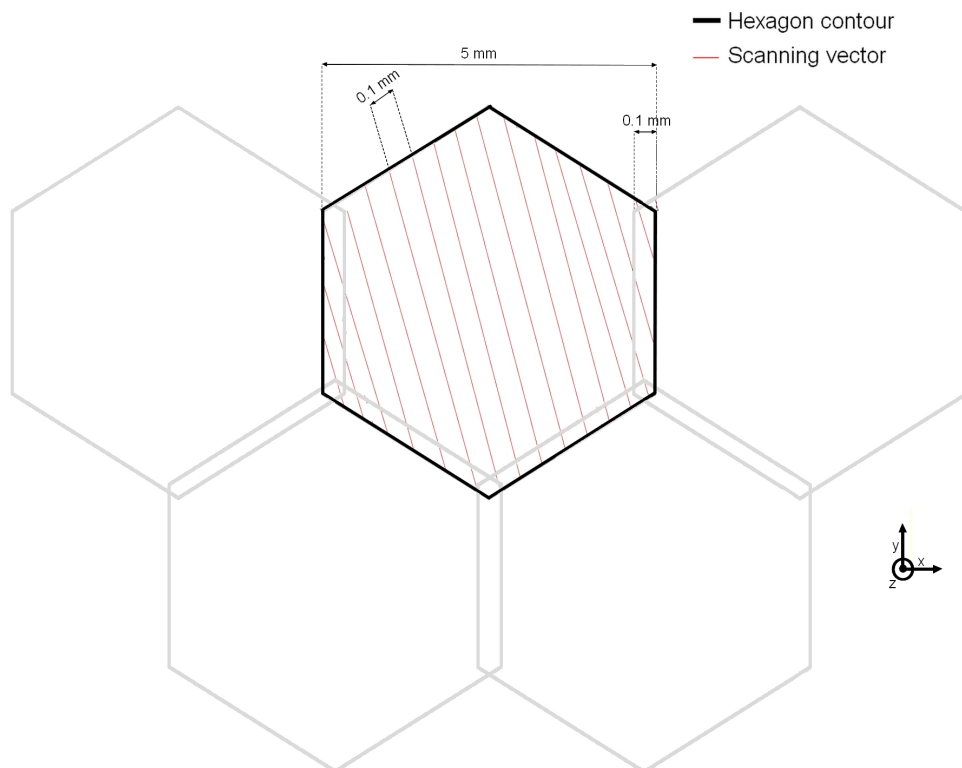


FIGURE 3.6: Schematic representation of the hexagonal pattern scanning strategy

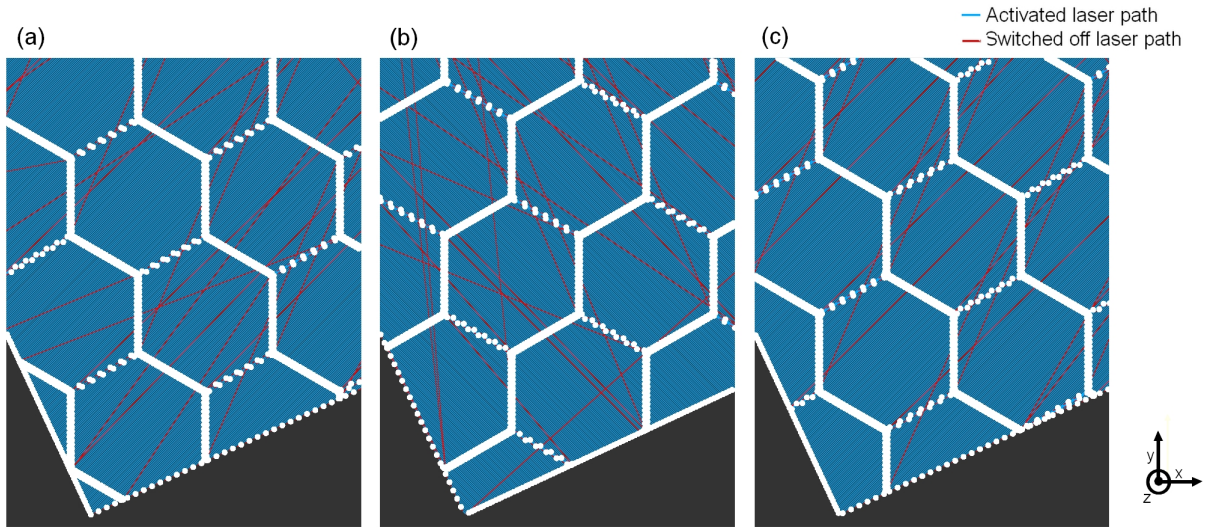


FIGURE 3.7: Laser scanning pattern for a parallelepiped sample: (a) Layer n (b) Layer $n + 1$ (c) Layer $n + 2$

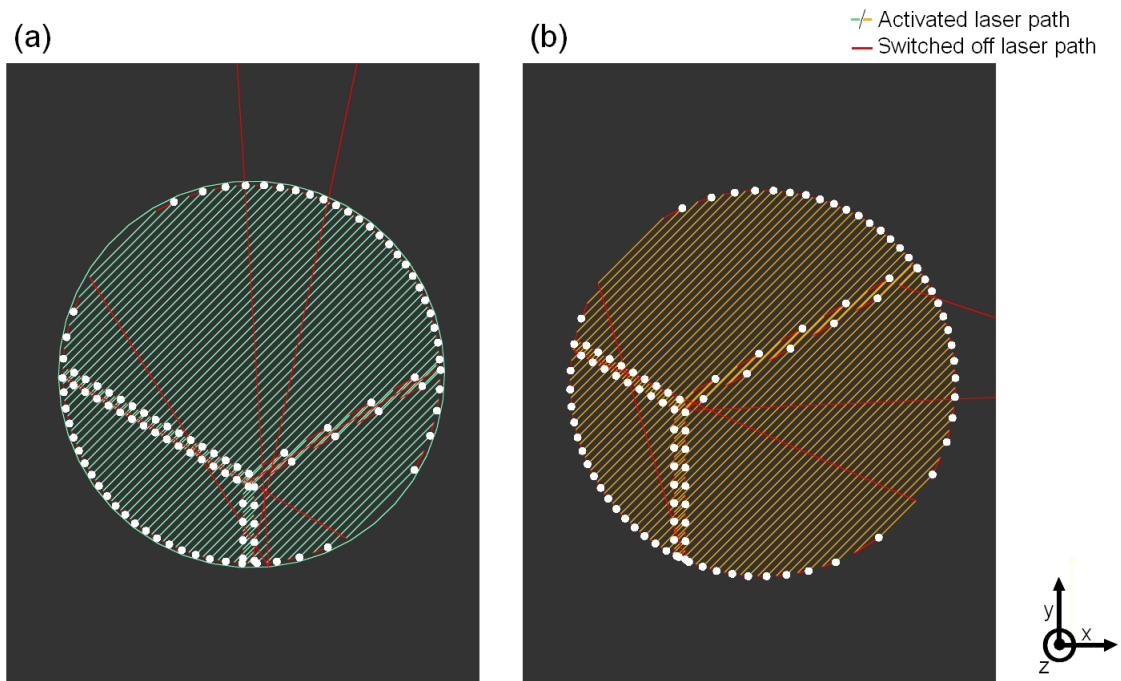


FIGURE 3.8: Screen capture of the laser path for a cylindric sample (a) with contour scanning strategy (b) without contour scanning strategy

3.3 Heat treatments

The heat treatments were conducted inside a unique oven of the VT 5050 EKP model manufactured by Heraeus, which is able to reach a temperature of 400° C. The samples were introduced in the cold oven under an air atmosphere, and after the annealing, were left to cool down in the turned off oven with the door open. Samples temperature data was obtained through a T-type thermocouple soldered to the sample surface, thanks to a *Labfacility L60 Thermocouple & Fine Wire Welder*. The data was displayed and saved every 10 seconds with a precision of 0.1° C, thanks to a *Agilent 34972A LXI Data Acquisition/Switching Unit* connected to the thermocouple (see Fig.3.9 for both devices). For reasons that can not be explained only by thermal inertia, setting the oven to the target temperature was not efficient to heat the specimens to the same temperature. After a couple of tests, the oven was then set at a temperature about 20° C above the target so that the temperature measured by the thermocouple welded on the sample reached the target temperature.

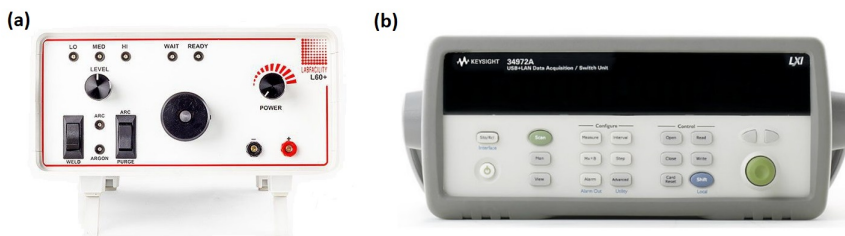


FIGURE 3.9: Pictures of (a) *Labfacility L60 Thermocouple & Fine Wire Welder* and (b) *Agilent 34972A LXI Data Acquisition/Switching Unit*.

Due to the inaccuracy of the oven, maintaining the samples at the exact target temperature was not possible. The holding plateaus were thus rather slow increasing slopes. For most of the samples, the theoretical beginning of the holding was set when the specimen reached a temperature 5° C below the target value. In this way, the sample average temperature for the complete holding was the closest possible to target value. A representative heating curve is available in Fig. 3.10. By posterior calculations, it appeared that all the samples have been heated at an approximative rate of 6°C/min. The non-linearity of cooling prevents us to give overall rate, but during the 20 minutes, the specimens cool down by about 7°C/min.

Samples that were subject to a heat treatment were named in a particular format, to ease distinction between them. They received the name of the batch, followed by "TT-holdingtemperature-holdingtime-specificities". Cubes that were subject to heat treatments were 5 x 5 x 5 [mm³].

The main objective of most of the research about aluminium alloys AM is to obtain parts with properties at least as good as their conventional cast counterparts. To obtain a larger panel of properties, a vast number of heat treatments have been developed for die cast alloys. The classical treatment of stress-relief for aluminium consists of a heating up to 300° C, with a holding duration of 2 hours followed by a slow cooling [44]. This treatment and its variants have been tried on a number of

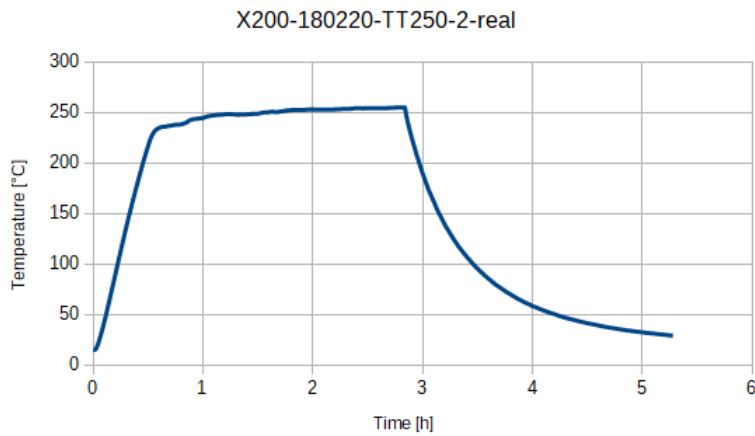


FIGURE 3.10: Temperature curve measured by the T-type thermo-couple for the cubic sample annealed at 250°C for 2 hours.

additively manufactured samples, in order to assess their effect on the microstructure and mechanical properties of the parts.

A first series of cubic samples was manufactured using the optimised process parameters from Section 4.2.1, namely ($P = 75\%P_{max}$; $v_s = 1200[\frac{mm}{sec}]$; $E_d = 57[\frac{J}{mm^3}]$) and a different heat treatment was applied to each one of them. The complete list of cubes treated can be found in Table 3.1.

Specimen	Holding time [min]	Aimed holding temp. [°C]	Max. temp. [°C]
X200-180220-TT150-2	120	150	-
X200-180220-TT200-2	120	200	-
X200-180220-TT300-2	120	300	256
X200-180220-TT300-2-plaque	120	300	281
X200-180220-TT150-2-real	120	150	156
X200-180220-TT200-2-real	120	200	203
X200-180220-TT250-2-real	120	250	255
X200-180220-TT300-2-real	120	300	302
X200-180220-TT300-1-real	60	300	302
X200-180220-TT360-1-real	60	360	371
X200-180220-TT300-5m-real	5	300	300
X200-180319-TT225-2-real	120	225	242

TABLE 3.1: List of the cubic heat-treated specimens

3.4 Characterisation

3.4.1 Density

Hydrostatic weighing

Multiple methods were considered to estimate the relative density of the specimens. The first one is hydrostatic weighting (HW), or hydrodensitometry. It is a direct application of the well-known Archimedes' principle, which can be stated as follows: "When a body is (partially or totally) immersed in a fluid, the upthrust on the body is equal to the weight of fluid displaced." [14]. By weighing each pieces in air and in water - giving respectively values of dry weight W_a and underwater weight W_w - one can calculate the apparent density ρ_a [30]:

$$\rho_a = \frac{W_a}{W_a - W_w} \cdot \rho_w$$

where ρ_w is the water density. The apparent relative density $\rho_{a,rel}$ of the specimens can then be calculated with:

$$\rho_{a,rel} = \frac{\rho_a}{\rho_b}$$

where $\rho_b = 2.68[\frac{g}{mm^3}]$ is the theoretical bulk density of AlSi10Mg [51]. All weightings were done with a *Sartorius BP121S* analytical balance with precision of 0.1 [mg] [55]. Samples were immersed in demineralised water for more than twelve hours before the measurements to impregnate them. The weightings were also done in demineralised water. Water temperature was measured with a precision glass thermometer to compute ρ_w as accurately as possible thanks to tabulated values [67]. Multiple measurements were done for each sample in order to increase the method's reliability.

The technique was employed with "as-built" and polished cubes. For this second option, all six faces of the tested cubes were polished with P320 silicon carbide sandpaper sheets and briefly with P1200 ones. In most cases, the tests were done with samples of volumes $\simeq 1[cm^3]$ and weights $\simeq 2.5[g]$.

Relative optical density image analysis

Another method was used to estimate the relative density of the various samples: the relative optical density image analysis (RODIA). For this purpose, the samples were cut with a micro-cutting machine and underwent the polishing routine detailed in table 3.2. Pictures of the polished sections were then taken under the optical microscope. An *Olympus AX70* microscope was used, with 5x and 10x magnification. The pictures were taken with a smart-phone through the lens of the microscope. The used camera has a resolution of 16 [MP]. A camera is directly connected to the microscope at the laboratory, but it only has a 5 [MP] resolution. As a result, the latter was not used.

With the help of the *ImageJ* software, the surface of both the porosities and the whole surface could be isolated for each analysed image (see figure 3.11). The surface fraction occupied by porosities could then be obtained as the ratio between the areas of the two (in pixels). If we approximate that the porosities surface fraction is

equal to the volumetric one, that method gives an estimation of the relative density ρ_{rel} .

Step	Polishing surface	Abrasive	Grain size	Lubricant type	Rotation speed [rpm]
1	MD-piano 220	Diamond	P220	Water	200-300
2	MD-piano 1200	Diamond	P1200	Water	200-300
3	MD-largo	DP-spray	9 μm	Alcohol	150
4	DP-DAC	DP-spray	3 μm	Alcohol	150
5	DP-NAP	DP-spray	1 μm	Alcohol	150

TABLE 3.2: Polishing routine for Al-Si alloys

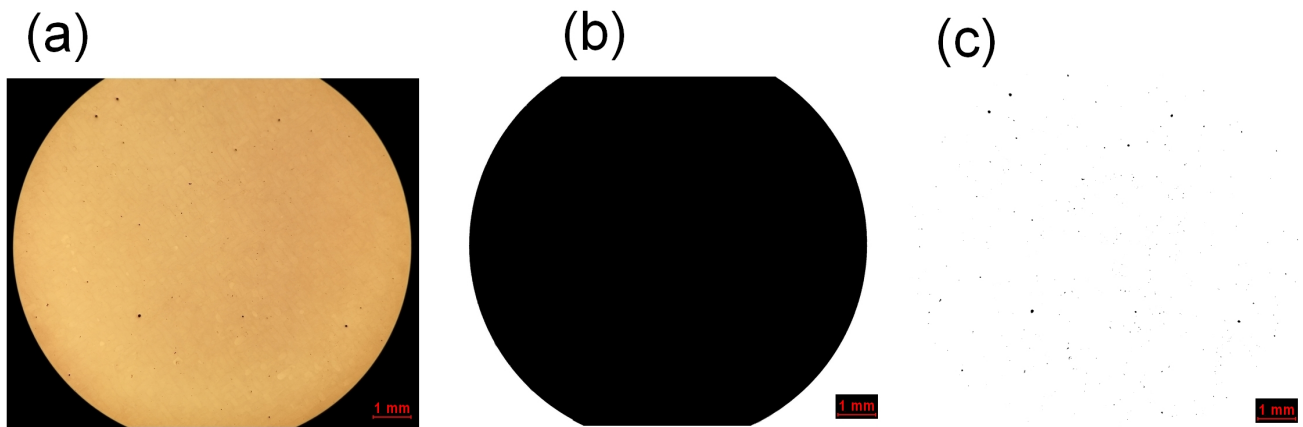


FIGURE 3.11: RODIA procedure for specimen X200-180319-cub 1: (a) Original picture of polished section (b) Whole surface isolation with *ImageJ* (c) Porosities isolation with *ImageJ*.

The images isolations in "foregrounds" and "backgrounds" were done through manual thresholding based on pixel intensity quantifications. An optimal threshold was sought for porosities isolation so as to include only holes, and as many as possible. Particular attention was given to the photography in order to obtain the best contrast, focus and intensity homogeneity. Between two and five photographs were taken for each specimen to build a representative sample.

3.4.2 Microstructure

Optical microscopy

In order to make the identification of the melt pools boundaries possible, the samples underwent the polishing routine detailed in table 3.2. They were then etched with a Keller's reagent. It is a popular etchant containing hydrochloric acid, hydrofluoric acid and nitric acid diluted in distilled water.

A study of the melt pool sizes was conducted (see section 4.2.2). As SLM involves melt pools overlapping to ensure consolidation, one cannot measure the actual original melt pools dimensions. The method has thus only been used as a tool to compare samples.

Scanning electron microscopy

Microstructure and fracture surfaces were observed thanks to a Zeiss Ultra-55 Scanning Electron Microscope with a field emission gun, both through secondary electrons imaging. Microstructure observation required the same polishing routine as for optical microscopy, with the exception of the last step (etching) which was replaced by a smooth mechano-chemical polishing with an Oxide Polishing Suspension (*Struers Op-S NonDry*).

Size of cells and ductile dimples were measured with the linear intercept method, as well as the interdistances between the globular Si particles in heat-treated samples. An example of this method is available in figure 3.12. The size of these particles was measured via image analysis, with the help of the *ImageJ* software.

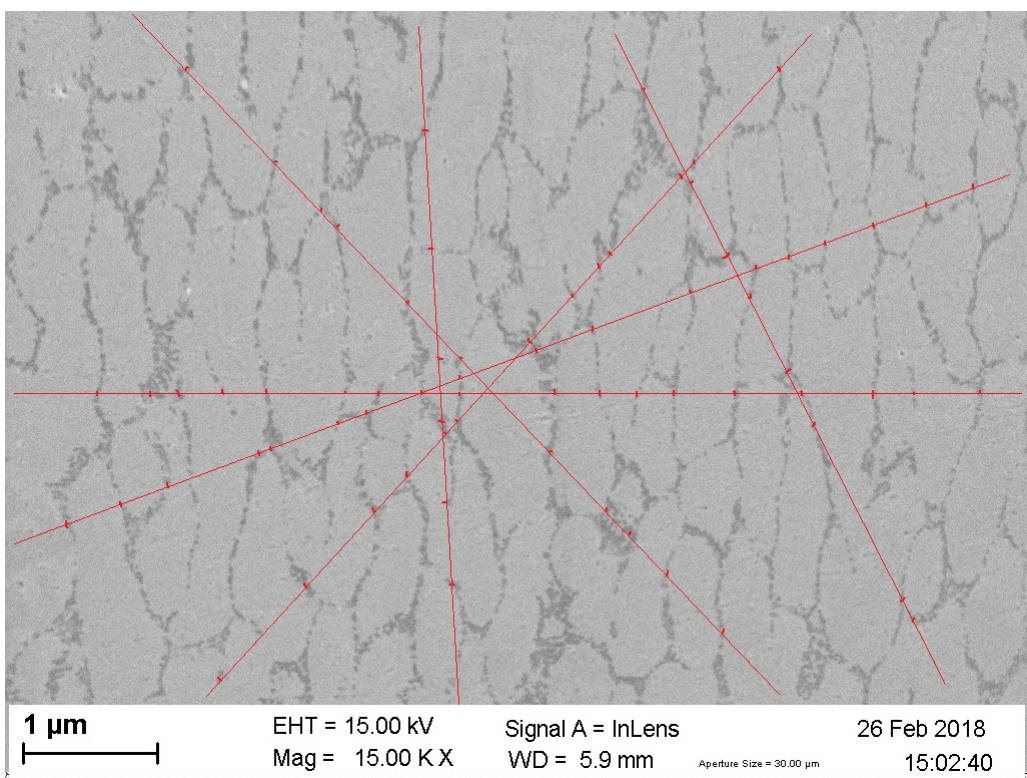


FIGURE 3.12: Implementation of the mean linear intercept method on a SEM picture of an as-built sample.

3.4.3 Residual stresses

Measurements of residual stresses were performed by Dr Ing. Pierluigi Mollicone, at University of Malta. Two parallelepiped specimens were specifically built to undergo the semi-destructive method of hole drilling. Their dimensions are $10 \times 40 \times 120$ [mm³]. One was tested as-built, while the other was heat-treated at 300°C for 2h. Machining of the latter was performed after the heat treatment, removing the least matter possible, before shipping to Malta. This was done in order to reduce rugosity on the top and bottom faces of the samples, because smooth surfaces are necessary

for the correct fixation of the gauges.

From the deformation measured by the strain gauges during the hole drilling, residual stresses were calculated with the integral method, as well as with its simplified approximation [60], the power series method.

For the sake of comparison, 5 samples were also subjected to a *Bruker D8 Advance X-Rays Diffractometer*, in order to obtain qualitative information about the deformation of the crystal lattice, and thus residual stresses. The wavelength of the X-ray was 1.5406 [nm], and the angle was varied between 20 and 100°.

3.4.4 Mechanical properties

Hardness test

Vickers hardness measurements were made with a *Wolpert Dia-Testor 2RC* tester. Nearly all tested specimens were cut beforehand with a micro-cutting machine and indented on one of the two exposed cross sections. By contrast, the $5 \times 5 \times 5$ [mm^3] cubes were directly indented on the original surfaces. All the tested surfaces were polished beforehand with P1200 silicon carbide paper. For each test, a pyramidal indenter (see figure 3.13) was pressed during 10 [sec] onto the material with a load of 10 [kg]. The indentation durations were measured with a digital timer and the tests were stopped manually. The two diagonals lengths of the resulting indents were then evaluated using a ruler on the screen of the machine, which displays the image of the sample's surface that is captured by an embedded optical microscope.

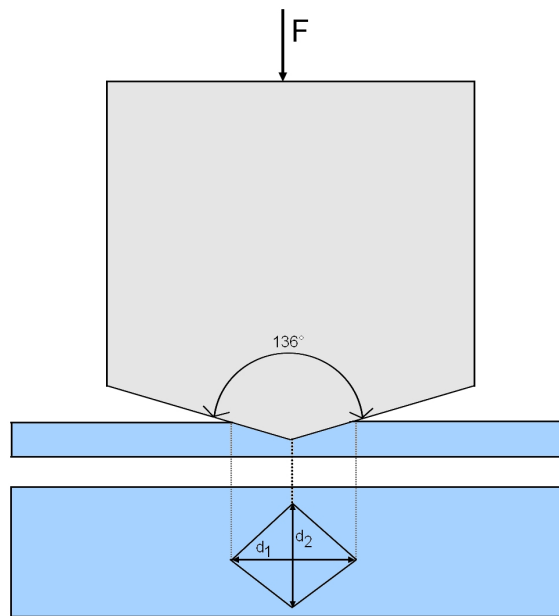


FIGURE 3.13: Schematic representation of the Vickers hardness test

Three to ten tests were made for each sample and the mean diagonal length value was computed for every test. The corresponding Vickers hardness values H_v could

then be estimated by means of a conversion table (see C).

Tensile tests

The tensile tests were performed on a *RetroLine testControl II* screw-driven electro-mechanical testing system manufactured by *Zwick Roell*. It works in the following manner:

- The cylindrical specimen is clamped on its extremities with grips. Both of them are fixed to a cross head (see figure 3.14).
- Parameters are selected thanks to a software connected to the machine: One must enter the extensometer initial gauge length L_0 , the cross head speed and the pre load (used to limit the backlash in the assembly). The initial minimal value d_o for the specimen diameter is also measured with a digital calliper and specified in the program.
- The contact extensometer is placed on the sample. Its purpose is to measure the length change ΔL during the test.
- The lower cross head goes down. This induces a force F and a displacement in the specimen, both of which are saved in an *Excel* file. The test goes on until the fracture of the specimen occurs, unless if it is stopped beforehand.

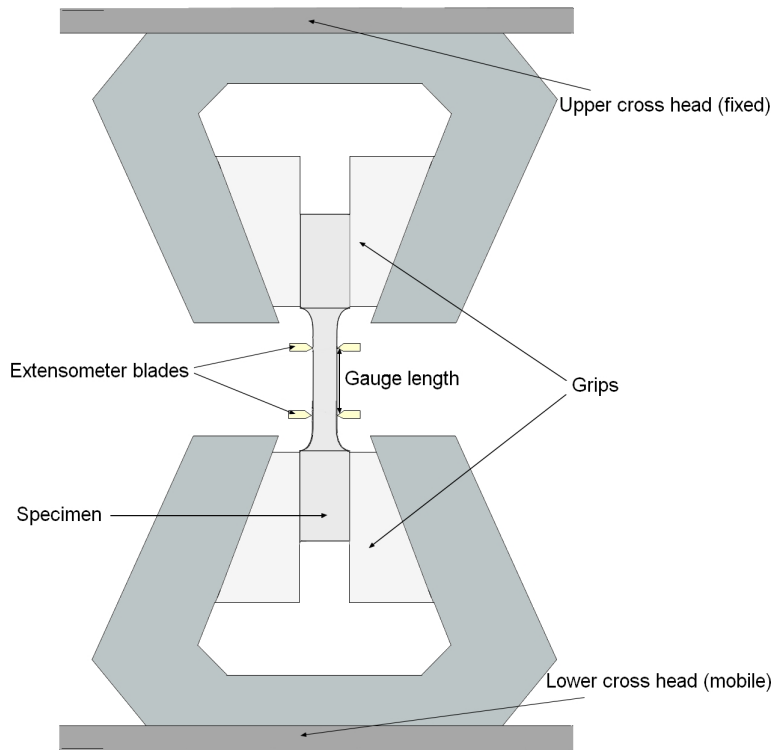


FIGURE 3.14: Schematic representation of the tensile test mounting

The tensile specimens used all originated from batch X200-190417. They were manufactured using the optimised set of parameters: $P = 0.75\%P_{max}$ and $v_s = 1200[\frac{mm}{s}]$. Their minimal diameter is equal to 6 [mm]. Further details about their geometry and heat treatments can be consulted respectively in sections 3.2 and 3.3. For each test, the extensometer gauge length was set to 18 [mm]. This is approximately the maximal possible value, given the short length of the specimens. A pre load of 15 [N] was adopted and a cross head speed of 1 [$\frac{mm}{min}$] was chosen in accordance with what had been done in a previous work at UCL. It was decided to interrupt the tensile tests of one AB specimen and of two others - that underwent heat treatments at 200°C and 300°C. In that way, the damage mechanisms could be observed afterwards. Table 3.3 regroups the strain limits at which the tests were stopped. They correspond roughly to the onset of necking.

Sample	Strain limit [-]
X200-180417-3	0.01
X200-180417-6	0.06
X200-180417-9	0.08

TABLE 3.3: Strain limits for interrupted tensile tests of batch X200-180417 specimens

A tensile test can be used to compute multiple properties. First of all, the engineering stress (σ_{eng}) and strain (ϵ_{eng}) were computed at each time step for every tested samples. The formulas below were used:

$$\sigma_{eng} = \frac{F}{A_0} = \frac{F}{\frac{\pi d_0^2}{4}}$$

$$\epsilon_{eng} = \frac{\Delta L}{L_0} = \frac{L - L_0}{L_0}$$

On the basis of the stress-strain curve, the following characteristics could be computed:

- The Young's modulus E: it is used to characterize the stiffness of a material. The tested specimen first deforms elastically, which corresponds to a linear strain-strain relationship. The slope value for the corresponding part of the curve is E. It is found via numerical linear regression in the ϵ_{eng} between 0 and $\simeq 0.1[\%]$.
- The elastic limit σ_y : it is the σ_{eng} at which the plastic strain (non-linear) becomes non negligible. The 0.2 [%] criterion was used. In this manner, σ_y is found as the intersection of the stress-strain curve with the line of slope E passing through point $(\epsilon, \sigma)=(0.2[\%], 0[MPa])$.
- The ultimate tensile strength σ_u : it is simply the maximal σ_{eng} attained during the test.

- The strain at fracture ϵ_f : in the case of fragile fracture, the value of ϵ_{eng} at the end of the test could be used. However, if the specimen underwent a necking mechanism - as there is strain localisation - the final ϵ does not constitute a good approximation. In that case, the specimen final minimal diameter d_f was measured with a profile projector. The true final strain $\epsilon_{f,true} = \ln(\frac{L_f}{L_0})$ could then be computed using the volume conservation hypothesis:

$$L_0 \cdot A_0 = L_f A_f$$

which implies that $\epsilon_{f,true} = \ln(\frac{A_0}{A_f}) = \ln(\frac{d_0^2}{d_f^2})$. All the properties mentioned above are illustrated in figure 3.15.

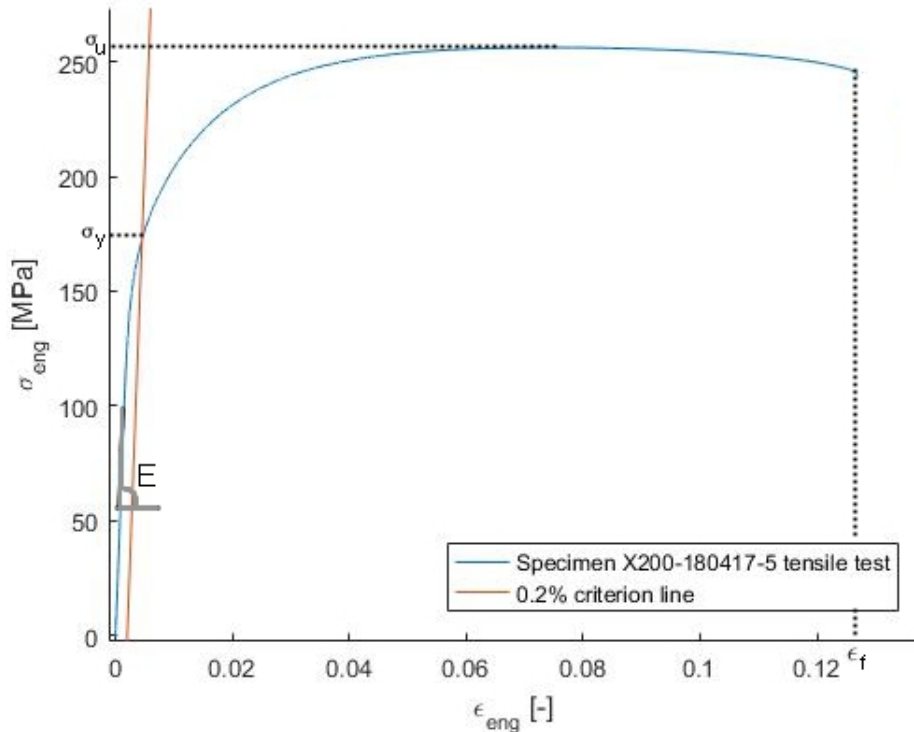


FIGURE 3.15: Tensile stress-strain curve for specimen X200-180417-5 with annotated key features

Chapter 4

Results

4.1 Powder ageing

4.1.1 Grain size and distribution

The evolution of powder size distribution during the year, measured without any prior ultrasonic treatment, is available in figure 4.1. Each plotted curve was averaged based on four measurements. The mean diameter (D_a) varied between 31.5 and 36.8 [μm], corresponding respectively to the last and first samplings. The standard deviation (SD) stayed between 14.8 and 16.2 [μm]. Details for the samplings conditions are available in table 4.1. The grain size testing method demonstrated high reproducibility. For each sample, the curves for the four measurements seemed to overlap perfectly when observed at the scale of figure 4.1.

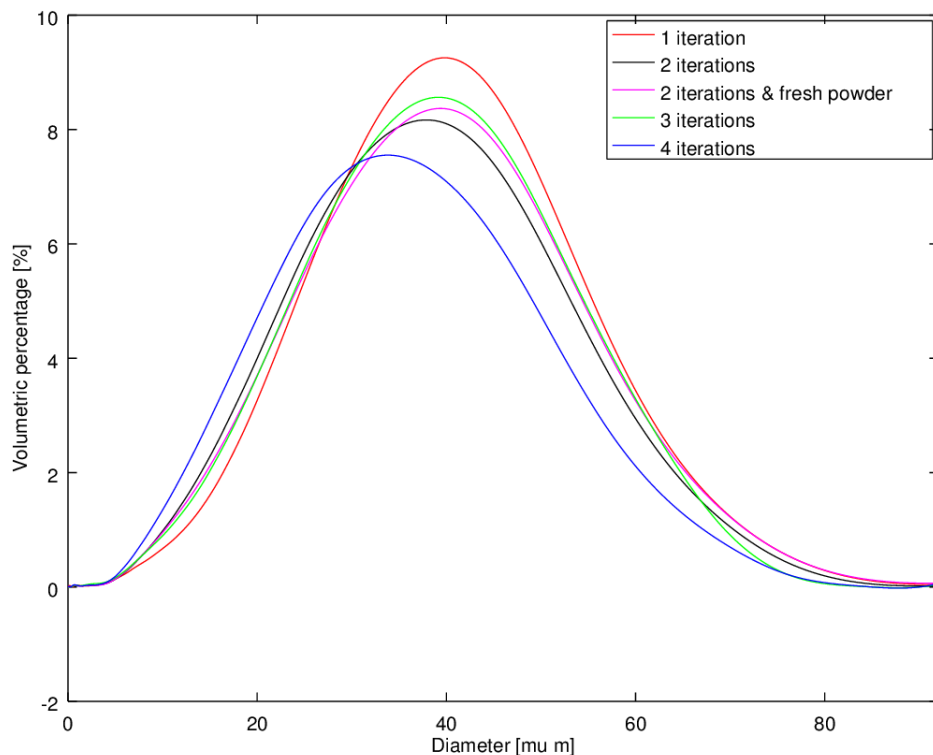


FIGURE 4.1: Evolution of powder size distributions with recycling iterations before ultrasonic treatments.

Date of sampling	Number of recycling iterations	Prior addition of fresh powder	Batches
23/10/2017	1	No	X200-171024
09/01/2018	2	No	X200-180109
21/02/2018	2	Yes	X200-180220
13/03/2018	3	No	X200-180313
			X200-180315
			X200-180319
17/04/2018	4	No	X200-180417

TABLE 4.1: Powder samplings recycling history

Mean diameters and standard deviations were compared before and after exposure to ultrasounds (US). Results are gathered in table 4.2 with the 95% confidence intervals (CI). In both cases, a general progressive decrease of the mean diameter and a narrowing of the distribution was observed as functions of the number of recycling cycles. The only exception to this trend is the distribution for February sample. This particular sampling was made the day after fresh powder was added to the recycled one. US caused a systematic decrease of $\simeq 10\%$ for D_a , exception made for the April sampling (only 6%). Ultrasonic treatment permitted to lower the maximal diameter measured from 134 to 84 [μm].

Date of sampling	Before US		After US	
	D_a	SD	D_a	SD
23/10/2017	36.8 ± 0.1	15.5 ± 0.0	33.3 ± 0.0	14.6 ± 0.0
09/01/2018	34.5 ± 0.1	15.5 ± 0.1	31.4 ± 0.0	14.6 ± 0.0
21/02/2018	35.5 ± 0.2	16.2 ± 0.3	32.1 ± 0.1	14.9 ± 0.0
13/03/2018	35.0 ± 0.0	15.2 ± 0.0	31.6 ± 0.1	14.5 ± 0.0
17/04/2018	31.5 ± 0.1	14.8 ± 0.0	29.6 ± 0.0	14.3 ± 0.0

TABLE 4.2: Average powder diameter and standard deviation before and after ultrasonic treatment

4.1.2 Composition

Fresh powder

The composition of fresh (unrecycled) powder measured by ICP spectrometry is shown in table 4.3. Each mass fraction is vitiated by a relative error than can go up to 3%. The method thus gives far more precise results for elements in smaller quantities.

Al [%wt]	Fe [%wt]	Mg [%wt]	Si [%wt]
89.0 ± 2.67	0.14 ± 0.004	0.50 ± 0.015	9.99 ± 0.300

TABLE 4.3: Composition of the fresh AlSi10Mg powder

Recycled powder

The reiterations of this analysis on the recycled powder used for different batches gave the results in table 4.4. The samples tested were the same as for the grain sizes analysis (see table 4.1). Mass fractions as a function of time are displayed on figure 4.2, with the corresponding error bars. There appears to be a peak of alloying elements mass fractions for February sample. It seems that these quantities drop progressively the following two months. However, these assertions should be taken with a grain of salt due to the large error bars.

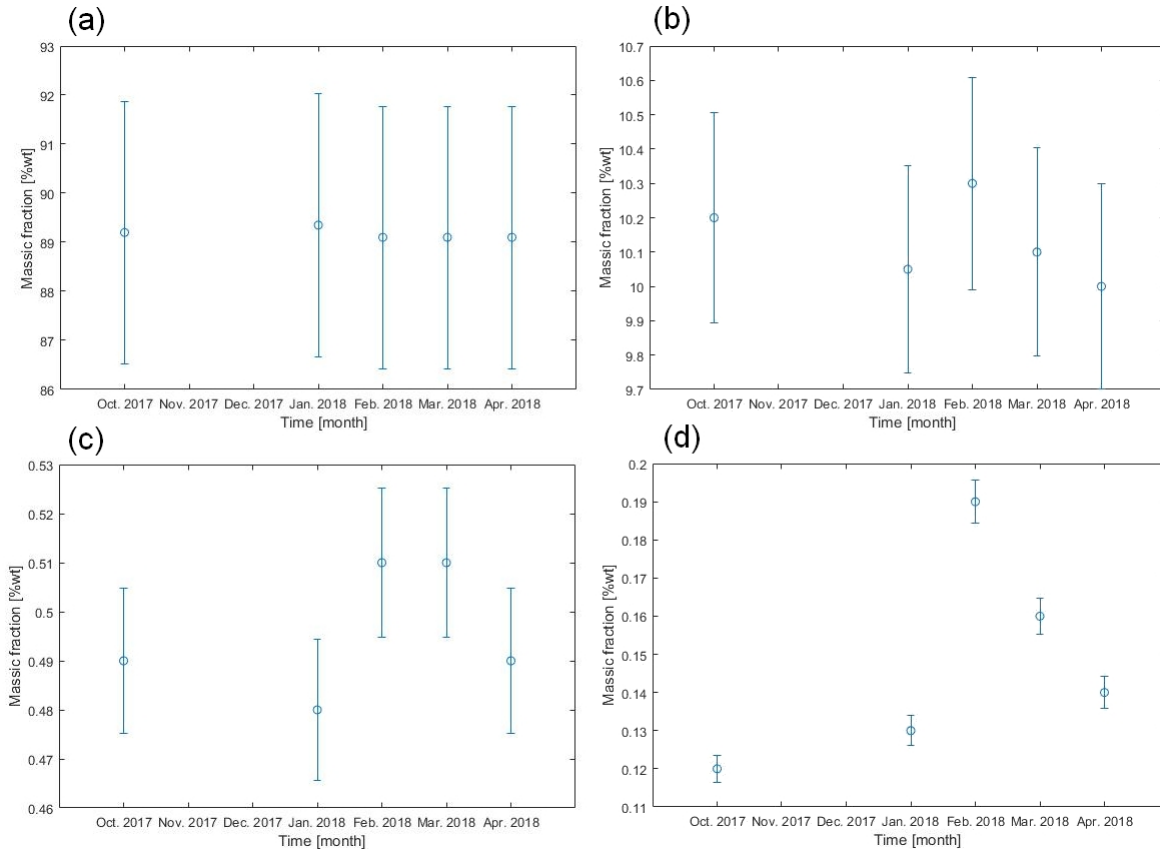


FIGURE 4.2: Evolution of concentration of the recycled powder constituting elements: (a) aluminium mass fraction (b) silicon mass fraction (c) magnesium mass fraction (d) iron mass fraction

Date of sampling	Composition [%wt]			
	Al	Fe	Mg	Si
23/10/2017	89.2 ± 2.67	0.12 ± 0.004	0.49 ± 0.015	10.2 ± 0.3
09/01/2018	89.3 ± 2.67	0.13 ± 0.004	0.48 ± 0.014	10.1 ± 0.3
21/02/2018	89.1 ± 2.67	0.19 ± 0.006	0.51 ± 0.015	10.3 ± 0.3
13/03/2018	89.1 ± 2.67	0.16 ± 0.005	0.51 ± 0.015	10.1 ± 0.3
17/04/2018	89.1 ± 2.67	0.14 ± 0.004	0.49 ± 0.015	10.0 ± 0.3

TABLE 4.4: Composition of recycled AlSi10Mg powder as a function of the date

SLM processed material

Two samples of batch X200-171024 were machined in order to extract material chips to use for ICP analysis. The composition after completion of the SLM process could thus be compared with the original one (sampled the 23/10/2017). Table 4.5 shows the results for both. A relative loss of a few percent was measured for magnesium (between 3.5% and 4.7 %). It seems that the mass fraction of silicon also decreased (of $\simeq 1\%$) but this is uncertain due to the large error bars.

Sample	Composition [%wt]			
	Al	Fe	Mg	Si
5	89.6 ± 2.67	0.13 ± 0.004	0.47 ± 0.015	9.89 ± 0.300
7	89.5 ± 2.67	0.12 ± 0.004	0.48 ± 0.015	9.90 ± 0.300

TABLE 4.5: Compositions of the chips extracted from samples "5" and "7" from batch X200-171024

4.2 Density and hardness study

4.2.1 Optimisation of the SLM parameters

The optimisation of the manufactured samples properties was done with respect to $\rho_{a,rel}$ and H_v . For this purpose, twelve cubes were made with P varying from 75% P_{max} to P_{max} and v_s from 900 to 1500 [$\frac{mm}{sec}$]. Details about batch X200-171024 are given in appendix A. The goal of this optimisation was to select a single set of parameters values to use in the rest of the thesis. The parameters values were chosen to cover a wide range of E_d . Sets of parameters ($P = 75\%P_{max}$; $v_s = 1200[\frac{mm}{sec}]$) and ($P = 75\%P_{max}$; $v_s = 900[\frac{mm}{sec}]$) gave the best results in terms of $\rho_{a,rel}$ in a previous study done at UCL. It was decided to produce samples with these sets of values in triplicate in order to have a first insight on the process reproducibility. This will be discussed further in next section. Here, only the mean H_v and $\rho_{a,rel}$ of those samples will be compared to the others.

Results for the measurements of $\rho_{a,rel}$ and H_v are summarised in figure 4.3 and detailed in appendix A. The 95% confidence intervals (CI) are drawn on the graphs. The methods used to compute them are described in appendix D. All apparent relative density values were obtained through hydrostatic weighing of the unpolished AB specimens.

Both $\rho_{a,rel}$ and H_v reached maximal values for ($P = 75\%P_{max}$; $v_s = 1200[\frac{mm}{sec}]$). It was thus chosen to work with this optimal set of parameters values in the rest of the thesis. The graph then shows a general progressive decrease of $\rho_{a,rel}$ and H_v for $E_d > 57[\frac{J}{mm^3}]$. Two samples were manufactured using the same energy density ($E_d \simeq 86.1$) but with different P and v_s . The lower density and hardness at this E_d value on graph 4.3 both correspond to the parameters values ($P = P_{max}$; $v_s = 1059[\frac{mm}{sec}]$).

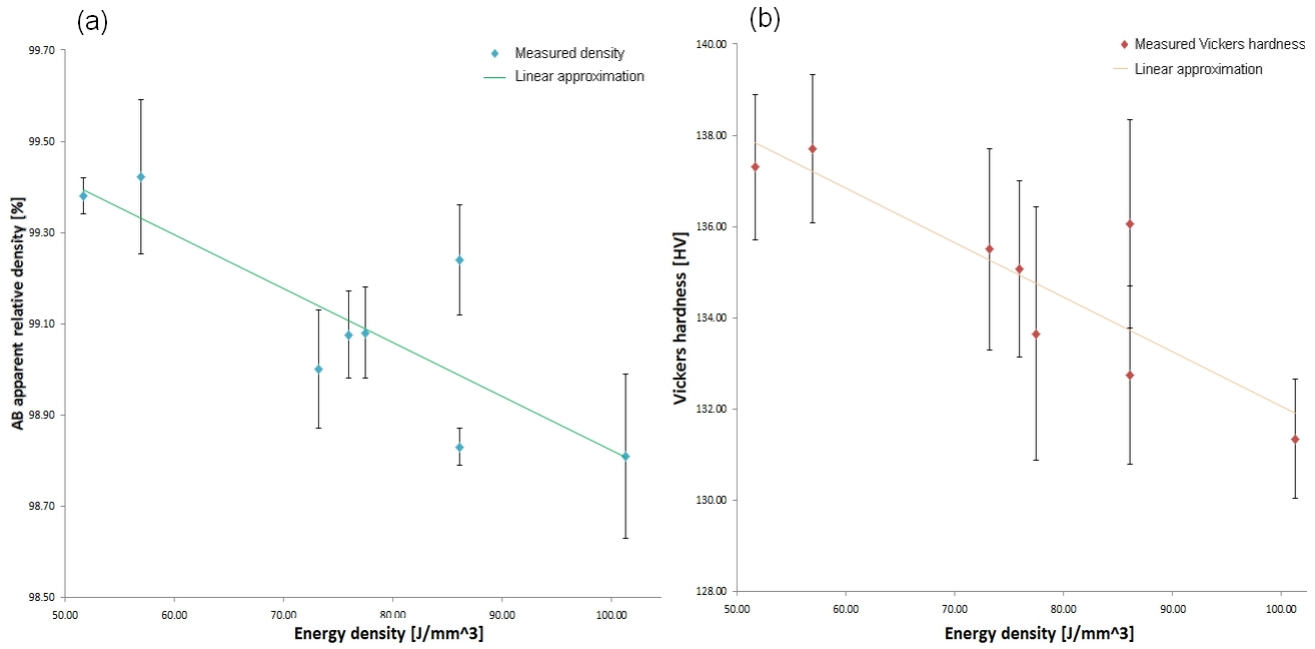


FIGURE 4.3: Batch X200-171024 samples properties as a function of the energy density: (a) as-built apparent relative density (b) Vickers hardness

4.2.2 Reproducibility

General results

Batch X200-171024 raised a reproducibility issue. Sample "8a", manufactured with parameters ($P = 75\%P_{max}$; $v_s = 900[\frac{mm}{sec}]$), had a relative density $\simeq 5\%$ lower than the others' ($\rho_{a,rel} = 98.77\%$). It was decided to produce a batch of fifteen ($P = 75\%P_{max}$; $v_s = 1200[\frac{mm}{sec}]$) cubic samples and fifteen ($P = 75\%P_{max}$; $v_s = 900[\frac{mm}{sec}]$) others in order to assess the process reproducibility when using a same powder. It was chosen to work with the two sets of parameters to compare the results for optimal and sub-optimal set values, and to try understanding the conditions that caused the poor properties sample "8a". Part of the samples were positioned closely to one another (see A.4) to see if the specimens rapprochement has any effect on their final properties. The distance between two adjacent cubes in the same row (that is quasi-aligned with y) was $\simeq 50[mm]$. The distance separating the rows was $\simeq 70[mm]$. The apparent relative density was once more measured with the unpolished AB samples.

Type	$\bar{\rho}_{a,rel}$ [%]	$SD_{\rho_{a,rel}}$ [%]	\bar{H}_v [HV]	SD_{H_v} [HV]
($P = 75\%P_{max}$; $v_s = 1200[\frac{mm}{sec}]$)	99.42	0.08	138	0.4
($P = 75\%P_{max}$; $v_s = 900[\frac{mm}{sec}]$)	99.08	0.27	135	1.3

TABLE 4.6: Average values and standard deviations for apparent relative densities and hardnesses of the specimens of batch X200-171024

Hardness and apparent relative density results for batch X200-180109 are shown in appendix A. The key information is displayed in tables 4.7 and 4.8. Type ($P = 75\%P_{max}$; $v_s = 900[\frac{mm}{sec}]$) samples exhibited slightly poorer properties than type ($P = 75\%P_{max}$; $v_s = 1200[\frac{mm}{sec}]$) ones in average. However, the former have far better properties to what one could have expected based on previous results (see table 4.6). The highest measured density is 99.54 [%].

Type	$\bar{\rho}_{a,rel}$ [%]	$SD_{\rho_{a,rel}}$ [%]	\bar{H}_v [HV]	SD_{H_v} [HV]
($P = 75\%P_{max}$; $v_s = 1200[\frac{mm}{sec}]$)	99.40	0.09	139.9	0.87
($P = 75\%P_{max}$; $v_s = 900[\frac{mm}{sec}]$)	99.36	0.11	138.3	1.3

TABLE 4.7: Average values and standard deviations for apparent relative densities and hardnesses of types the specimens of batch X200-180109

Type	$min(\rho_{a,rel})$ [%]	$max(\rho_{a,rel})$ [%]	$min(H_v)$ [HV]	$max(H_v)$ [HV]
($P = 75\%P_{max}$; $v_s = 1200[\frac{mm}{sec}]$)	99.24	99.52	138.6	141.4
($P = 75\%P_{max}$; $v_s = 900[\frac{mm}{sec}]$)	99.18	99.54	134.6	140.4

TABLE 4.8: Minimal and maximal values for apparent relative densities and hardnesses of the specimens of batch X200-180109

Sample proximity and position influence

The results are displayed in figure 4.4 as functions of the (x,y) positions of the samples on the manufacturing plate. The coordinates are such that the roll sweeps were done in the positive x direction during the process. Other graphs showing the averaged $\rho_{a,rel}$ and H_v as functions of the x and y coordinates were also plotted. The samples distanced from less than 1 [cm] along x or y were considered to have the same corresponding coordinate. The graphs are shown in appendix E. No significant trend was observed on these graphs: the variations of hardnesses and relative densities are too small compared to the CI.

A comparison of the results for closely packed samples ($y < 6$) and distant ones ($y > 6$) was also carried out. The details are shown in tables 4.9 and 4.10. Again, no significant distinction could be drawn between the two.

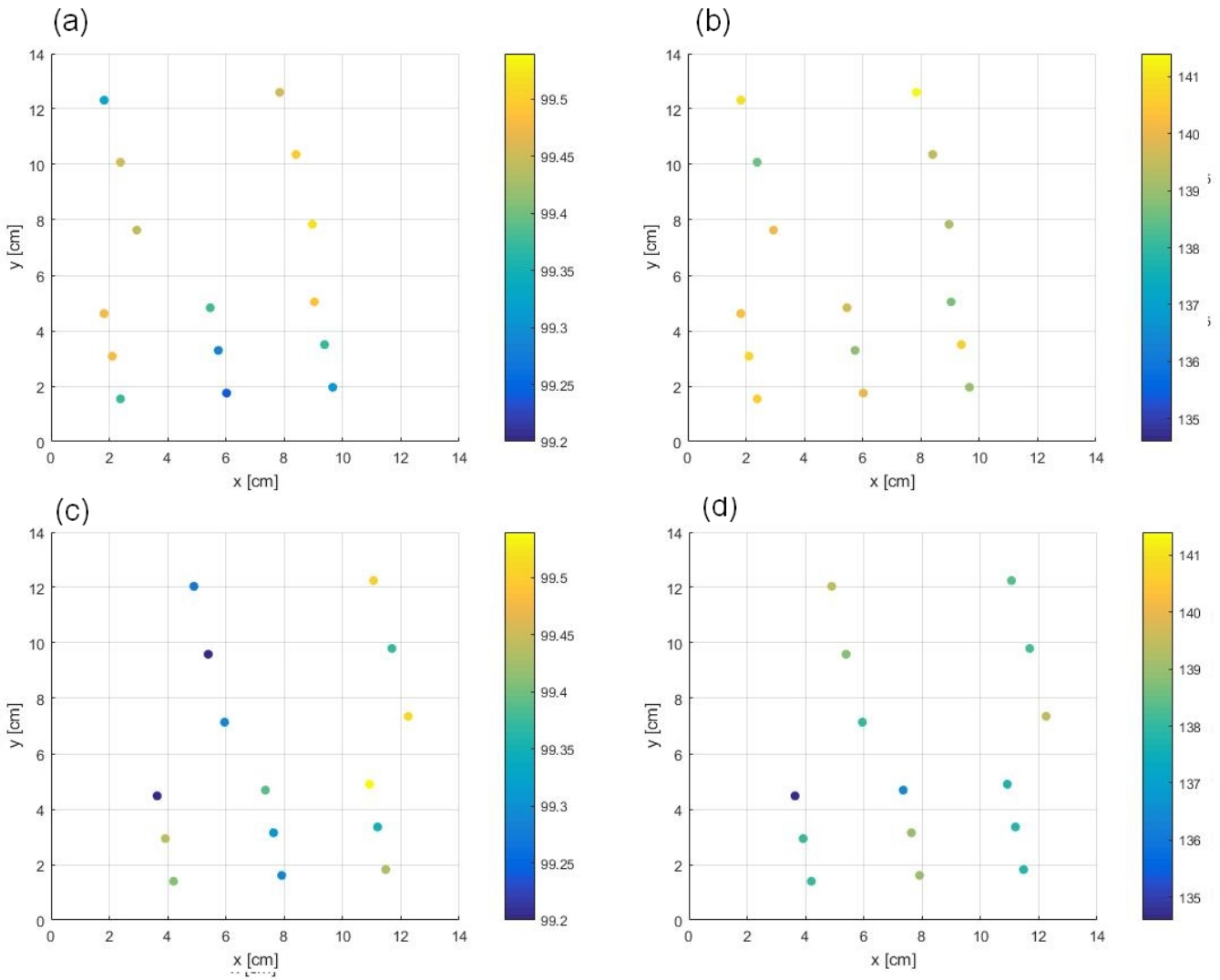


FIGURE 4.4: Batch X200-180109 scatter plots as functions of the (x,y) position on the manufacturing plate: (a) type ($P=0.75\% P_{max}$; $v_s=1200 \frac{mm}{sec}$) apparent relative densities (b) type ($P=0.75\% P_{max}$; $v_s=1200 \frac{mm}{sec}$) hardnesses (c) type ($P=0.75\% P_{max}$; $v_s=900 \frac{mm}{sec}$) apparent relative densities (d) type ($P=0.75\% P_{max}$; $v_s=900 \frac{mm}{sec}$) hardnesses

Type	Position	$\bar{\rho}_{a,rel}$ [%]	$SD_{\rho_{a,rel}}$ [%]	\bar{H}_v [HV]	SD_{H_v} [HV]
$(P = 75\% P_{max}; v_s = 1200 [\frac{mm}{sec}])$	y>6	99.45	0.07	140.0	1.1
	y<6	99.38	0.07	139.9	0.7
$(P = 75\% P_{max}; v_s = 900 [\frac{mm}{sec}])$	y>6	99.36	0.10	138.7	0.6
	y<6	99.37	0.08	138.0	1.6

TABLE 4.9: Average values and standard deviations for apparent relative densities and hardnesses of types the specimens of batch X200-180109, with distinction between the closely packed samples and the others

Type	Position	$\min(\rho_{a,rel}) [\%]$	$\max(\rho_{a,rel}) [\%]$	$\min(H_v) [\text{HV}]$	$\max(H_v) [\text{HV}]$
$(P = 75\% P_{max}; v_s = 1200[\frac{mm}{sec}])$	y>6	99.33	99.52	138.6	141.4
	y<6	99.24	99.49	138.7	140.9
$(P = 75\% P_{max}; v_s = 900[\frac{mm}{sec}])$	y>6	99.20	99.51	138.0	139.5
	y<6	99.29	99.54	134.6	140.4

TABLE 4.10: Minimal and maximal values for apparent relative densities and hardnesses of the specimens of batch X200-180109

Scan order influence

The apparent relative densities, Vickers hardnesses and the corresponding 95 % CI are displayed as functions of the scan order in figure 4.5. The period of time between two successive scans of powder layers is the same for every sample. However, the time span between the scan and the powder covering differs from one to the other. This could lead to differences in terms of thermal exchanges.

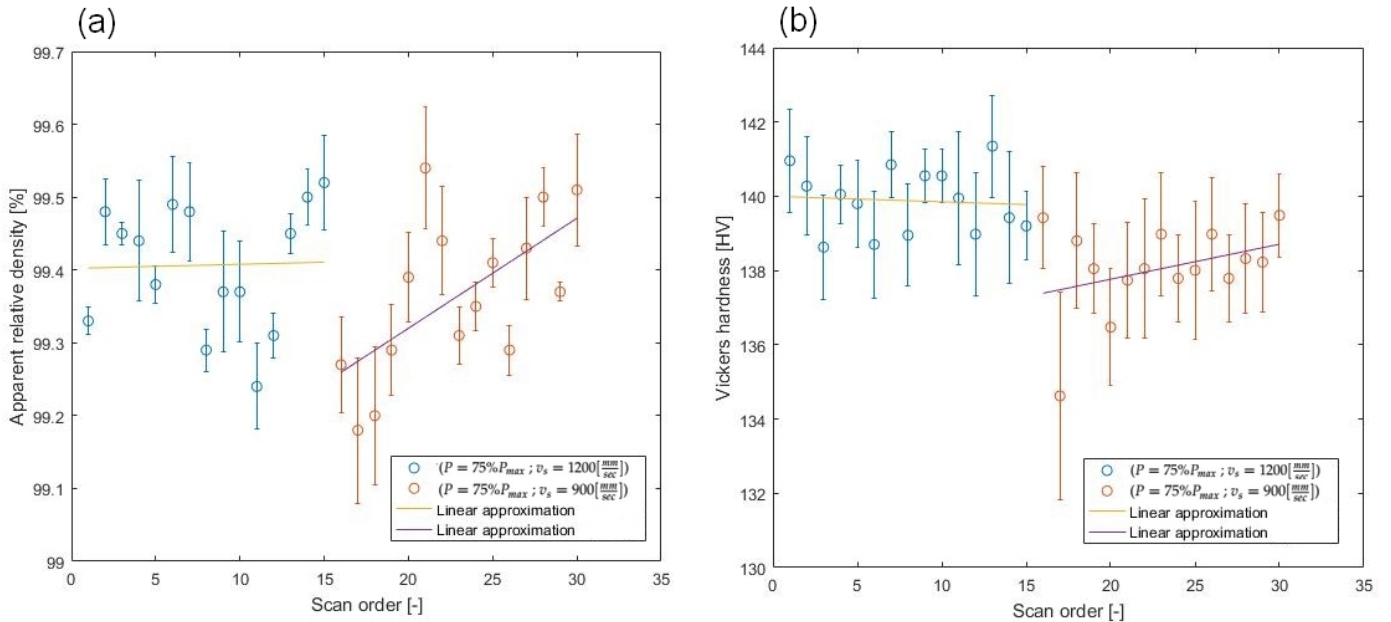


FIGURE 4.5: Batch X200-180109 scatter plots as functions of the scan order of (a) the apparent relative densities (b) the Vickers hardnesses

Only one trend can be noted: the density of the ($P = 75\%P_{max} ; v_s = 900[\frac{mm}{sec}]$) samples appears to be larger for later scanning. However, this doesn't help understanding the poorer properties measured for samples with the same parameters in batch X200-171024 as they were precisely the last scanned.

Powder influence

The hardnesses and relative densities of samples manufactured using the optimised parameters ($P = 75\%P_{max} ; v_s = 1200[\frac{mm}{sec}]$) were monitored throughout this whole work. In this way, it was possible to study the impact of the powder ageing. Control cubes of dimensions $10 \times 10 \times 10 [mm^3]$ were produced in multiple batches for that purpose. The average measurements for those samples are gathered in table 4.11. Detailed information is given in appendix A.

¹Measured by HW (AB)

²Measured by HW (polished)

³Measured by RODIA

Batch	$\rho_{a,rel}$ ¹ [%]	$\rho_{a,rel}$ ² [%]	ρ_{rel} ³ [%]	H_v [HV]
X200-171024	99.42	-	-	137.7
X200-180109	99.40	99.51	99.59	139.9
X200-180319	-	99.75	99.84	139.8
X200-180417	-	99.47	99.67	136.0

TABLE 4.11: Average hardness and relative density measurements for the control cubes of each batch

Samples from batches X200-180222 and X200-180228 are not included in this section. In those cases, fresh steamed powder was used, which induced high porosity in the produced parts. The most reasonable explanation is that the powder processing caused the formation of aggregates. This was not investigated further, and only recycled powder was employed thereafter. Table 4.11 indicates that the relative density peaked with batch X200-170319. It dropped slightly afterwards with batch X200-170417. Hardness also decreased - more significantly - with this last batch.

Melt pools sizes and distribution study

Samples "8a" and "8b" of batch X200-171024 were made using the same manufacturing parameters. However, the former had way lower $\rho_{a,rel}$ and H_v (see appendix A). A statistical analysis of the melt pools size distribution was conducted for both samples to try grasping a better understanding of the origin of the differences. The procedure described in section 3.4.2 was followed. 130 zones were manually delineated for both samples. An illustration of the zones subdivision is shown on figure 4.6.

In both cases, the area of every zone was computed. Melt pools areas histograms are displayed on figure 4.7. Even though the mean areas are nearly the same, the distributions are quite different (see table 4.14). The standard deviation for sample "8b" is approximately 50[%] bigger than for "8a" one. The corresponding picture contains significantly more melt pools with small areas ($<200 \text{ } [\mu\text{m}^2]$) and large ones ($>1000 \text{ } [\mu\text{m}^2]$).

Sample	Mean area $[\mu\text{m}^2]$	SD $[\mu\text{m}^2]$
"8a"	$4.6629 \cdot 10^3$	$2.3625 \cdot 10^3$
"8b"	$4.6597 \cdot 10^3$	$3.9285 \cdot 10^3$

TABLE 4.12: Summary of the melt pools areas distributions for samples "8a" and "8b"

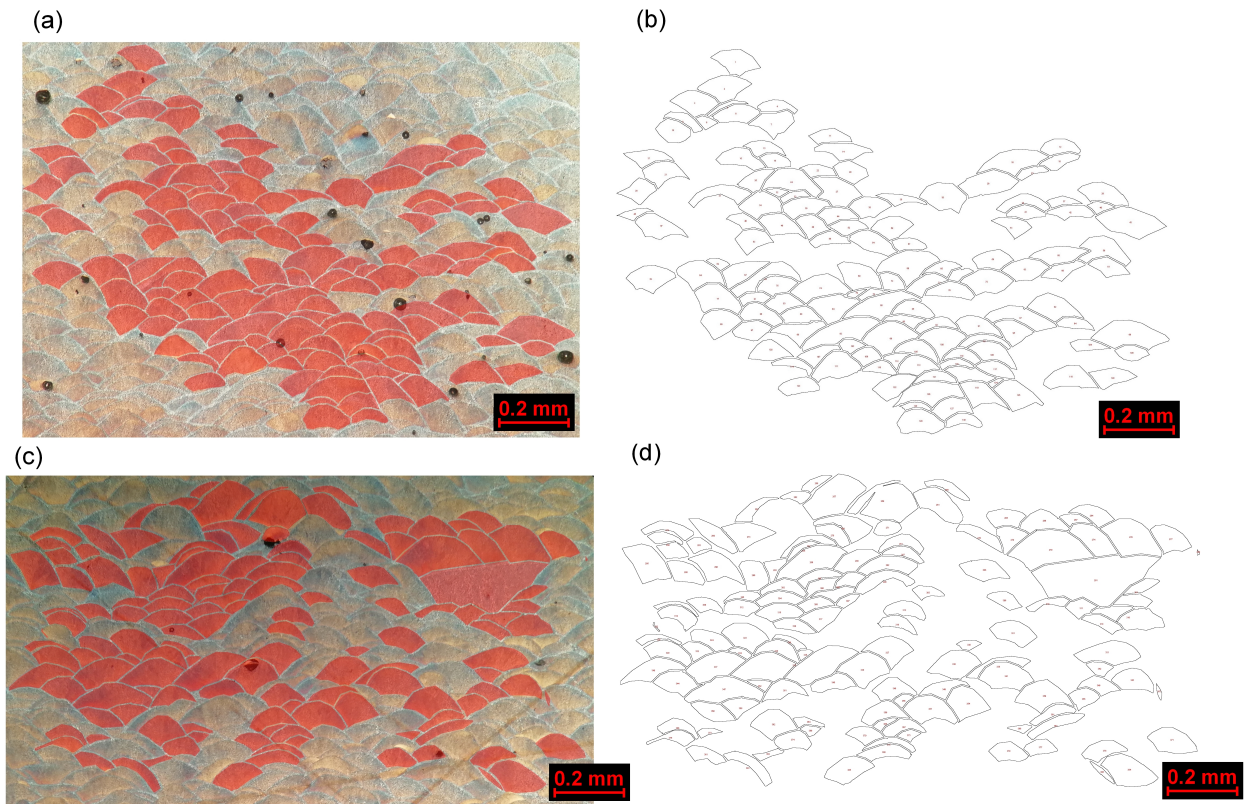


FIGURE 4.6: Screen captures of (a) melt pools subdivision from a picture of specimen "8a" (b) *ImageJ* partitioning from the same picture of specimen "8a" (c) melt pools subdivision from a picture of specimen "8b" (d) *ImageJ* partitioning from the same picture of specimen "8b"

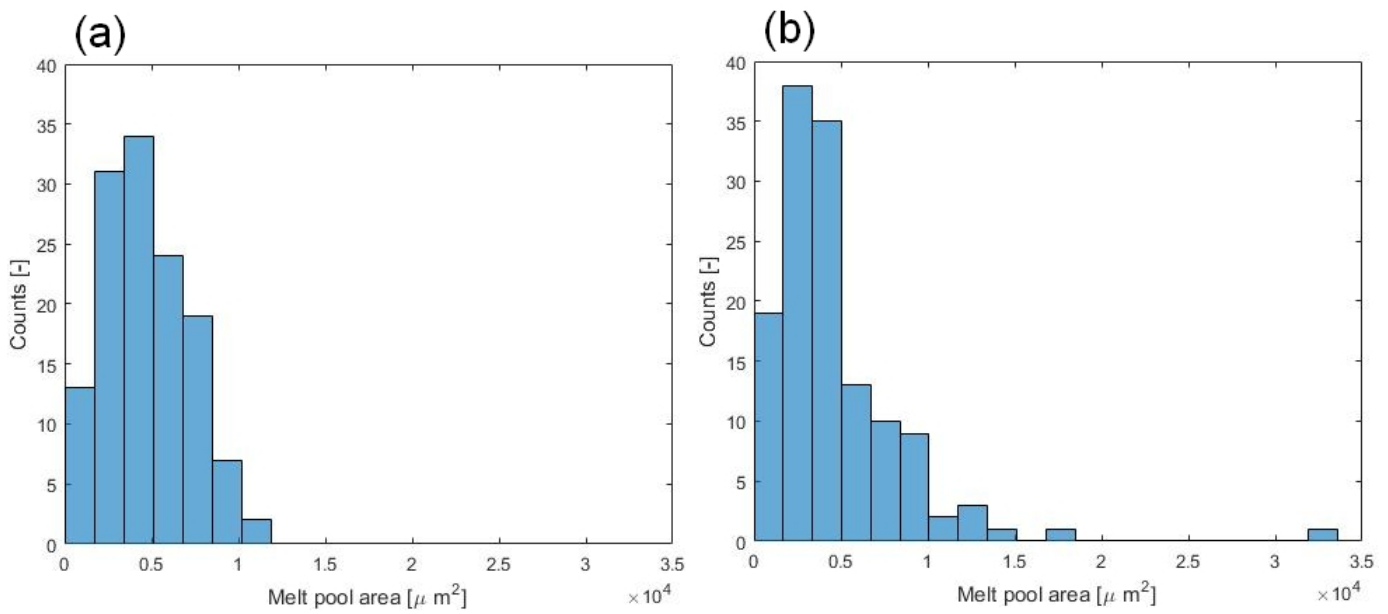


FIGURE 4.7: Histograms of melt pools areas occurrences from *ImageJ* partitioning of (a) sample "8a" b) sample "8b"

4.2.3 Homogeneity along the z direction

As mentioned in section 3.2, all tensile specimens were built vertically. Their heights are significantly greater than the other samples'; respectively 6 [cm], and 1 [cm] or less. It was chosen to cut up specimen X200-180417-25 into slices to measure if the density and hardness were homogeneous along the Z direction in the material. The surfaces analysed were named according to their original Z position in the specimen with either "B", "C1" , "C2", "C3" or "T" (for bottom, center and top) and to the test done with a letter "D" or "H" (for density and hardness). The denomination is summarised in figure 4.8.

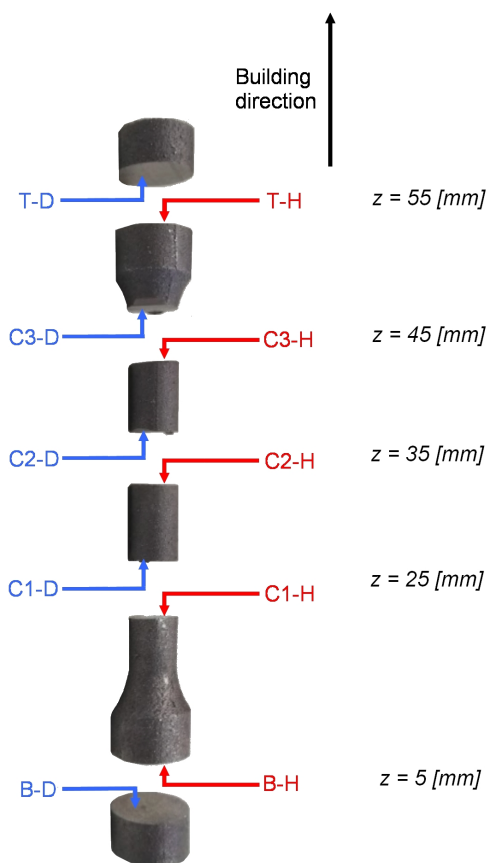


FIGURE 4.8: Specimen X200-180417-25 sub-parts and surfaces denomination.

Results are shown in figure 4.9. No general trend could be observed with respect to hardness. The measured values are high and closely packed except for the "B" surface, which exhibited a significantly lower hardness. Density values are all equal or above 99.75 [%]. The values at the center of the sample were slightly lower to the extremities'. A summary of the results is displayed in table 4.13.

Property	Average value	Minimum	Maximum	Standard deviation
Relative density [%]	99.80	99.75	99.87	0.05
Hardness [HV]	138.0	132.2	141.7	3.5

TABLE 4.13: Relative density and hardness results summary for specimen X200-180417-25 surfaces

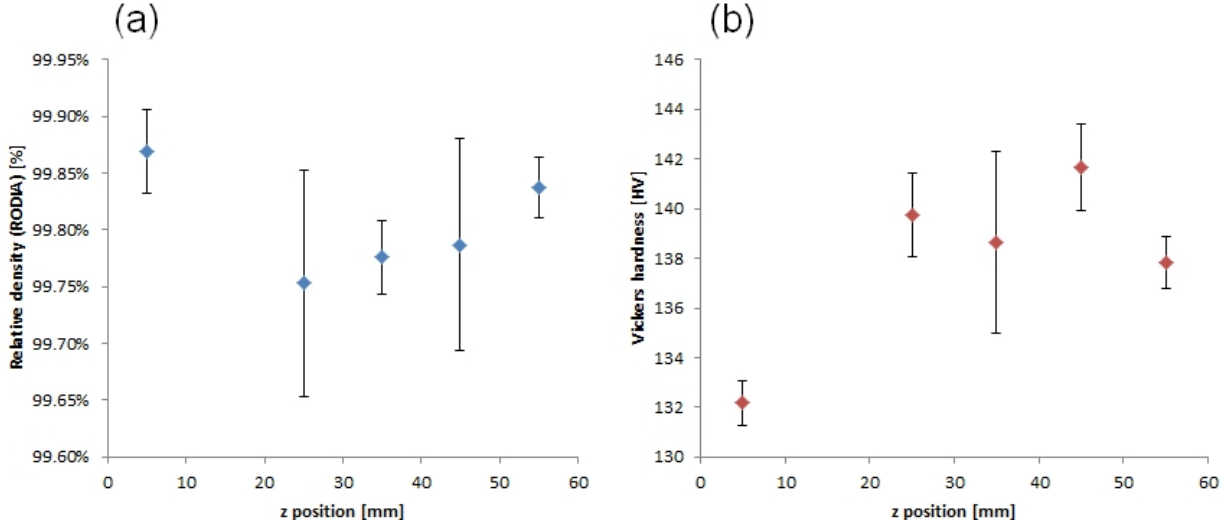


FIGURE 4.9: Scatter plots of the results for specimen X200-180417-25 surfaces as a function of the vertical position: (a) RODIA based relative density (b) Vickers hardness

4.3 In-depth characterisation of the as-built samples

4.3.1 Mechanical properties

The average tensile properties of the six tested as-built specimens are displayed in table 4.14. Detailed information may be consulted in appendix B. All data was computed based on the procedures of section 3.4.4. A typical curve is shown on figure 4.10.

E [GPa]	σ_y [MPa]	σ_u [MPa]	ϵ_f [%]
64.9 ± 3.0	266.6 ± 23.6	381.7 ± 24.7	2.5 ± 0.5

TABLE 4.14: Average tensile mechanical properties of the as-built specimens from batch X200-180417

One specimen built with no contour scanning strategy was tested. Its tensile behaviour was observed to be very similar to the other samples. No distinction shall thus be made between the two types in what follows. Stress-strain curve for specimen X200-180417-1 was non-linear before the plasticity regime started. This is due to slippage in the grips. The obtained Young's modulus for the test was thus not taken into account for the computation of the average value.

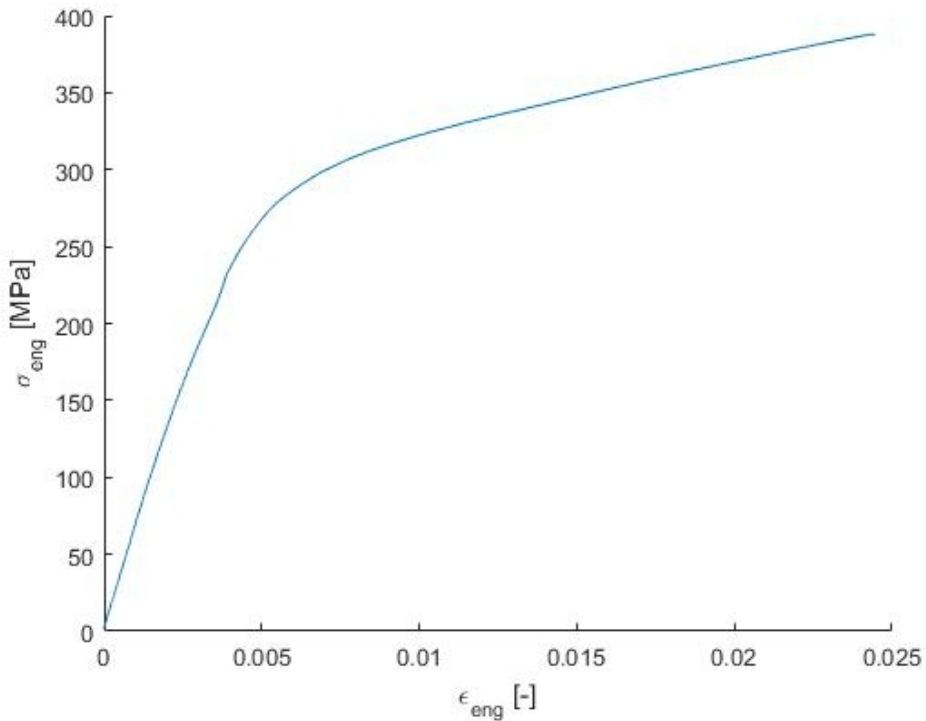


FIGURE 4.10: Engineering tensile stress-strain curve for specimen X200-180417-2

No necking phenomena was observed among all tensile tests for AB samples. The Considere criterion was used for the detection of plastic instability. It states that necking starts at $\frac{d\sigma_{true}}{d\varepsilon_{true}} = \sigma$, which is equivalent to $\frac{d\sigma_{eng}}{d\varepsilon_{eng}} = 0$. The latter condition was not satisfied for any AB engineering stress-strain curve.

4.3.2 Microstructure

The presence of these 3 zones makes it impossible to give a single representative value to represent the size of the whole microstructure. The equiaxed cells from the fine zone core have a mean size below 1 μm , lying generally between 0.4 and 0.7 μm . The coarse zone at the melt pool boundary presents slightly larger cells with a size between 0.8 and 1.2 μm .

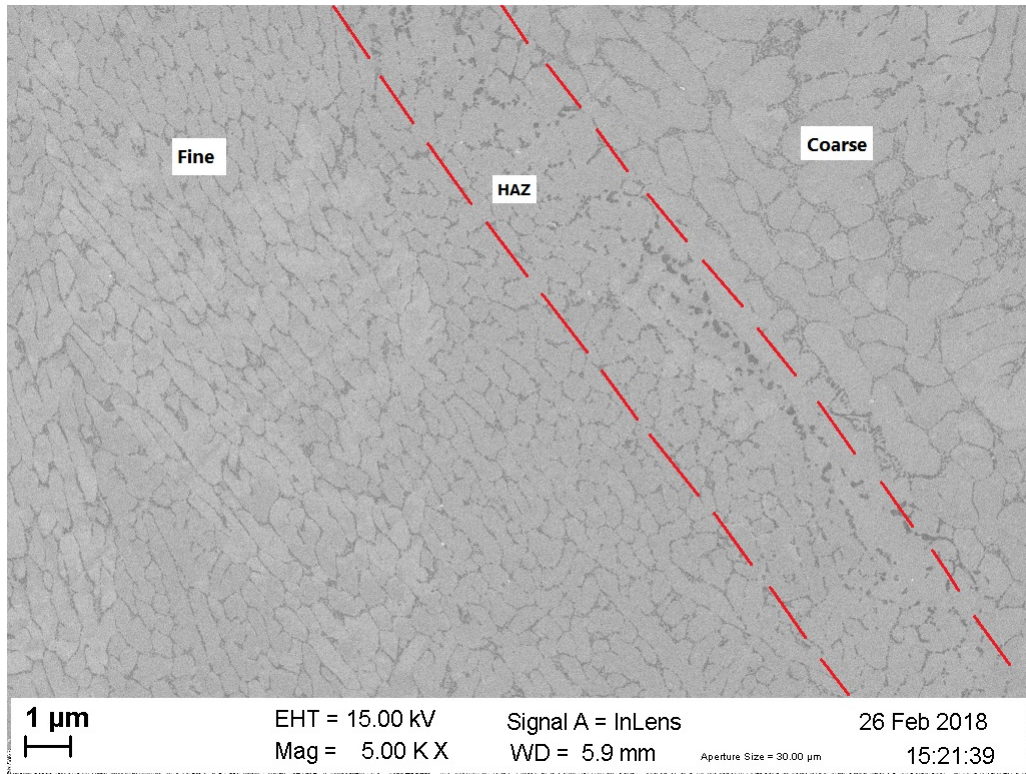


FIGURE 4.11: Microstructure of an as-built sample with the 3 different zones visible, indicating the edge of the melting pool.

Damage and fractography

The fracture surfaces of ruptured tensile specimens were directly observed via SEM, as shown in Fig. 4.12. Some "step-like" structures are present near the edges. They are shown on figure 4.13. Their width is ranging from 70 to 110 μm , which is similar to the hatch space of the SLM process.

Taking a closer look reveals on Fig. 4.14 the presence of dimples on an important fraction of the surface. Their size seems to vary mainly between 0.3 and 0.7 μm . But smoother areas are also visible on the surface (see Fig. 4.15). The presence of unmelted powder particles indicates that the area has known a lack of fusion. It causes bad cohesion between the consecutive layers and represents an important defect, able to initiate premature failure.

Microstructure damage after fracture was also observed via SEM. An example is available in figure 4.16. The cells are strongly oriented in the loading direction. Their average size in this direction is 1.2 μm , while it is only 0.6 μm in the perpendicular direction.

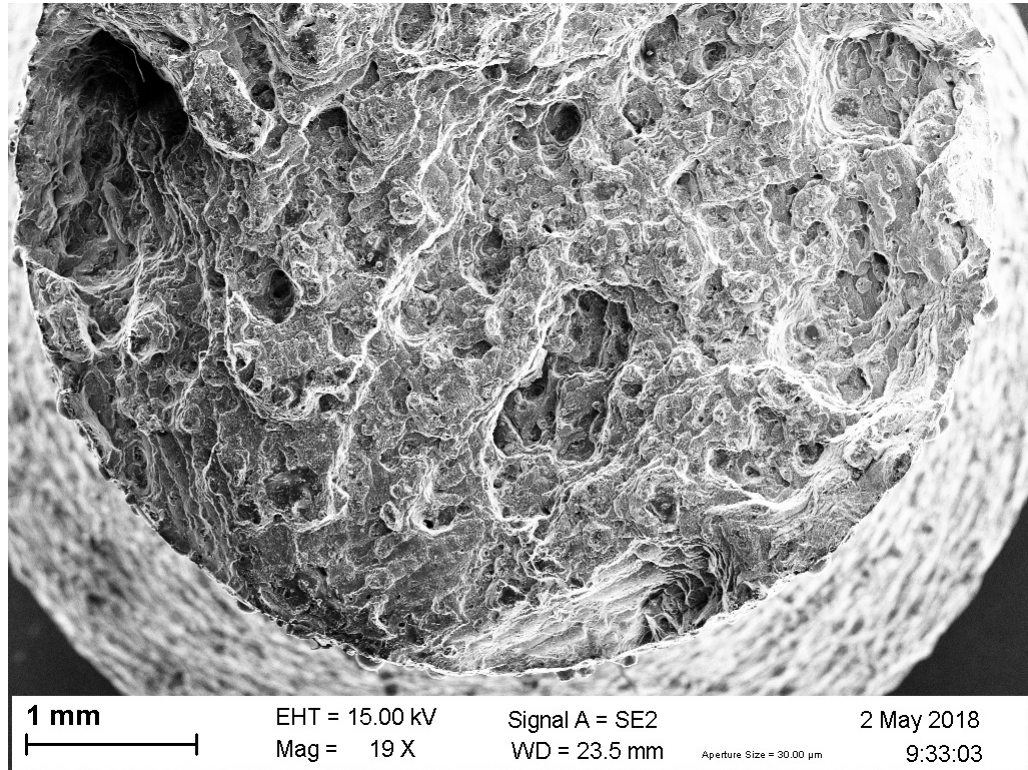


FIGURE 4.12: Fractograph of an as-built tensile sample.

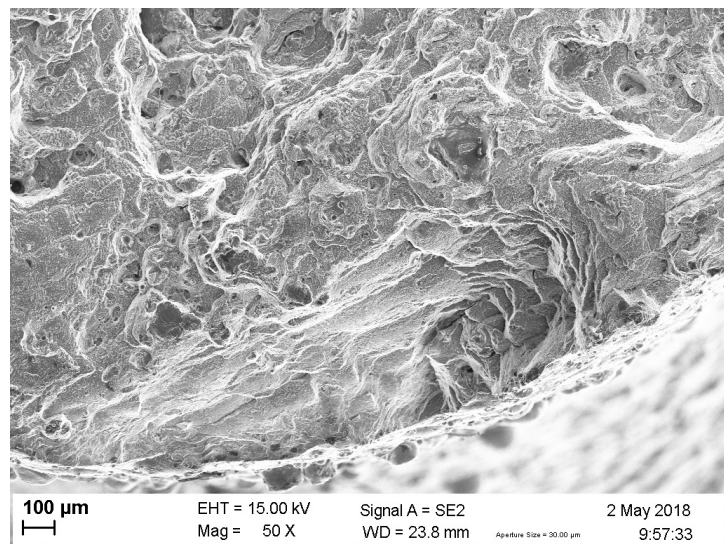


FIGURE 4.13: "Step-like" structure appearing on the edge of the as-built tensile sample.

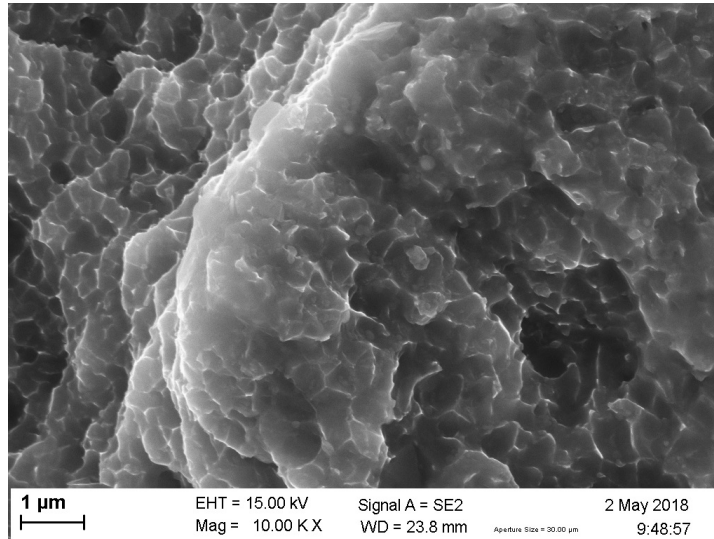


FIGURE 4.14: Close-up shot on the ductile dimples of the as-built fracture surface.

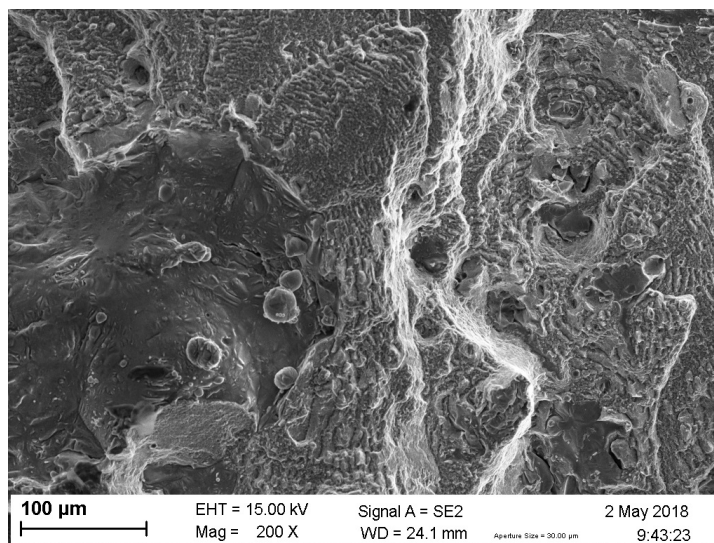


FIGURE 4.15: View of the smooth fracture surface (on the left). A couple unmelted powder particles are visible.

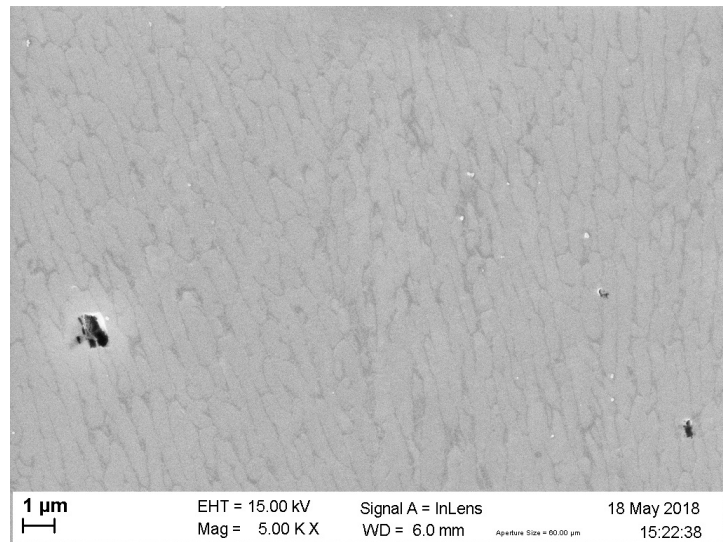


FIGURE 4.16: [Microstructure damage after rupture. The picture is taken roughly 40 μm below the fracture surface. The loading direction is vertical.

4.4 In-depth characterisation of the heat-treated samples

4.4.1 Density

The density of most of the heat treated cubes of dimensions $5 \times 5 \times 5$ [mm^3] was measured through RODIA (see table 4.15). The 95% CI are also indicated.

Temperature [°C]	Holding time [min]	ρ_{rel} [%]
150	120	99.83 ± 0.02
200	120	99.82 ± 0.04
225	120	99.88 ± 0.01
250	120	99.77 ± 0.04
300	5	99.85 ± 0.02
300	120	99.77 ± 0.04

TABLE 4.15: RODIA relative density results for the heat treated cubes

All samples came from the same batch (X200-180220) except for TT225-2 one which originated from batch X200-180319. The samples from the latter had significantly better properties than the other batches'. This particular specimen should thus not be compared to the others. The other samples treated during two hours show a slight decrease of ρ_{rel} as a function of the temperature. The relative density measured for TT300-5m, that was heated for a short duration, is superior to the other's. Nevertheless, caution should be exercised here since the measured differences are small (inferior to a tenth of percent).

4.4.2 Hardness

Heat-treated samples were subjected to hardness tests identical to those performed on as-built cubes. Results are displayed in figure 4.17.

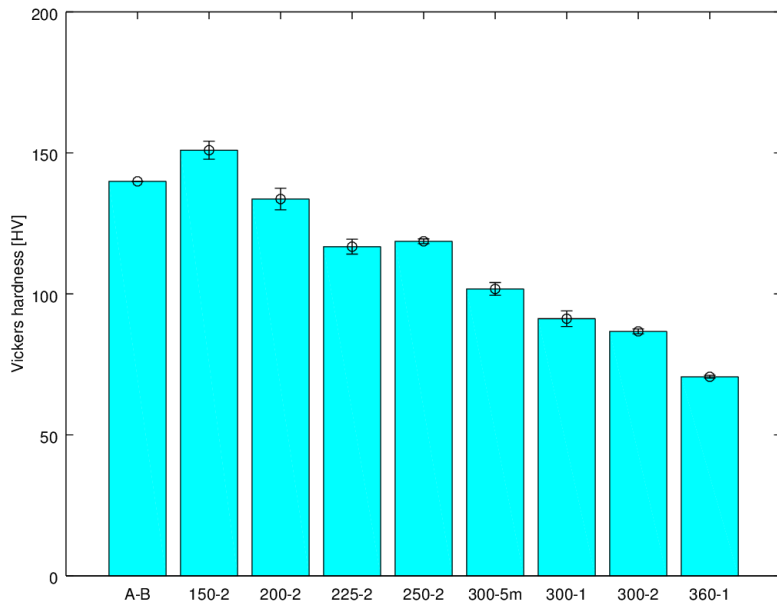


FIGURE 4.17: Comparison of the heat-treated samples hardness with the as-built.

4.4.3 Mechanical properties

Tensile tests were made on heat treated specimens. All samples had undergone a HT during 2h, at either 150°C, 200°C, 250 °C or 300 °C. Three samples were tested for each HT except for the one at 250 °C (only two samples). One specimen heated at 150°C was manufactured with no contour scanning strategy. The results are gathered in C. Typical curves for each heat treatment are displayed in figure 4.18. The average tensile properties for each HT are shown in table 4.16. All samples heated at 250°C and 300°C went through necking in the sense of Considère criterion. Their $\epsilon_{f,true}$ was computed thanks to a profile projector.

HT	E [GPa]	σ_y [MPa]	σ_u [MPa]	$\epsilon_{f,eng} [\%]$	$\epsilon_{f,true} [\%]$
150°C (2h)	68.4 ± 1.9	288.2 ± 1.4	441.7 ± 5.5	3.1 ± 0.4	-
200°C (2h)	72.1 ± 0.4	245.4 ± 0.6	382.0 ± 11.4	2.6 ± 0.2	-
250°C (2h)	70.6 ± 1.0	235.1 ± 7.4	340.9 ± 12.2	8.8 ± 0.2	16.5 ± 0.1
300°C (2h)	68.9 ± 0.6	170.7 ± 1.7	252.9 ± 10.4	13.6 ± 0.5	29.7 ± 0.1

TABLE 4.16: Average tensile mechanical properties of the heat-treated specimens from batch X200-180417

The heat treatment at 150° increased notably σ_u compared to the as-built values. However, the heating at 200° caused virtually no change of ultimate tensile strength. None of these heat treatment caused any significant change of fracture strain. For HT at 250° and 300°, the material softened significantly (with necking appearance); the

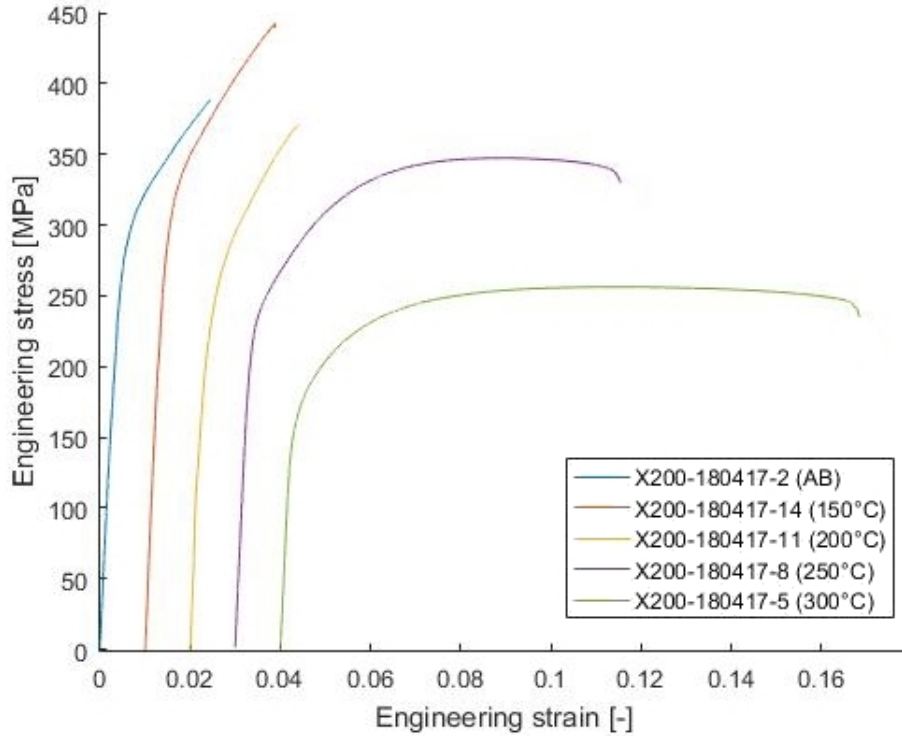


FIGURE 4.18: Engineering stress-strain curves of heat treated tensile specimens of batch X200-180417.

higher the heating temperature, the bigger the ductility increased and the strength decreased. The Young's modulus measured for heat treated samples was significantly bigger in average 69.9 [GPa] compared to 64.9 [GPa].

The average σ_{true} - ϵ_{true} data was also displayed in a graphical form for better insight. The true stress and strain were approximated by the engineering ones for samples with no necking. A fit was made with the average properties in a Ramberg-Osgood hardening law:

$$\epsilon_{true} = \frac{\sigma_{true}}{E_a} + 0.002 \left(\frac{\sigma_{true}}{\sigma_{y,a}} \right)^{\left(\frac{1}{n_a} \right)}$$

where $n_a \simeq \epsilon_{f,true,a}$ is the strain hardening coefficient. The subscript "a" means that the average values are used. This was done with an online calculator [42].

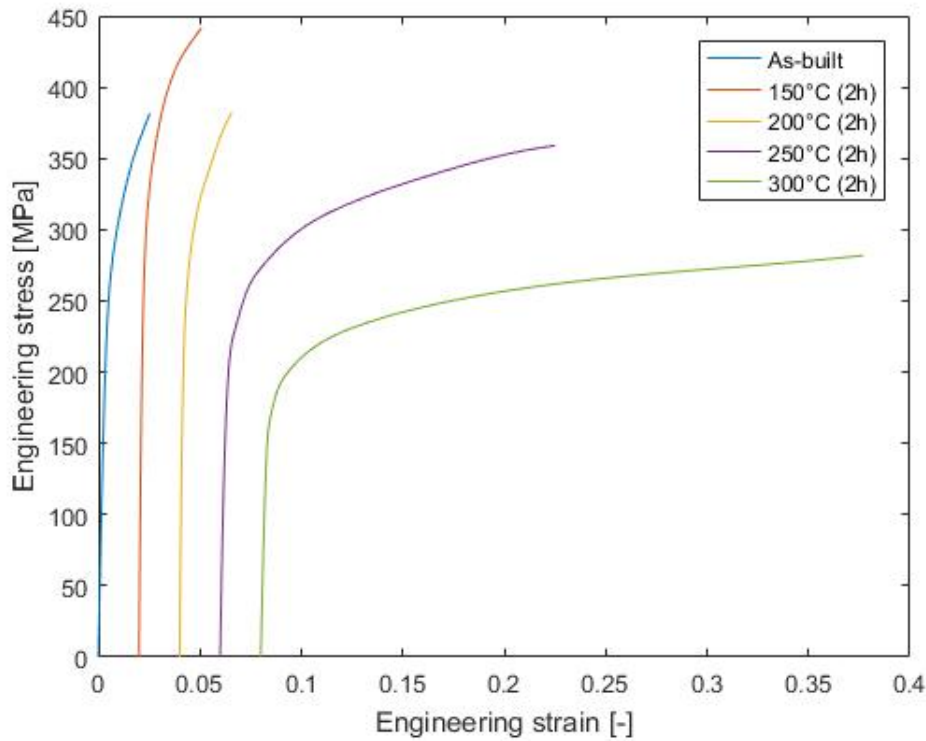


FIGURE 4.19: Average stress-strain curves of the tensile specimens of batch X200-180417.

4.4.4 Microstructure

As discussed in the section 2.6, heat treatments can modify the fine microstructure of SLM parts.

Treatment at 250°C gives an intermediate result, as shown in Fig. 4.21. Globularization begins to take place but most of the cellular structure remains visible. Cell size is for the most part comprised between 0.5 and 0.9 [μm], with a mean size around 0.7 [μm]. As a comparison with other samples treated at higher temperature, the particle size was calculated with ImageJ. The result was a mean particle size of 0.29 [μm].

Microstructure after heat treatment at 300°C for 2 distinct holding times are available in Fig. 4.22 and 4.23. The mean particle size for 1 hour and 2 hours holding time are respectively 0.22 and 0.27 [μm]. We know that the particles tend to agglomerate along the cell boundaries, which leaves the center free from most of the Si phase. Intergranular distance of two particles on the same boundary can be very small, while distances across the cell represent a better comparison point to the cell size of non-globularized samples. A quick measurement of those specific intergranular distances gives value comprised between 0.4 and 0.8 [μm].

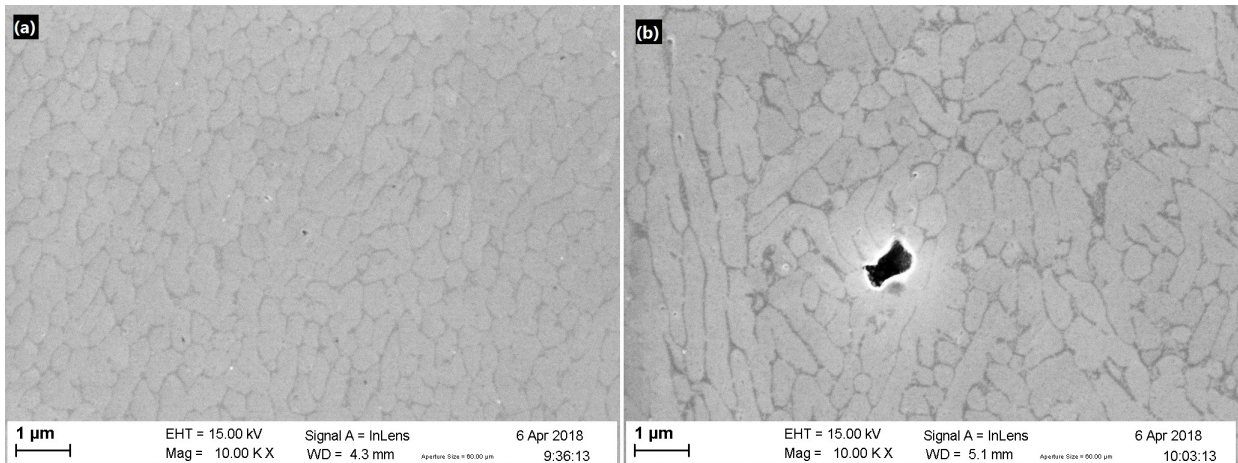


FIGURE 4.20: Microstructure of the sample heat-treated at (a) 150°C for 2h and (b) 200°C for 2h.

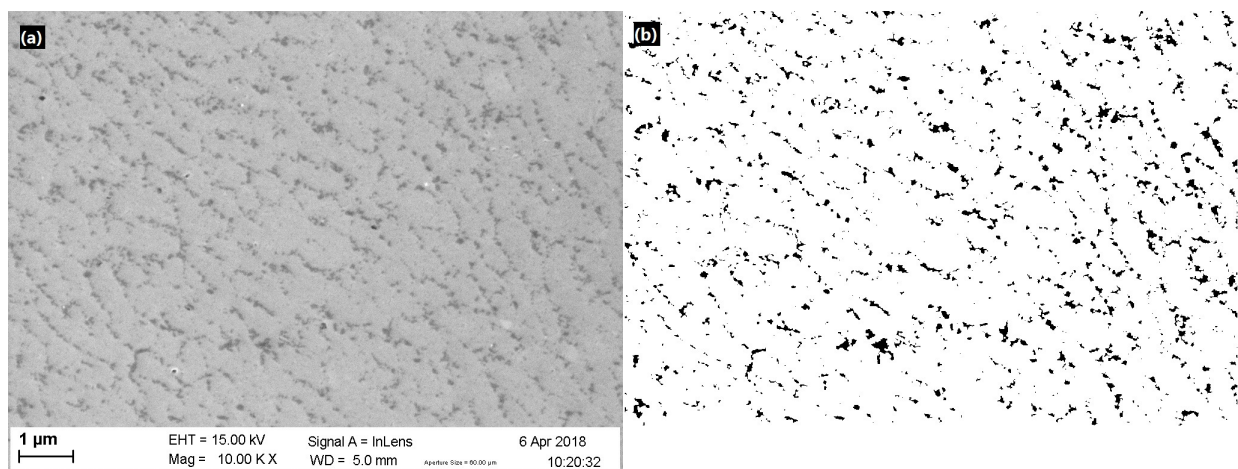


FIGURE 4.21: (a) Microstructure of the sample heat-treated at 250°C for 2h and (b) Isolation of the Si particles via the ImageJ software.

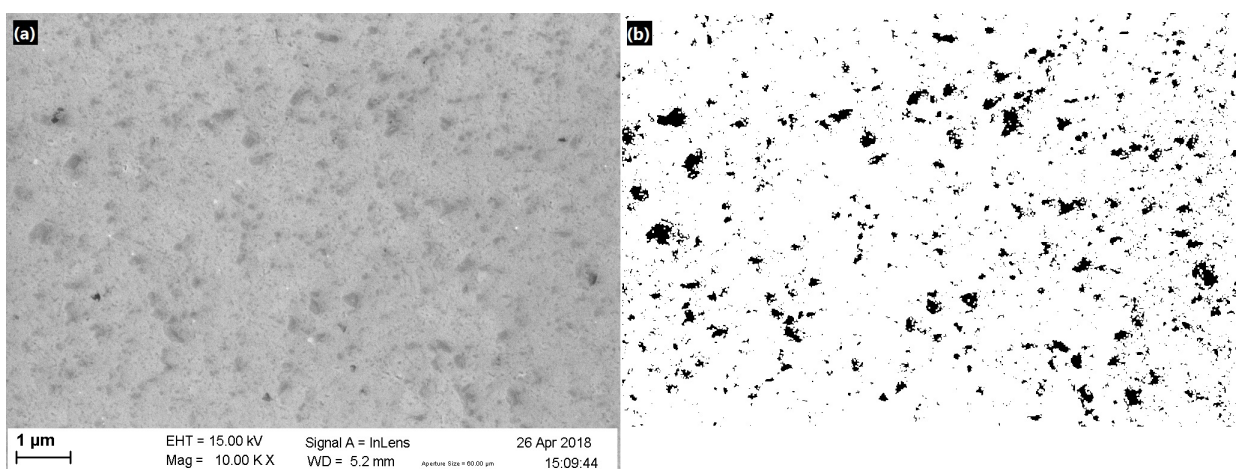


FIGURE 4.22: (a) Microstructure of the sample heat-treated at 300°C for 1h and (b) Isolation of the Si particles via the ImageJ software.

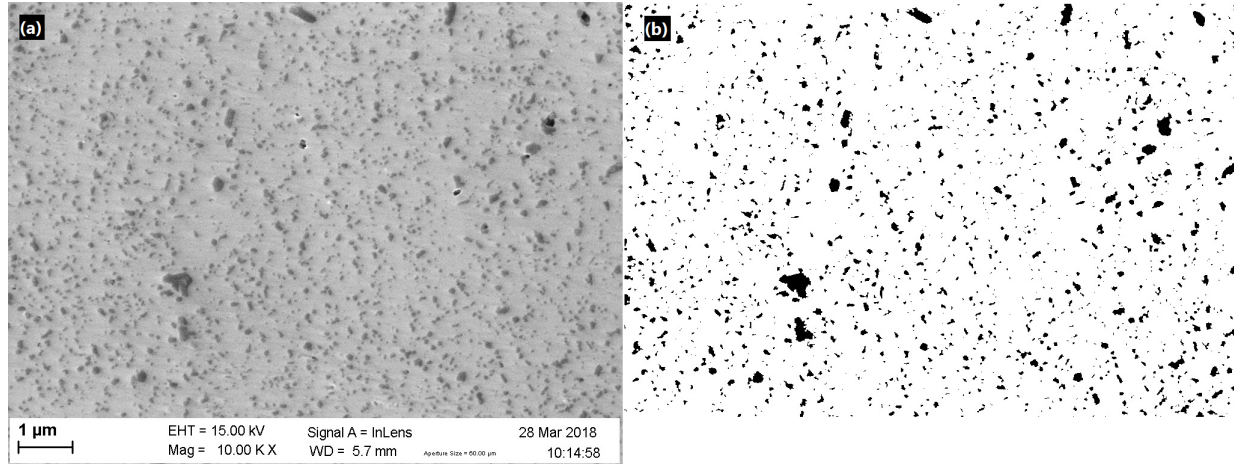


FIGURE 4.23: (a) Microstructure of the sample heat-treated at 300°C for 2h and (b) Isolation of the Si particles via the ImageJ software.

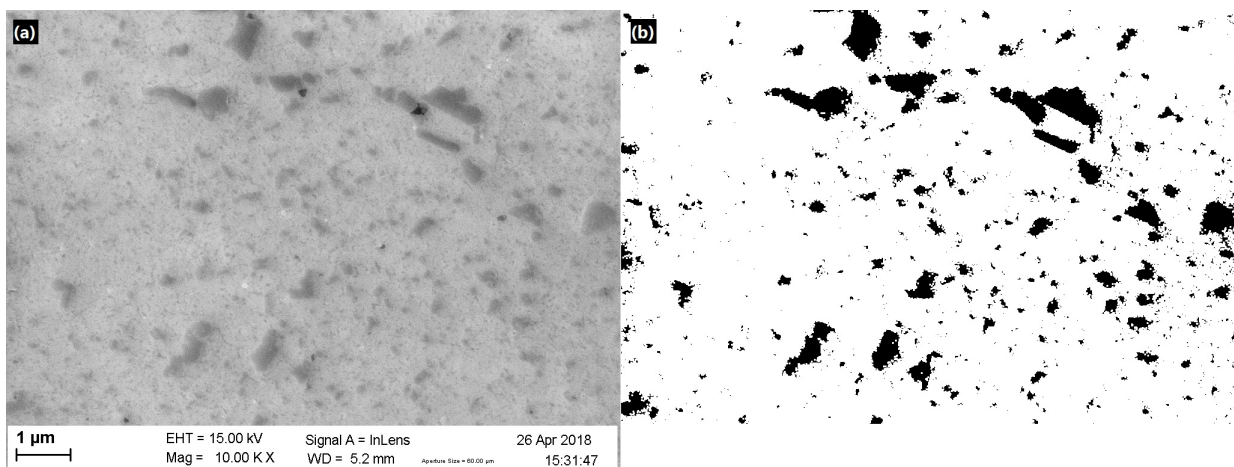


FIGURE 4.24: (a) Microstructure of the sample heat-treated at 360°C for 1h and (b) Isolation of the Si particles via the ImageJ software.

Damage and fractography

Fracture surfaces of heat-treated samples keep several common characteristics with as-built surfaces. The parallel lines delimiting scan tracks remain visible after every annealing, up to 300°C holding for 2h, as shown in Fig. 4.25. The same observation can be made for regions showing a lack a fusion, as displayed in Fig. 4.26.

Most of the surface is covered of dimples, visible on figure 4.27, with an average size of 0.7 [μm]. The dimples seem however to present a larger depth than in as-built samples, because ridges are more elongated. This could mean that these ridges can sustain higher plastic strain before failure.

As highlighted on figure 4.28, several porosities with a diameter below 10 [μm] appear on the fracture surface.

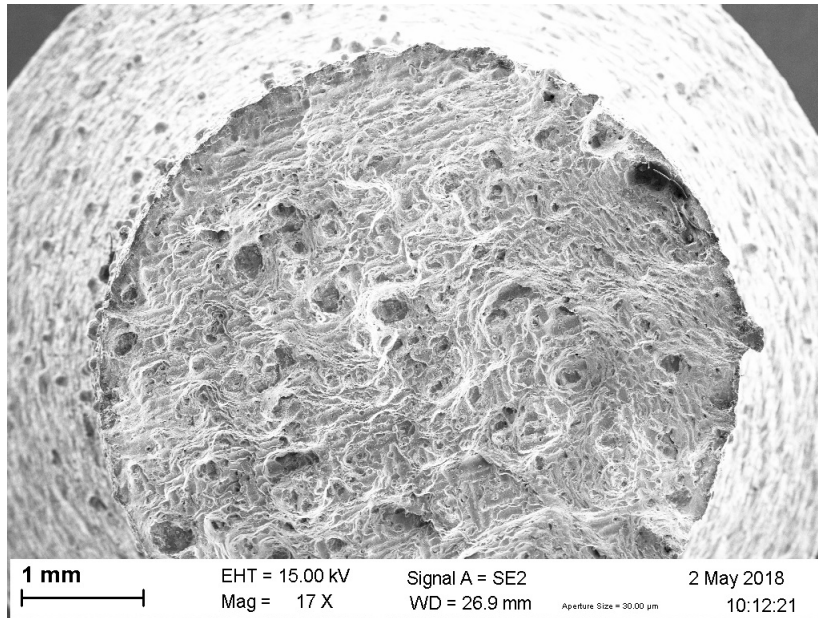


FIGURE 4.25: Fractograph of a 300°C-2h tensile sample.

The microstructure damage observable on Fig. 4.29 present voids inside the globular Si particles. These could indicate brittle fracture of the Si phase prior to complete failure of the part.

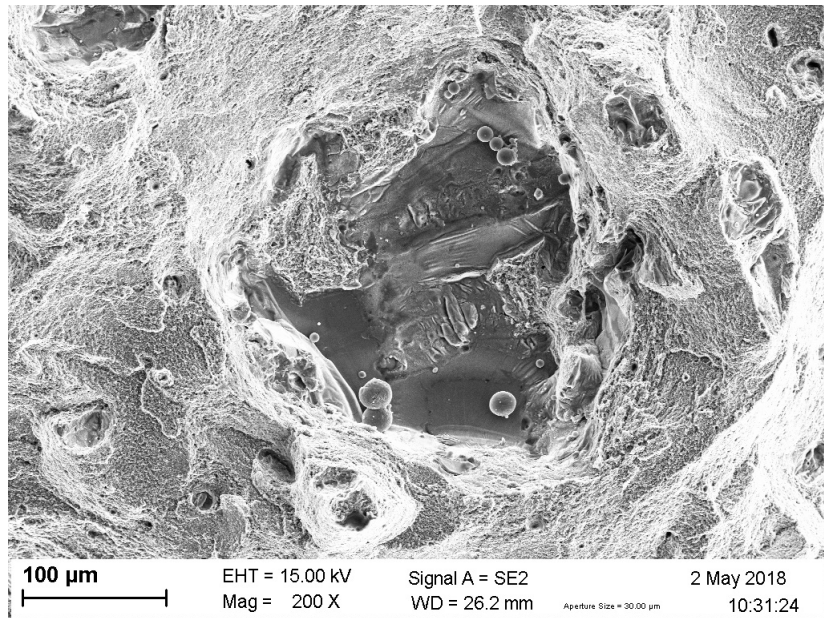


FIGURE 4.26: View of the smooth fracture surface of 300°C-2h sample. A couple unmelted powder particles are visible.

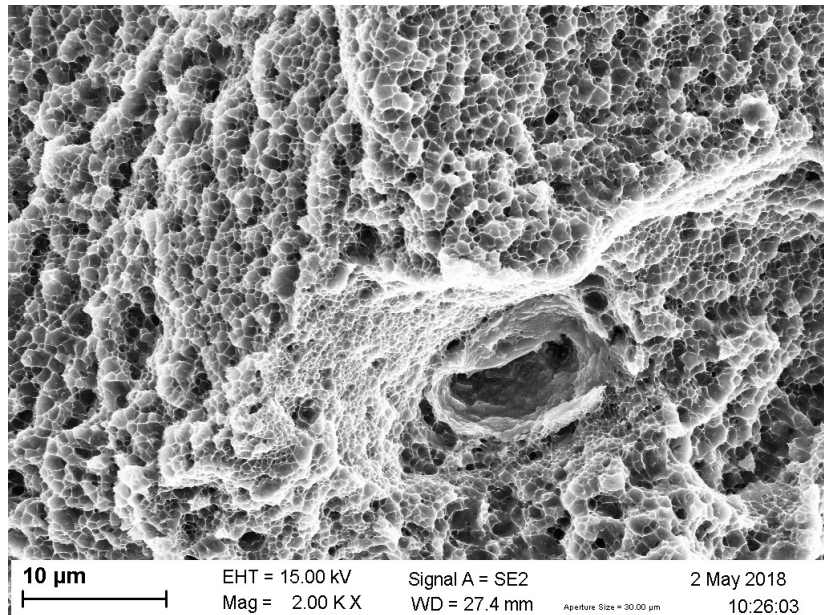


FIGURE 4.27: Close-up shot on the ductile dimples of the 300°C-2h sample fracture surface.

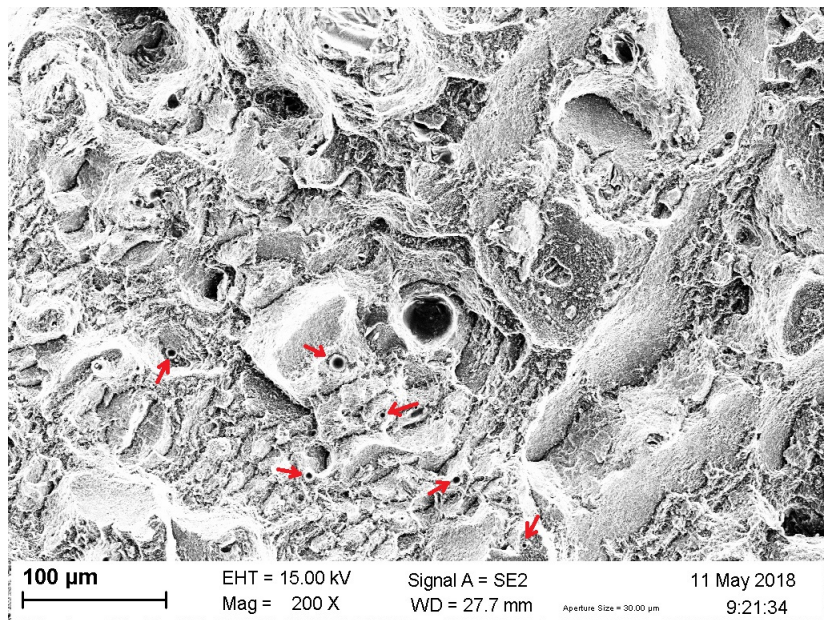


FIGURE 4.28: View of the smooth fracture surface of 300°C-2h sample. A couple unmelted powder particles are visible.

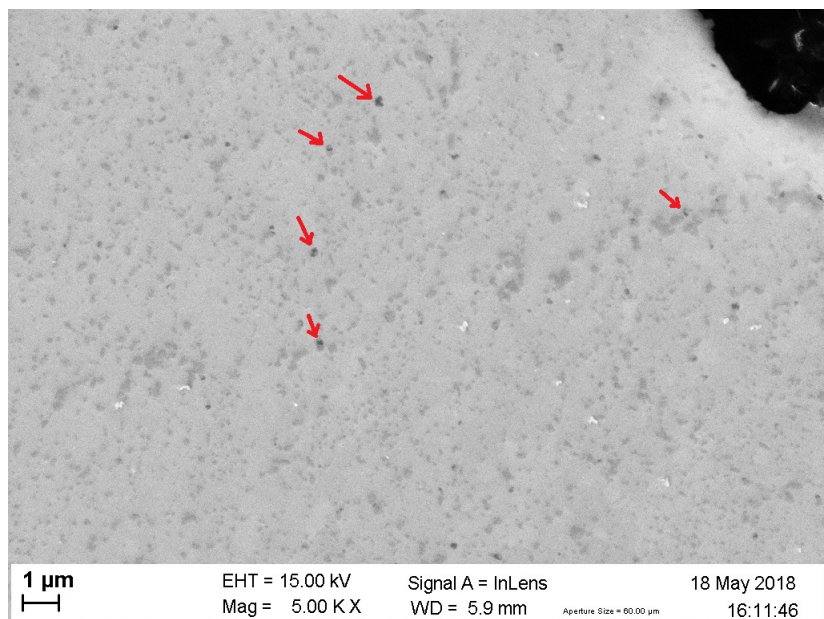


FIGURE 4.29: Microstructure damage after rupture of a 300°C-2h sample. The loading direction is vertical.

4.5 Residual stresses

X-ray diffraction of an as-built sample cut in half gave the results displayed on figure 4.30. A zoom on the main aluminium peak (around 38.4°) [52], including comparison with the various heat-treated samples, is available in figure 4.31. The value of full width at half-maximum (FWHM) for all 5 samples is available in Table 4.17.

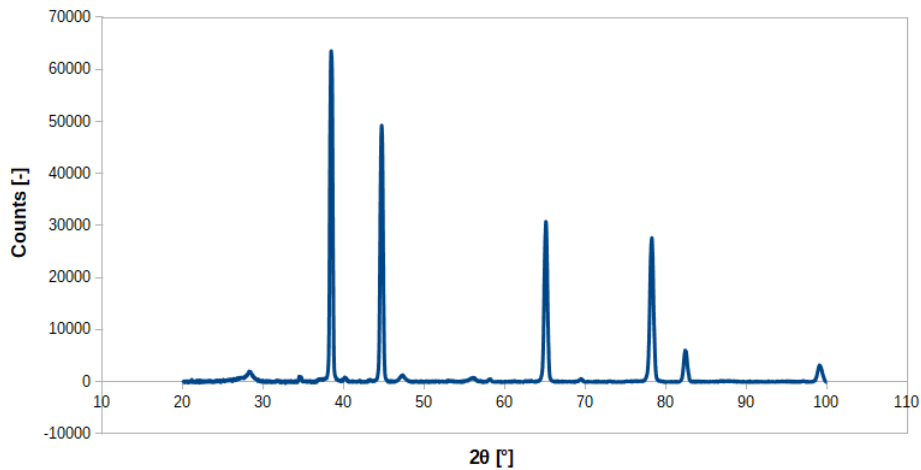


FIGURE 4.30: X-Ray diffractogram of a X200-180109 as-built sample.

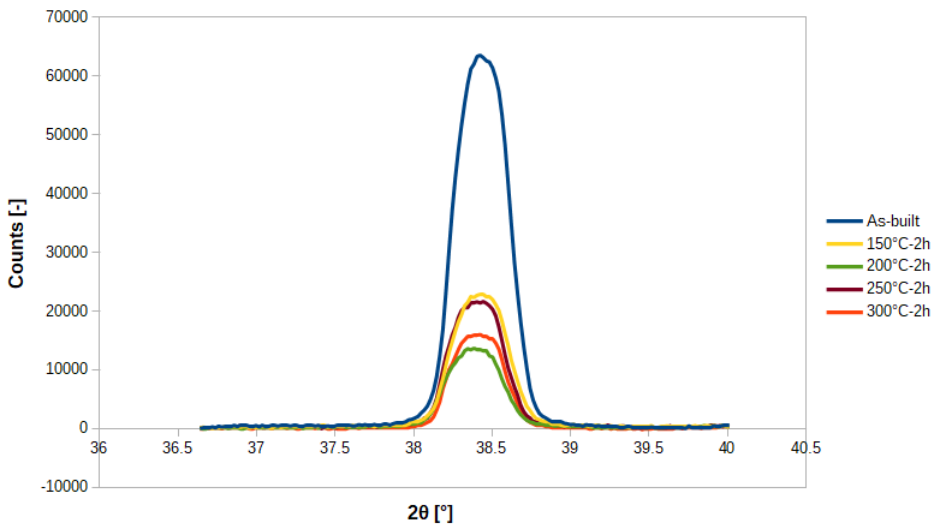


FIGURE 4.31: Close-up view on the highest Al peak, for the 5 different samples.

Hole-drilling method gives more quantitative results. When we assume that the residual stresses are uniform along the xy planes, at least at the scale of the hole, we obtain that the as-built sample presents a maximal and minimal principal stress respectively of 10 and 1 MPa. For the sample heat-treated at 300°C for 2h, those values are respectively 43 and 23 MPa. When the assumption that stress varies depending

Sample	As-built	150°-2h	200°-2h	250°-2h	300°-2h
FWHM [°]	0.402	0.410	0.408	0.402	0.400

TABLE 4.17: Average tensile mechanical properties of the as-built specimens from batch X200-180417

on the depth, the two chosen calculation methods offer different results, available in figure 4.32.

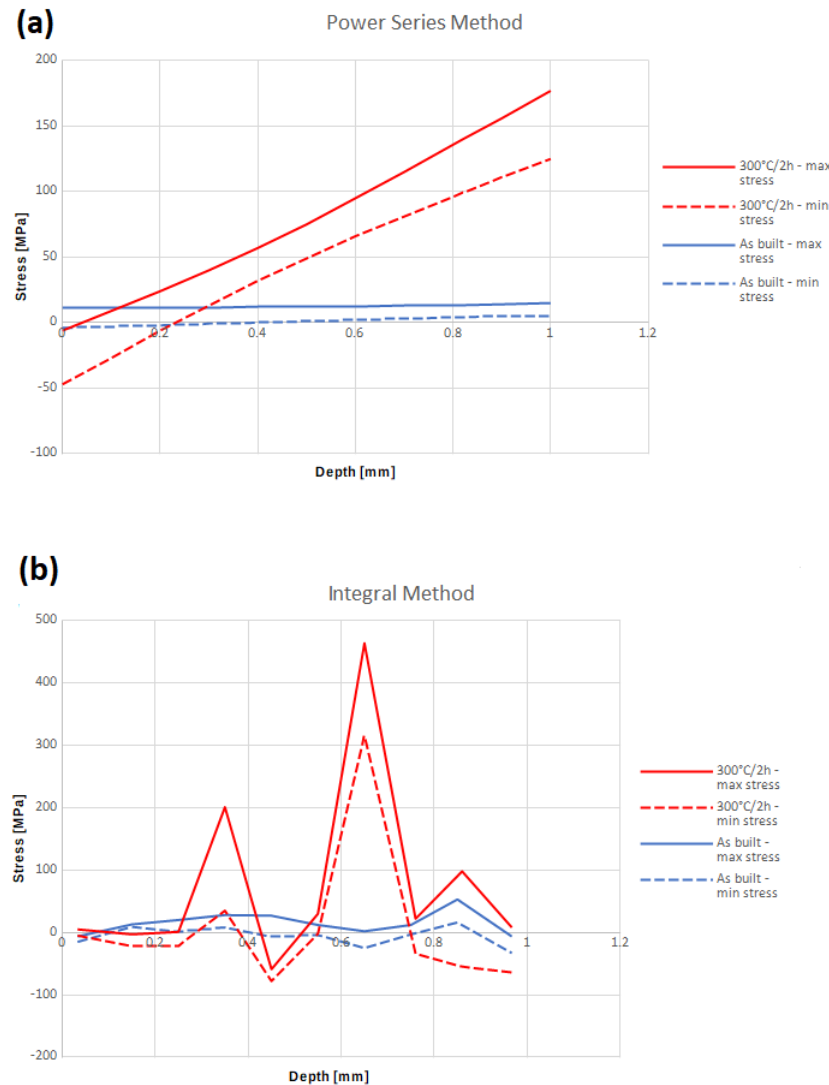


FIGURE 4.32: Magnitude of principal residual stresses along depth in both the 300°C-2h and the as-built sample, calculated with (a) the power series method, (b) the integral method.

Chapter 5

Discussion

5.1 Powder ageing

5.1.1 Grain size and distribution

Two trends were identified in section 4.1.1: there was a clear diminution of the average particle size D_a and a narrowing of the distribution as functions of the number or recycling iterations. Only one sampling did not concur with these observations. This can be easily explained: the powder in question was sampled just after fresh powder was added to the recycled one. Its size distribution was thus shifted back towards a fresher distribution.

Particle sizes going up to $\simeq 134 [\mu m]$ were measured in the powder samples even though they were sieved with a $75 [\mu m]$ mesh size. The most reasonable justification is that particles agglomeration took place between the siftings and the sizes measurements. Ultrasonic treatments gave the opportunity to confirm that a non-negligible part of the AlSi10Mg powder indeed agglomerated. The maximal measured particle size after exposure to ultrasounds was $\simeq 84 [\mu m]$. This is rather close to the sieving mesh size but still bigger. The gap between the two could be due to lack of resolution or to residual aggregates.

The agglomeration phenomena could explain the diminution of the average particle size with the recycling iterations, according to Maamoud et al. (2018) [23]: the large particles that agglomerated since the last sieving could not go through the mesh. Only smaller particles were thus recycled, lowering the average size. Another cause could be the projection of very fine spatters out of the melt pool during the process. These spatters could fall in the unmelted powder and be recycled with it. Unfortunately, no source could be found literature to support or refute this hypothesis.

It seems reasonable to assume that the agglomerates could have led to the emergence of defects in the parts due to powder bed inhomogeneity. This could, at least partly, explain the scatter of relative densities for samples from a same batch.

5.1.2 Composition

ICP spectrometry was used in order to estimate the impact of repeated recycling on the evolution of the chemical elements mass fractions. A few observations were made. The prior addition of fresh powder of February sample increased the mass fractions of iron, magnesium, and potentially silicon. It seems that there is a systematic diminution of the alloying elements with the reuse of the powder. Unfortunately,

this cannot be attested due to the large error bars.

The change of composition induced by SLM was also investigated for two samples. It was concluded that approximately 4% of the magnesium was lost during the process. The preferential loss of magnesium for a heated aluminium-based alloy is well known [22]. It is due to the lower vapour pressure of the element.

5.2 Density measures assessments

5.2.1 Relative optical density image analysis

The estimation of the relative density through RODIA can be imprecise on many aspects. First, the distribution of porosities is inhomogeneous on the analysed surface. Multiple pictures must thus be taken systematically and arbitrarily for each specimen to constitute a representative sample.

Second, the quality of the images has a critical role. The isolation of the porosities during the thresholding requires a substantial difference of pixel intensity between the holes and the material. Since some porosities and some zones of the material can appear respectively brighter or darker than was expected, there are risks that one isolates spots and/or not actual porosities. Additionally, the thresholding is manual and thus prone to slight human errors.

Most importantly, the finite resolution of the camera implies that the smallest porosities are not visible on the pictures. One can expect the density measurement through RODIA to be a biased method, due to the discretisation in pixels among other things. Results for pictures with different magnifications were compared to quantify these effects. For this purpose, a picture was taken under 5x magnification and two under 10x magnification. The former was delimited to match the visible zones on the latter (see figure 5.1). The same two zones - named A and B - were thus analysed for different levels of resolution.

The comparison of figures 5.3 (b) and (d) shows that much more small porosities are isolated if the resolution is refined. This is confirmed by the bar charts on figure 5.2. The threshold of porosity area for detection in the case of 5x magnification is $0.5625 \text{ } [\mu\text{m}^2]$ whereas it is $0.14 \text{ } [\mu\text{m}^2]$ for 10x magnification. This area corresponds to a pixel in each case. It is also worth noting that there is an overall tendency to overestimate the areas at lower resolution, which counterbalances slightly the low number of detected porosities.

The RODIA results for zones A and B are outlined in table 5.1. It was observed that pictures with lower resolution have the tendency to lead to the overestimation of the relative density. The order of magnitude of the difference is of few hundredths of percent. The method is thus presumably positively biased. However, the observed effect is minor: this is probably due to the fact that the undetected porosities are the smallest, which influence the less the calculated density value.

Taking pictures at refined magnification could be considered to refine the precision of the method. This would, however, require to increase the number of analysed

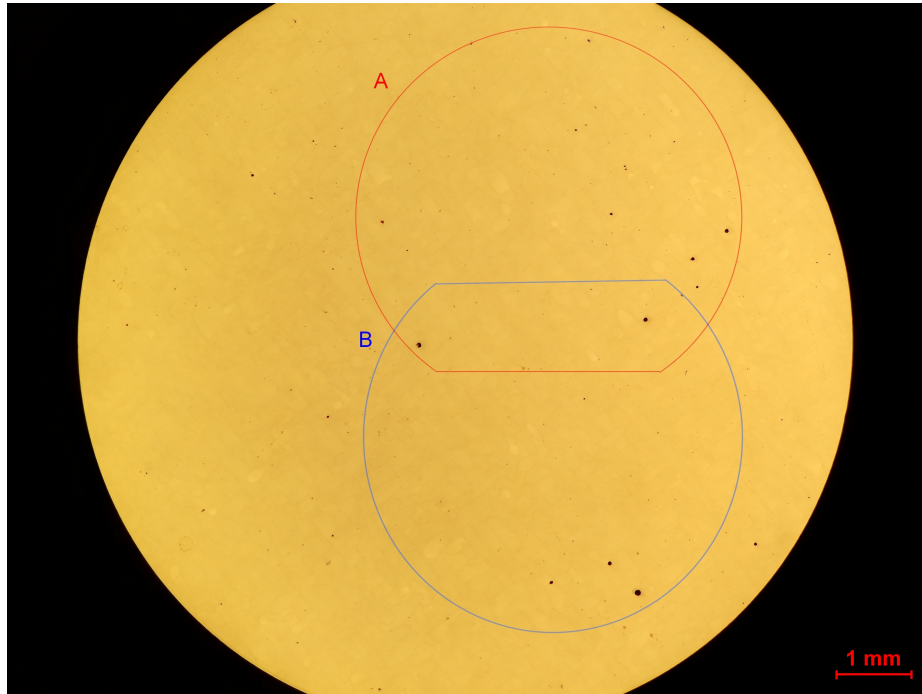


FIGURE 5.1: 5x magnification picture of specimen X200-180319-cub1 and delimitation of the zones A and B

Zone	Magnification	Measured relative density [%]
A	5x	99.87
A	10x	99.84
B	5x	99.86
B	10x	99.85

TABLE 5.1: RODIA results for zones A and B of specimen X200-180317 with 5x and 10x magnification

pictures to generate a sample size as representative. A picture with doubled magnification covers indeed four times less surface. The number of analyses should thus be quadrupled to take as much information into account.

RODIA method required to make the assumption that the volumetric porosity fraction is equal the surface one. The dependability of this affirmation will now be discussed. Let us consider a cubic cell of side length D containing a spheric porosity of diameter D in its center (see figure 5.4). The volumetric porosity fraction f_v is:

$$f_v = \frac{\frac{\pi D^3}{6}}{D^3} = \frac{\pi}{6}$$

However, the surface porosity fraction depends on the observed pore diameter D_{obs} which varies with the z coordinate of the surface plane crossing it: $\frac{D_{obs}(z)}{2} = \sqrt{(\frac{D}{2})^2 - z^2}$. If we assume that there is a statistically significant number of pores of similar size, one can make the hypothesis that - in average - the observed diameter is the mean diameter D_{mean} :

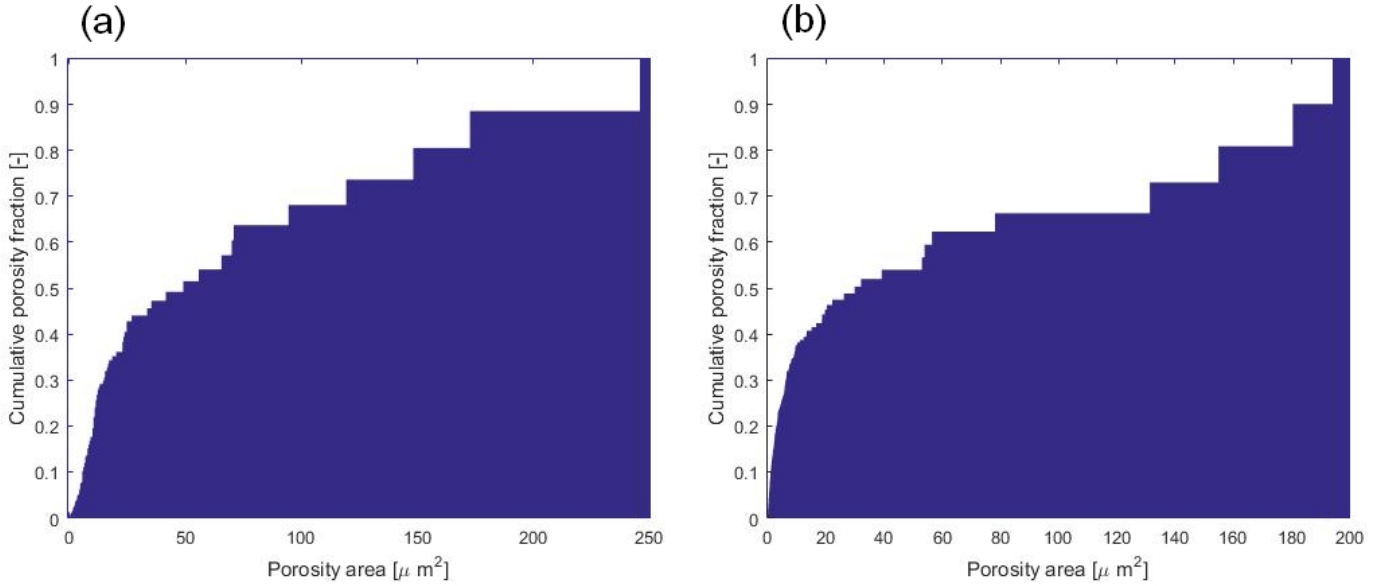


FIGURE 5.2: Cumulative porosity fraction bar chart as function of the porosity area from picture of specimen X200-180319 on zone A under
 (a) 5x magnification (b) 10x magnification

$$\frac{D_{mean}}{2} = \frac{\int_{-\frac{D}{2}}^{\frac{D}{2}} D_{obs}(z) dz}{D} = \frac{\pi D}{8}$$

This hypothesis is quite coherent for small pores but not for the largest: in most cases, a very small number of pores is significantly bigger than the others. If we still assume it to be true, the surface porosity fraction f_s can be computed as follows:

$$f_s = \frac{\frac{\pi D_{mean}^2}{4}}{D^2} = \frac{\pi^3}{16 \cdot 4} \simeq 0.9253 f_v$$

It can thus be concluded that the method to measure the relative density intrinsically has a slightly built-in positive bias. The greater the porosity is, the bigger the bias. In the working range of ρ_{rel} of this work, they can go from 0.01 to 0.03 [%]. Combining this with the bias induced by the measures imperfections, one can conclude that RODIA should be used as a mean to estimate an upper limit for the relative densities.

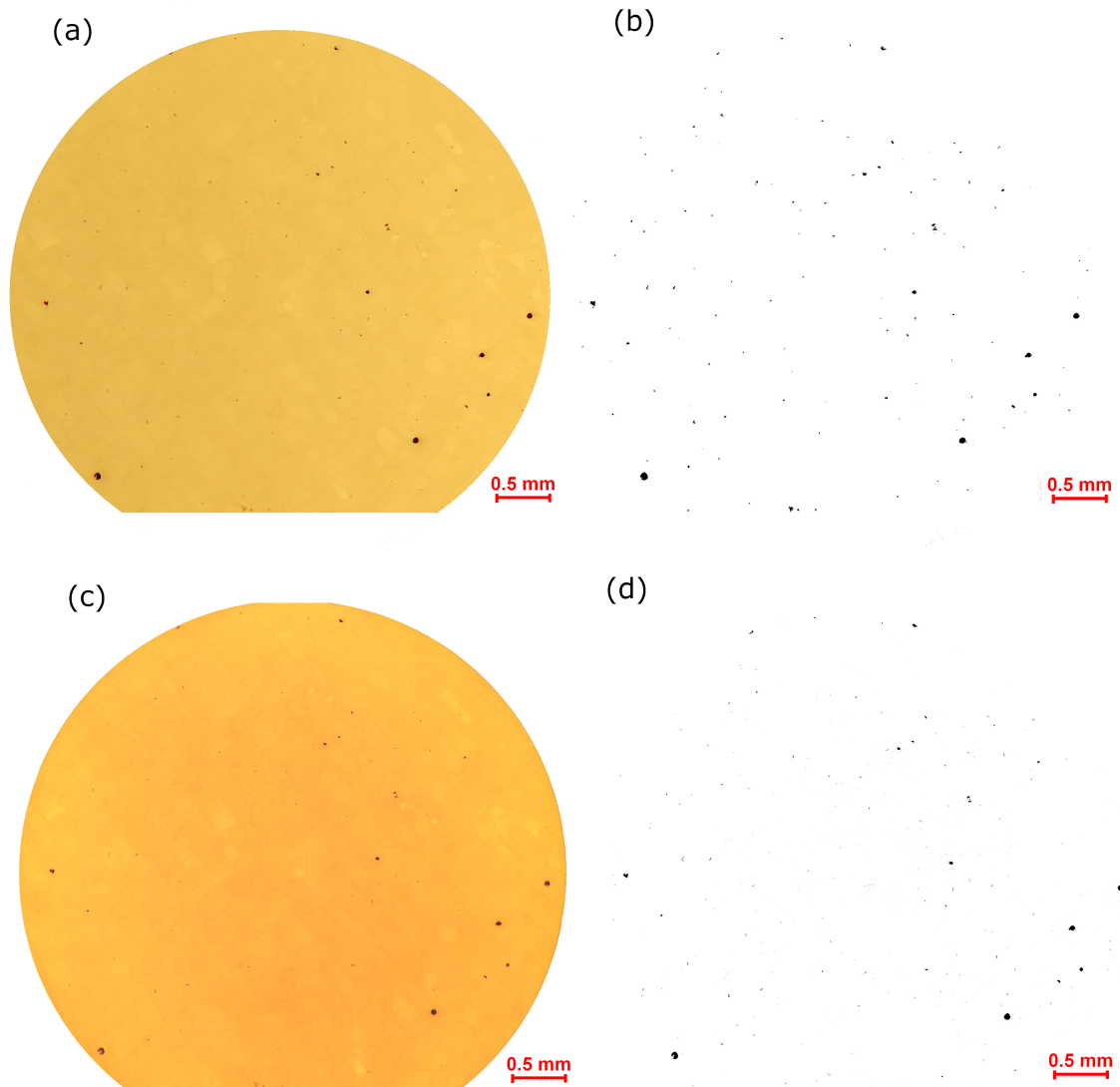


FIGURE 5.3: Zone A of specimen X200-180319-cub1: (a) Delimitation from original picture under 5x magnification (b) Porosities isolation from 5x magnification picture (c) Original picture under 10x magnification (d) Porosities isolation of 10x magnification picture

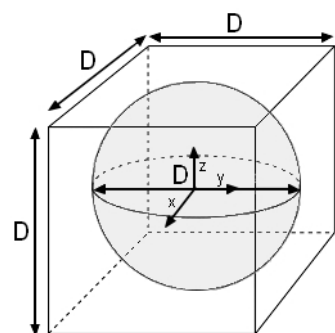


FIGURE 5.4: Schematic of a spheric porosity of diameter D in a cubic cell of size length D

5.2.2 Measures comparison

Some samples' densities were also measured through hydrostatic weighing (both with and without preliminary polishing). Multiple techniques were performed on the same few specimens in order to draw a comparison of the results and reach a deeper understanding of the methods reliability. The results are gathered on figures 5.5 and 5.6.

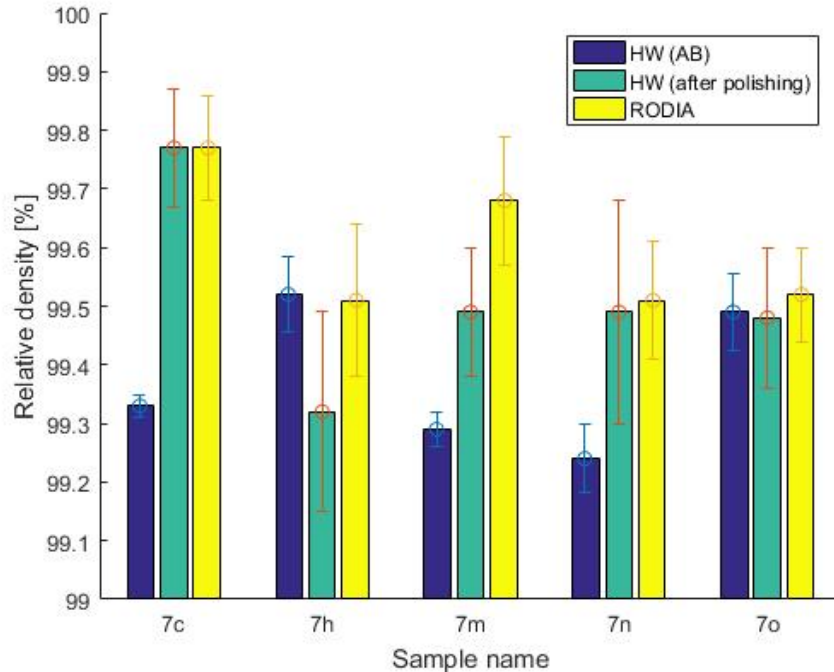


FIGURE 5.5: Bar charts of the density measurements with the HW (AB and after polishing) and RODIA methods for samples of batch X200-180109

As-built hydro measurements on figure 5.5 demonstrated high variability relatively to the other measures. Over the five tested samples, two exhibited similar relative densities for all techniques. However, three had $\rho_{a,rel}$ significantly below the values obtained with the other methods. In particular, the gap for sample "7c" was 0.44 [%]. The fact that the CI do not intersect with the others' suggest that AB HW method was negatively biased in those cases. The most plausible explanation is that air was trapped in the surface roughness, which distorted the results (by overestimating the closed porosities volume). This would not be surprising as SLM produced parts usually have bad surface finish.

The two other methods were more promising. Relative densities obtained with RODIA method are generally close to the ones of HW after polishing (see figures 5.5 and 5.6). In average, the absolute difference between the two is 0.16 [%] (0.24 [%] at most). When the difference is greater than 0.02 [%], the RODIA method always give greater density values. In addition, the CI do not always intersect. This can be attributed to the RODIA positive bias, and potentially to a negative bias for HW -

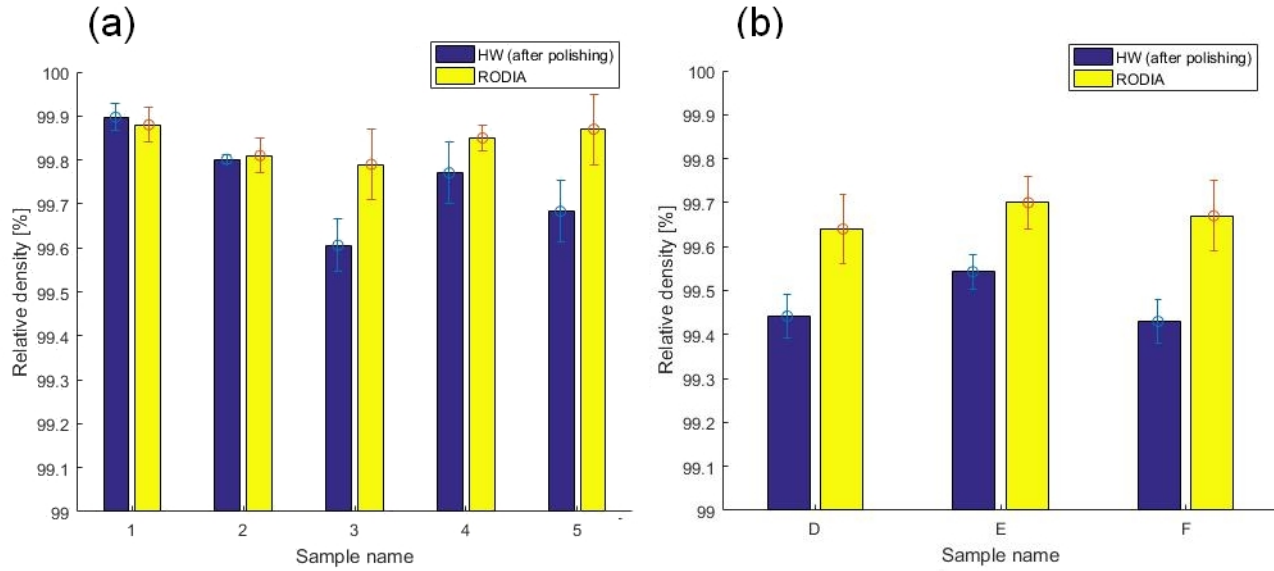


FIGURE 5.6: Bar charts of the density measurements with the HW (after polishing) and RODIA methods for samples of (a) batch X200-180319 (b) batch X200-180417

that would still not be fully erased through polishing. Ultimately, given the opposite bias and the proximity of the relative density values for both methods, one could consider the two to be bounds between which lies the actual ρ_{rel} .

5.3 Density and hardness study

5.3.1 Parameters optimisation

Optimisations of the relative density and hardness were both achieved with the parameters set ($P = 0.75P_{max} = 205[W]$, $v_s = 1200[\frac{mm}{s}]$). This pair of parameters lie in the process window suggested in section 2.3. Kempen et al. found optimal parameters values (maximising density) that are not far to the ones of this work (see table 5.2) [32]. The energy density was however significantly bigger in this work, especially since the laser was more focused (which is not taken into account for the approximate computation). E_d is rather close to a value minimising porosity obtained by Read et al. ($65 [\frac{J}{mm^3}]$) [50]. Both cited sources used a chessboard scanning strategy, with islands size of around $5 \times 5 [mm^2]$.

Source	$h [\mu m]$	$t [\mu m]$	$\phi_{99\%} [\mu m]$	$P [W]$	$v_s [\frac{mm}{sec}]$	$E_d [\frac{J}{mm^3}]$
This work	100	30	75	205	1200	57
[32]	105	30	150	200	1400	45
[50]	75	30	150	200	1350	65

TABLE 5.2: Optimised manufacturing parameters comparison with literature sources

A relative density of 99.9 [%] was reached, which is superior to the best values found in the literature [17]. It is likely that all samples manufactured with the optimised parameters had $\rho_{rel} > 99.4\text{[%]}$ according to the measurements. Results depended on the powder age and recycling (4.2.2). It can be confirmed that the parameters chosen allowed for a right energy input and a correct melt pools overlapping.

The hardness was significantly bigger than what is typically expected - approximately 10 [HV] more (see section 2.4). This could indicate that the microstructure was finer than was typically obtained or that the material had a more pronounced work hardening ability. At first glance, nothing would justify this. A more credible justification is measurement-related: first, the obtained H_V value depends significantly on the load and on the test's time length. A study showed that the Vickers hardness of aluminium 17-ST alloy - which has a comparable H_v as AlSi10Mg - can range from 130.8 to 143.0 depending on the testing conditions, as shown in table 5.3 [9]. This alone could explain the high hardnesses measured in this work as the load and the time length were both small (respectively 10 [kg] and 10 [sec]).

In addition, the indenting machine used necessitates to take manual measurements. Given the high sensitivity of the hardness as a function of the lengths measured, the slightest error is greatly amplified. For example, a length error of 5 [μm], which is the achievable accuracy, induces an error of 4 [HV]. Although the repeated testing greatly improves the estimation reliability (see confidence intervals in section 4.2.1), a slight negative bias could induce a systematic overestimation of the hardness by a few [HV]. For these reasons, the hardness values obtained in this work should not be compared to the ones in literature. However, they still can be compared to each other as they were obtained through the same procedure.

Material	Load (kg.)	Time (sec.)	Vickers pyramid hardness no.	Standard deviation (VPN)
17-ST	2.5	10.0	143.0	1.28
	20.0	10.0	133.0	
	50.0	10.0	131.5	
	2.5	20.0	139.0	
	20.0	20.0	134.0	
	2.5	30.0	140.0	
	20.0	30.0	132.8	
	50.0	30.0	130.8	

TABLE 5.3: Vickers hardness results data for aluminium 17-ST alloy (from Emil Arbtin Jr. and Glenn Murphy, 1953 [9]).

Furthermore, one should note that the optimisation of the overall density was perhaps not the most pertinent to conduct. As it will be discussed in section 5.4, it is very likely that the tensile mechanical properties are dictated by the residual stresses and by the effects due to a second population of porosities. It could thus be interesting to perform a parametric study putting these at the forefront.

5.3.2 Reproducibility

SLM process demonstrated a satisfying reproducibility for the optimised set of parameters. However, non optimal values ($P=0.75P_{max}, v_s = 900[\frac{mm}{sec}]$) lead to higher variability for the hardness and the relative density. Since the energy density is bigger in that case ($76[\frac{J}{mm^3}]$), the explanation could be that the heat input was sufficient to trigger key hole instability at times, inducing porosity inside the melt pools. The phenomenon is illustrated in figure 5.7.

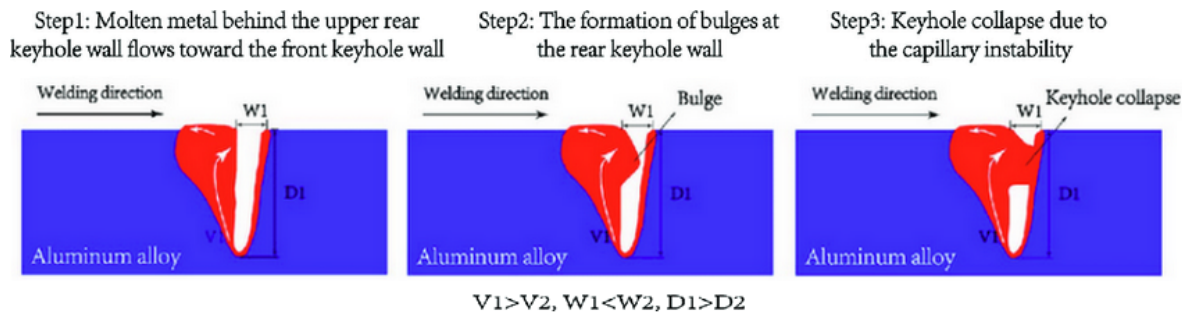


FIGURE 5.7: The diagram of keyhole collapse caused by the keyhole instability (from Huang et al., 2017 [27])

Relative density tended to be bigger for the samples of parameters ($P=0.75P_{max}, v_s = 900[\frac{mm}{sec}]$) scanned tardily. It may be due to the longer time left to exchange heat with the nearby unsintered powder. If the first scanned samples stayed at a significantly higher temperature compared to the others, they could be more prone to exceed the threshold leading to key hole instability. They would also have a bigger hydrogen solubility, as it increases with temperature (see figure 5.8) [18]. The apparition of porosities would thus be facilitated.

One sample, named X200-171024-8a, had notably low relative density. Its melt pools size distribution was compared to another specimen's (see section 4.2.2): the former was more homogeneous. Lots of porosities were present at the pools interface, which confirms that poor overlapping was achieved. The origin of this problem was not sorted out.

The hypothesis of thermal influence do not seem to stand for the specimens made with the optimised parameters. The energy density is 33% inferior, so the temperature must have reached lower values. No trend could thus be observed. The most determinant variables in terms of density and hardness seem to be the composition and the grain size distribution of the powder. A superior relative density was obtained after fresh powder was added to the recycled one (see section 4.2.2). However, an additional recycling iteration of the same powder caused a sensible decrease of ρ_{rel} . It dovetailed with a diminution of the alloying elements mass fractions. It is possible that both trends were correlated. Another possibility is that the contamination with moisture exceeded a critical value. The latter cannot be measured with ICP so this could not be verified.

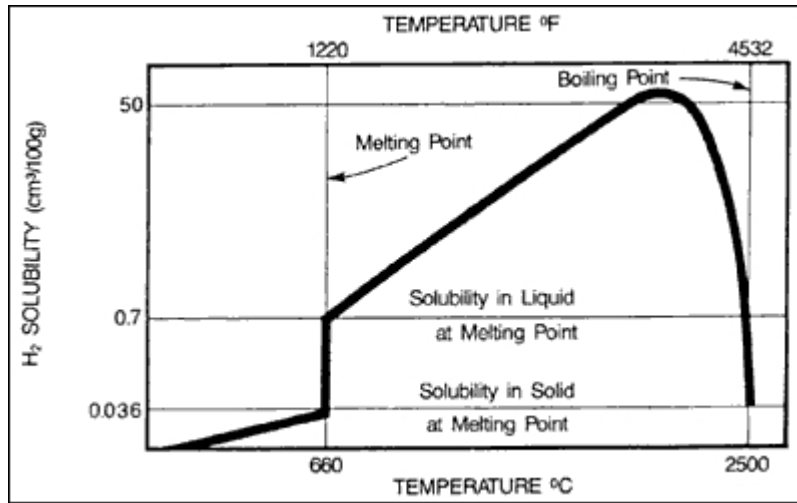


FIGURE 5.8: Solubility of hydrogen in aluminium (from Verhaeghe et al., 2003 [18])

5.4 Mechanical properties

The average tensile properties measures for AB specimens fell a bit short of the expectations. While σ_y was elevated compared to the standards, σ_u was less satisfactory ($\simeq 17\%$ beneath the highest value [17]). In addition, ϵ_f was lower than most values in table 2.1: up to $\simeq 58\%$ less than other results for samples built along z.

Results were compared to the *Aerostream* project's carried out by ULB, VUB and UCL universities in which AlSi10Mg tensile specimens were also built vertically and tested. The process parameters used for the project are unfortunately undisclosed. The comparison of the AB specimens is presented on figure 5.9. The properties obtained with the *Aerostream* project are obviously far better than what was obtained in this thesis for as-built specimens (and to what can be found in literature). The fracture strain was indeed three times bigger and the ultimate tensile strength 24% superior.

The shortcomings of the manufactured samples can be attributed at least partially to the presence of residual stresses. Consequent tension residual stresses were measured in the material. The actual stress during the tensile tests was thus greater than what was measured. In addition, there is a stress concentration due to the porosities. For spherical porosities, it is given by:

$$\sigma_{loc} = K_t \cdot \sigma_t$$

where σ_t is the applied stress and $K_t = \frac{3}{2}(1 + \frac{2}{7-5\nu}) \simeq 2$ [-] is the stress intensity factor [47].

The combination of the effects must have caused a shift of the actual local stress. The critical stress σ_c causing crack propagation was thus attained before the start of the voids coalescence, as illustrated in figure 5.10. As a result, the apparent tensile curve was truncated, reducing slightly σ_u and greatly ϵ_f . The yield strength, however, was the same as a residual stress free sample.

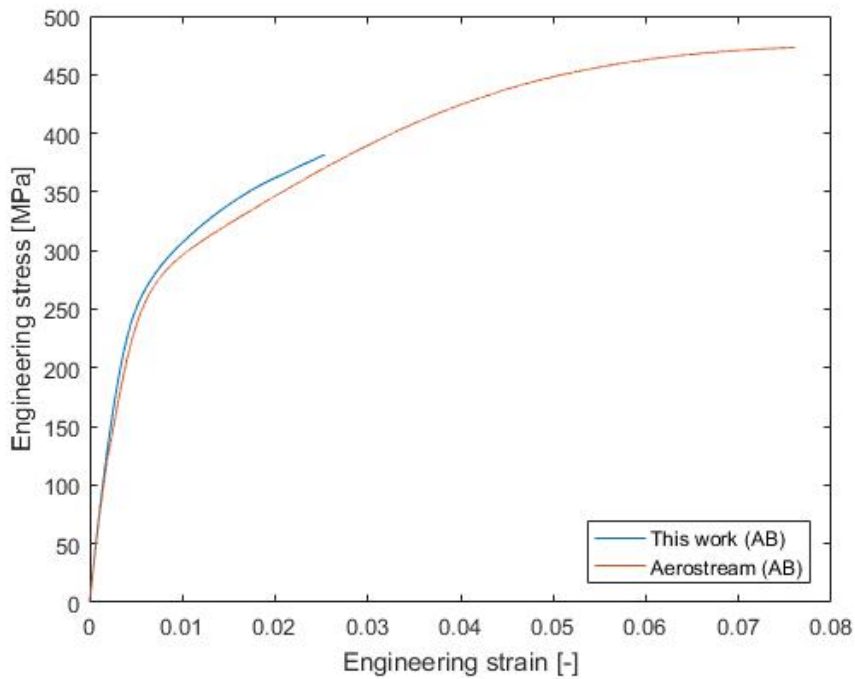


FIGURE 5.9: Engineering stress-strain tensile curves for as-built specimens of this work (in average) and of Aerostream project

This concurs with the data of table 2.2: the heating of the plate during the manufacturing process at 160°C, while reducing the residual stresses, increased the fracture strain by 77%. This could explain the differences with the better properties found in literature: as all the sources that obtained both high σ_u and ϵ_f did not specify the used process conditions, it is conceivable that they all used plate heating.

A consequent increase of ductility was observed for samples heat treated at 250°C and higher temperatures. This is due to the softening of the material induced by the microstructure modifications (see section 5.5). It could also be due to stress relief (SR). However, SR is not necessary to explain the results: the lowered maximal stress due to the softening could simply have been insufficient to reach the critical value σ_c impeding the ductile damage mechanism. The curves can thus not enable to certify if there was stress relief or not. Nevertheless, the heat treatment at 250°C permitted to have a good trade-off for the tensile properties: there was an increase of 250% of ϵ_f for decreases of only 12% and 11% of σ_y and σ_u respectively. This is quite different from what Mertens et al. observed for the same treatment (80% increase for ϵ_f and decreases of 10% and 2% for σ_y and σ_u) [43].

An increase of ultimate tensile strength was observed for the specimens that underwent a heat treatment at 150°C. This is seemingly due to artificial ageing: precipitated Mg_2Si particles constrain the dislocations displacement through the Orowan bowing phenomena as shown in figure 5.11, which induces hardening [20]. Artificial ageing can take place at 160°C (see section 2.6), it thus does not seem far-fetched that it could happen ten degrees below. Sample heated at 200°C demonstrated properties similar to the as-built ones. This is probably due to the compensation of the age-hardening effect with the microstructure softening.

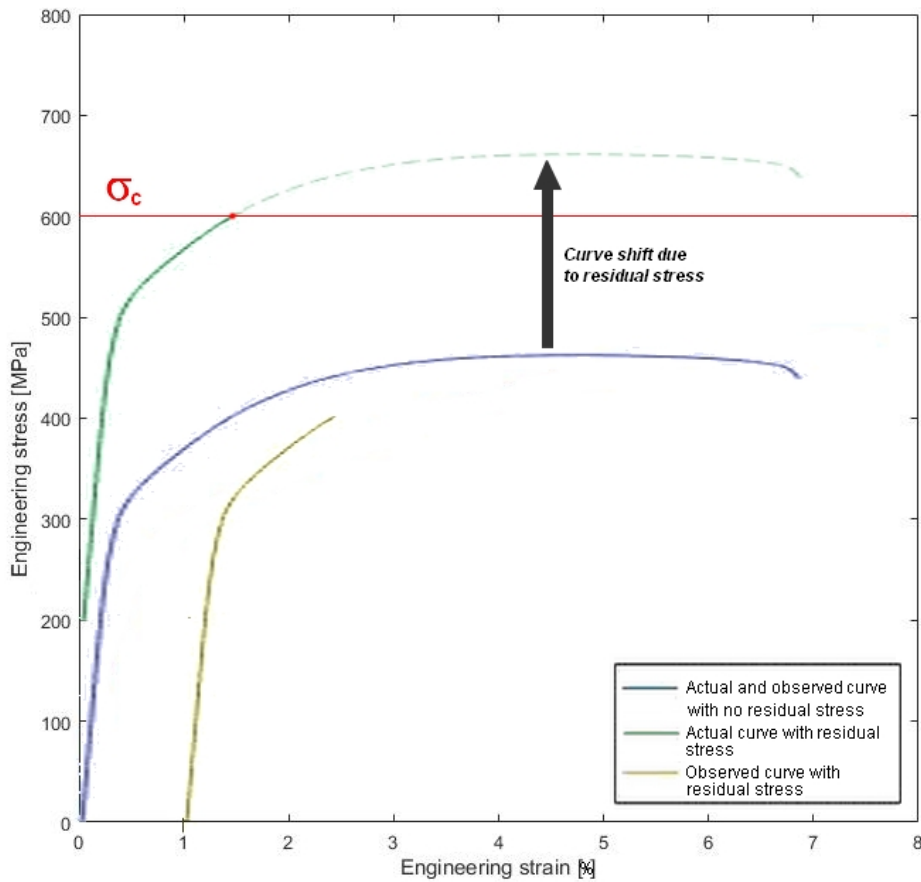


FIGURE 5.10: Illustration of the impact of residual stress on the observed tensile stress-strain curve

A noteworthy parallel can be made between the Vickers hardness and the ultimate tensile strength for AB and heat treated samples. The two are connected via a quasi-linear relationship as shown in table 5.4 and figure 5.12. A good empirical approximation can thus be obtained with $\sigma_u \simeq 2.88H_v$. Data was taken from sections 4.3 and 4.4.

HT	H_v [HV]	σ_u [MPa]	$\frac{H_v}{\sigma_u}$ [$\frac{HV}{MPa}$]
AB	136	381.7	2.81
150°	151.0	441.7	2.93
200°	133.6	382.0	2.86
250°	118.6	340.9	2.87
300°	86.7	252.9	2.92

TABLE 5.4: Relationship between Vickers hardness and ultimate tensile strength

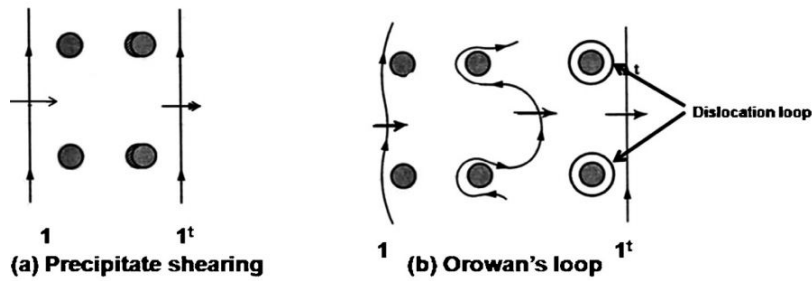


FIGURE 5.11: Schematic representation of dislocation/precipitate interaction under different tempering condition (a) underaged, (b) peak aged (from Ghosh et al., 2015 [20])

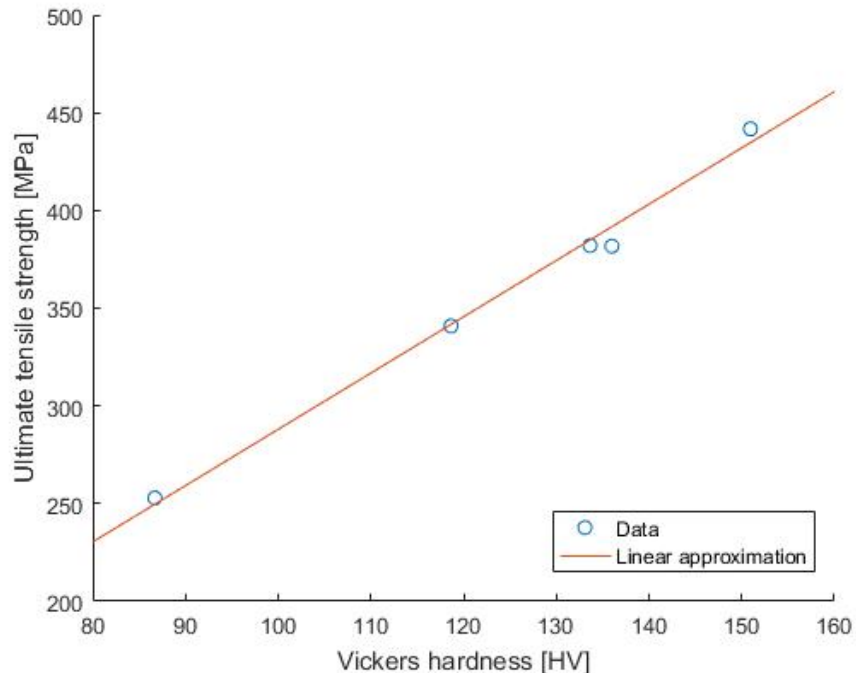


FIGURE 5.12: Average ultimate tensile strength for each heat treatment as a function of the Vickers hardness

5.5 Microstructure

Evolution of microstructure with post-treatments follows the expected spheroidization process. Optimisation of the final part microstructure - and thus mechanical properties - can however still be refined. A more accurate control of the parameters to ensure reproducibility could be needed. Further exploration of other sets of parameters, such as high temperature annealing with short holding time, could improve productivity without sacrificing quality of the part.

Similarity in the size of dimples on fractographs and microstructural cells is coherent with other results available in the literature. Dimple ridges could correspond to the ductile Al cells undergoing necking just before final failure.

5.5.1 Fractography

Step-like structures with width length similar to the hatch space were observed. It would suggest that failure takes place at the boundary between melt pools, where the microstructure is coarser, as discussed by Aboulkhair et al. [53].

Abundance of defects such as lack of fusion and porosities indicates that tensile failure is dictated by the presence of preferential sites for crack initiation. They are one cause for the low ductility of SLM alloys but not the only one. Annealing had no observable impact on these defects.

Evolution of microstructure with post-treatments follows the expected spheroidization process. Optimisation of the final part microstructure - and thus mechanical properties - can however still be refined. A more accurate control of the parameters to ensure reproducibility could be needed. Further exploration of other sets of parameters, such as high temperature annealing with short holding time, could improve productivity without sacrificing quality of the part.

Similarity in the size of dimples on fractographs and microstructural cells is coherent with other results available in the literature. Dimple ridges could correspond to the ductile Al cells undergoing necking just before final failure.

5.6 Residual stresses

Residual stresses measured with the hole method for an as-built sample were inferior to the ones of a specimen treated at 300°C. Other samples were sent for analysis, but the results were not received when this work was submitted due to logistical issues: the specimens were analysed in Malta, causing considerable transport time.

According to Vashista et al. (2012) [63], direct mathematical relation between the full width at half-maximum (FWHM) and residual stresses is difficult to obtain. This is due to the tendency of FWHM to increase with plastic deformation and grain refinement. They however observed experimentally a non-linear increase of FWHM with residual stresses.

We indeed observe a decrease of FWHM with the temperature of the heat treatment. It could mean that the heat treatment relieves stresses as intended. Only the as-built sample seems to defy this logic and present a FWHM lower than some heat-treated samples. However this could be explained by the geometrical difference of the as-built. While the heat-treated samples used for XRD are complete $5 \times 5 \times 5$ [mm³] cubes, the as-built is $1 \times 1 \times 1$ [cm³] cube cut in half. The higher volume explains the higher peak, and the cut may have allow a part of the residual stresses to relax by deforming the part, and thus causing the narrowing of the peak.

Nonetheless, the sample heat-treated at 300°C for 2 hours remains far from stress-free according to the results from Lam et al. (2015) [33]. They obtained for the same peak a FWHM of 0.361, which is much smaller than everything we managed to obtain. However, as discussed above, other parameters could play a role in this difference.

Results obtained via the hole-drilling method appears counter-intuitive. As-built SLM samples are known for their unwanted high residual stresses, which is one the reasons for the development of many post-processes aiming at reducing them. The very low value of residual stresses in the as-built sample across the entire hole depth is thus unexpected. On the other hand, the heat treated sample present residual stresses more adequate with literature. They should however be lower than in the as-built.

A part of the answer could lie in the machining applied to the two parts. Indeed, installation of gauges for the strain measurements during the drilling of the hole requires a certain level of surface smoothness. The intrinsic bad surface finish of the SLM process imposed the use of a post-process to reduce rugosity. The parts were milled with cutters adapted to hard steels. The inadequacy of the tools used have probably induced compressive residual stresses near the surface. This phenomenon has probably affected the stress distribution inside the parts, but is not able on its own to explain the state of the as-built sample. Additional residual stress measurements on a larger series of samples with the same post-treatment could help to understand the causes of this phenomenon.

Chapter 6

Conclusion

In this master thesis, an analysis of the impact of stress relief heat treatments was carried out. Results for the residual stresses measurements were unsatisfactory: they suggested that the residual stresses of heat treated samples were equivalent to or bigger than the ones of as-built samples. A possible explanation was provided.

Nevertheless, multiple instructive observations were made. The importance of powder monitoring was first highlighted. The assessment of the relative density measurements was then conducted. Results indicated that hydrostatic weighing (after polishing) and relative optical density image analysis methods could constitute bound values for the actual relative density value.

Optimal process parameters were identified with the aim of achieving high relative density. The reproducibility was addressed, both for the optimal parameters and for suboptimal ones. The former led to relative density values ranging from 99.4% to 99.9%. High hardness values were obtained compared to literature. The underlying reasons were identified.

Plausible hypotheses were made to explain the mechanical properties for as-built and heat-treated specimens. The major role of residual stresses was emphasised. The use of a pre-heating plate during the manufacturing process seems to substantially improve the tensile properties. An empirical relationship linking the ultimate tensile strength to the hardness was suggested.

The direct link between the very fine microstructure of SLM parts and their mechanical properties was discussed. Heat treatments have shown to affect deeply the microstructure, mainly by the process of spheroidization. Design of heat treatments specifically thought for AM alloys is necessary to ensure better control of the final properties.

This thesis leaves open numerous paths of investigation. An in-depth analysis of the variables influencing the residual stresses - such as machining and heat treatment conditions - could bring clarity regarding the reasons behind the surprising results of this work. A manufacturing process optimisation could also be carried out to minimise the residuals stresses in the parts, as their critical role was pointed out. Finally, other inherent issues of SLM should be addressed, such as fatigue strength.

Appendix A

Batches fabrication and hardness/density measurements details

A.1 Process parameters and measured hardness/density properties

All manufacturing set values are gathered in table A.1. Dimensions of the cubic, cylindrical and parallelepiped specimens are noted in accordance with figure 3.5.

Batch name	Contour	Type	Dimensions [mm]	Specimen name	$\frac{P}{P_{max}} [-]$	$v_s [\frac{mm}{s}]$	$E_d [\frac{J}{mm^3}]$	$H_v [HV]$	ρ_{rel}^1	$\rho_{a,rel}^2$	$\rho_{a,rel}^3$
X200-171024	No	Cubic	L=10	1	0.85	900	86.13	135.9	-	99.24	-
				2		1000	77.52	133.7	-	99.08	-
				3		1059	73.20	135.5	-	99.00	-
				4		1500	51.68	137.3	-	99.38	-
				5	1	900	101.33	131.3	-	98.81	-
				6		1059	86.12	132.7	-	98.83	-
				7	0.75	1200	57	137.3	-	99.49	-
				7a				137.9	-	99.33	-
				7b				137.9	-	99.45	-
				8		900	76	135.5	-	99.23	-
				8a				133.7	-	98.77	-
				8b				136.1	-	99.23	-
X200-180109	No	Cubic	L=10	7c	0.75	1200	57	141.0	99.77	99.33	99.77
				7d				138.6	-	99.45	-
				7e				140.0	-	99.44	-
				7n				141.4	-	99.45	-
				7g				139.4	-	99.50	-
				7h				139.2	99.51	99.52	99.32
				7i				140.3	-	99.48	-
				7j				140.9	-	99.48	-
				7k				140.6	-	99.37	-
				7l				139.8	-	99.38	-
				7m				139.0	99.65	99.29	99.48
				7n				140.0	99.51	99.24	99.48
				7o				138.7	99.52	99.49	99.49
				7p				140.6	-	99.37	-

Continued on next page

TABLE A.1: Manufacturing process parameters

Table A.1 – *Continued from previous page*

Batch name	Contour	Type	Dimensions [mm]	Specimen name	$\frac{P}{P_{max}} [-]$	$v_s [\frac{mm}{s}]$	$E_d [\frac{J}{mm^3}]$	$H_v [HV]$	ρ_{rel}	$\rho_{a,rel}$	$\rho_{a,rel}$
				7q 8c 8d 8e 8f 8g 8h 8i 8j 8k 8l 8m 8n 8o 8p 8q		900	76	139.0 139.4 138.8 138.0 138.3 138.2 139.5 134.6 138.0 138.0 136.5 139.0 140.4 138.5 138.7 138.7	- - - - - - - - - - - - - - - - - -	99.31 99.27 99.20 99.29 99.50 99.37 99.51 99.18 99.44 99.41 99.39 99.31 99.29 99.54 99.35 99.43	- - - - - - - - - - - - - - - - - -
X200-180220	No	Cubic	L=5	TT150-2 TT200-2 TT300-2 TT300-2-plaque TT150-2-real TT200-2-real TT250-2-real TT300-2-real TT300-5min-real	0.75	1200	57	- - - - 99.83 99.82 99.77 99.77 99.85	- - - - - - - - -	- - - - - - - - -	
X200-180222	No	Cubic	L=10	12	0.75	1200	57	-	-	98.30	-

Continued on next page

TABLE A.1: Manufacturing process parameters

Table A.1 – *Continued from previous page*

Batch name	Contour	Type	Dimensions [mm]	Specimen name	$\frac{P}{P_{max}} [-]$	$v_s [\frac{mm}{s}]$	$E_d [\frac{J}{mm^3}]$	$H_v [HV]$	ρ_{rel}	$\rho_{a,rel}$	$\rho_{a,rel}$
				13				-	-	98.90	-
X200-180228	Yes	Cylindrical	D=6, H=2	1	0.75	1200	57	-	98.87	-	-
				2			-	-	99.23	-	-
				3			-	-	-	-	-
X200180313	Yes	Cylindrical	D=6, H=10	1	0.75	1200	57	-	99.74	-	-
				2			-	-	99.77	-	-
			D=12, H=10	3			-	-	99.75	-	-
				4			-	-	99.73	-	-
	No	Parallelepiped	H=10, W=40, L=120	???			-	-	-	-	-
				???			-	-	-	-	-
X200-180315	No	Parallelepiped	H=10, W=40, L=115	???	0.75	1200	57	-	-	-	-
X200-180319	No	Cubic	L=10	cub 1	0.75	1200	57	139.5	99.88	-	99.90
				cub 2			-	140.8	99.81	-	99.80
				cub 3			-	140.1	99.79	-	99.61
				cub 4			-	138.6	99.85	-	99.77
				cub 5			-	139.9	99.87	-	99.68
	Yes	Cylindrical	D=6, H=10	TT300-1-real				116.6	99.86	-	-
				TT225-2-real			-	-	99.85	-	-
				cyl 1			-	-	99.92	-	-
				cyl 2			-	-	99.85	-	-
	No	Parallelepiped	D=12, H=10	cyl 3			-	-	99.82	-	-
				cyl 4			-	-	-	-	-
X200-180417	Yes	Tensile	(see section 3.2)	1, ..., 24 25	0.75	1200	57	-	138.0	99.80	-

Continued on next page

TABLE A.1: Manufacturing process parameters

Table A.1 – *Continued from previous page*

Batch name	Contour	Type	Dimensions [mm]	Specimen name	$\frac{P}{P_{max}} [-]$	$v_s [\frac{mm}{s}]$	$E_d [\frac{J}{mm^3}]$	$H_v [HV]$	ρ_{rel}	$\rho_{a,rel}$	$\rho_{a,rel}$
	No	Cubic	L=10	26, 27, 28 A B C				- 135.9 138.0 134.1	- 99.64 99.70 99.67	- - - -	- 99.44 99.54 99.44

¹Measured by RODIA [%].²Measured by HW (AB specimens) [%].³Measured by HW (polished specimens) [%].

A.2 Specimens positioning, fabrication orders and sintering times

A.2.1 Batch X200-171024



FIGURE A.1: Specimens positions, order of fabrication and sintering times for batch X200-171024

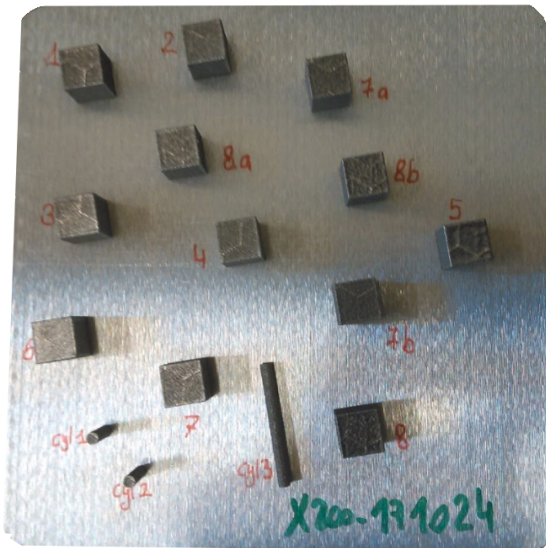


FIGURE A.2: Photography of the manufacturing plate after completion of the fabrication of batch X200-171024

A.2.2 Batch X200-180109

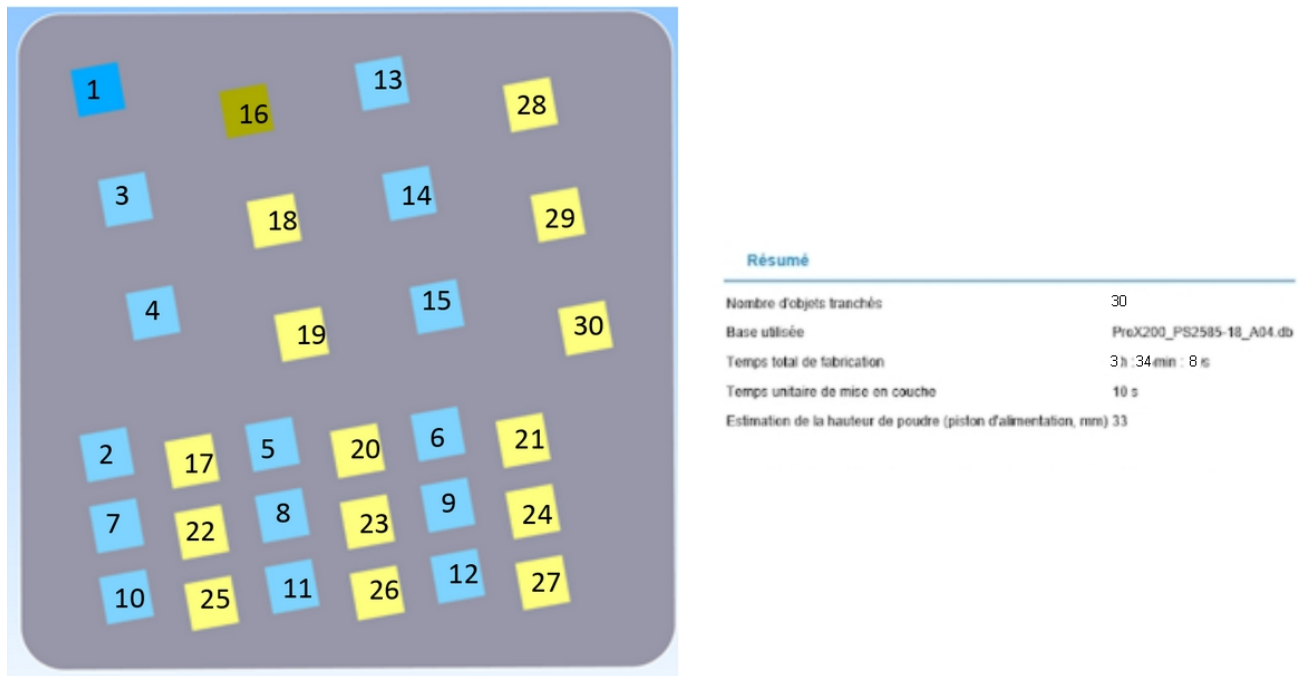


FIGURE A.3: Specimens positions, order of fabrication and sintering times for batch X200-180109

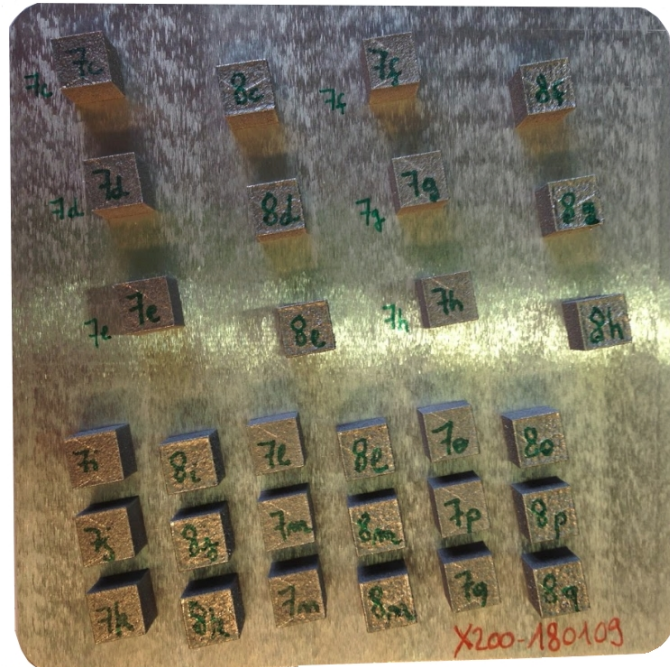


FIGURE A.4: Photography of the manufacturing plate after completion of the fabrication of batch X200-180109

A.2.3 Batch X200-180220

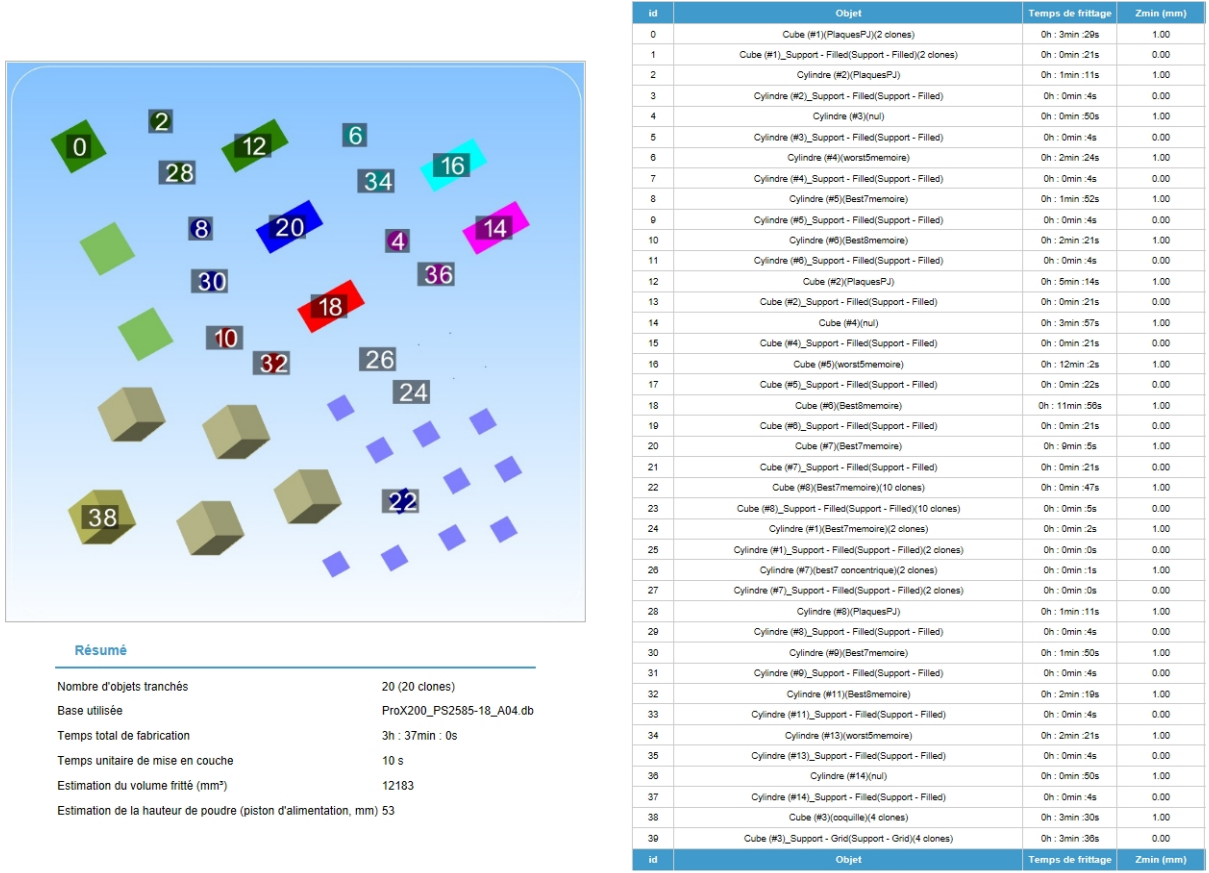


FIGURE A.5: Specimens positions, order of fabrication and sintering times for batch X200-180220

A.2.4 Batch X200-180222



FIGURE A.6: Specimens positions, order of fabrication and sintering times for batch X200-180222



FIGURE A.7: Photography of the manufacturing plate after completion of the fabrication of batch X200-180222

A.2.5 Batch X200-180228



FIGURE A.8: Specimens positions, order of fabrication and sintering times for batch X200-180228

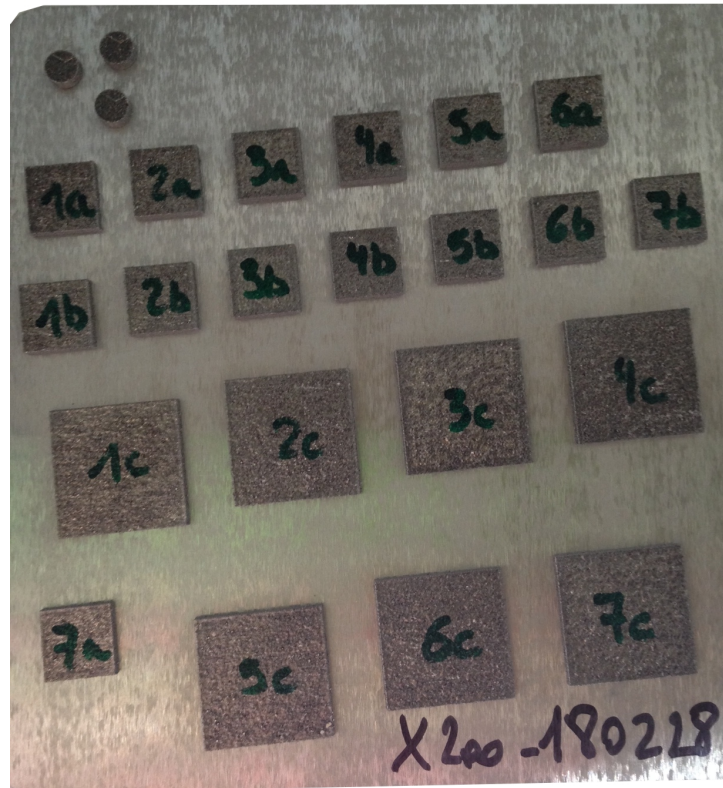


FIGURE A.9: Photography of the manufacturing plate after completion of the fabrication of batch X200-180228

A.2.6 Batch X200-180313



FIGURE A.10: Specimens positions, order of fabrication and sintering times for batch X200-180313



FIGURE A.11: Photography of the manufacturing plate after completion of the fabrication of batch X200-180313

A.2.7 Batch X200-180315

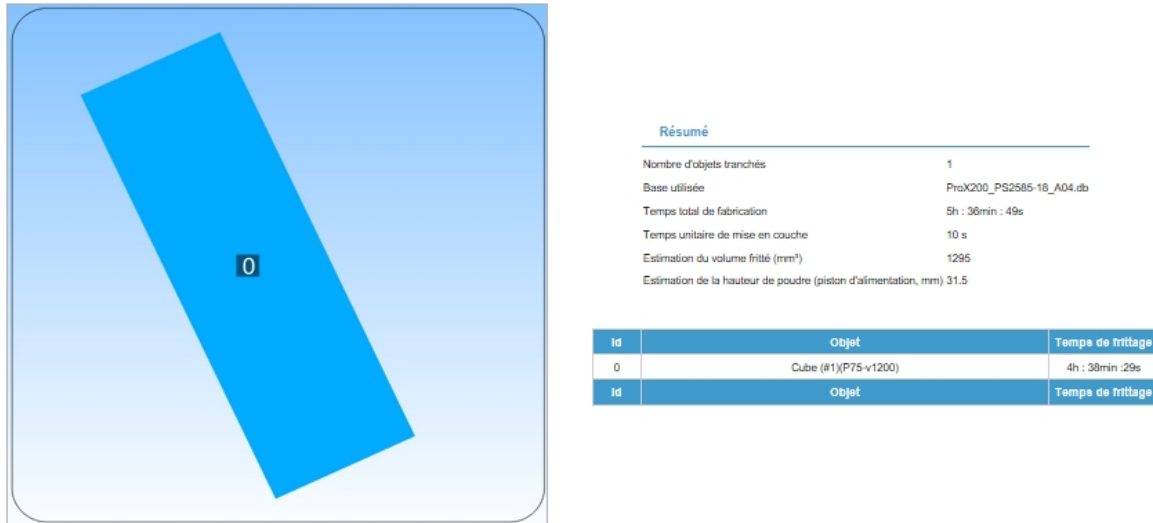


FIGURE A.12: Specimens positions, order of fabrication and sintering times for batch X200-180315



FIGURE A.13: Photography of the manufacturing plate after completion of the fabrication of batch X200-180315

A.2.8 Batch X200-180319

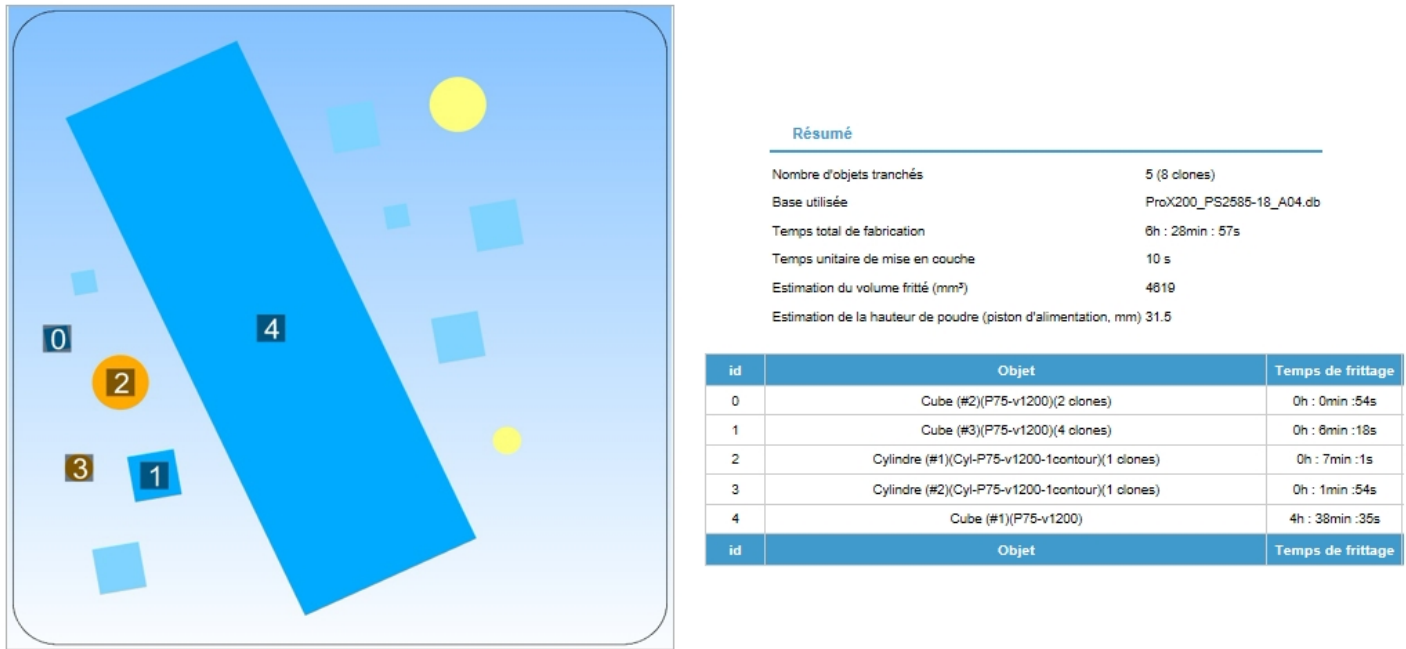


FIGURE A.14: Specimens positions, order of fabrication and sintering times for batch X200-180319

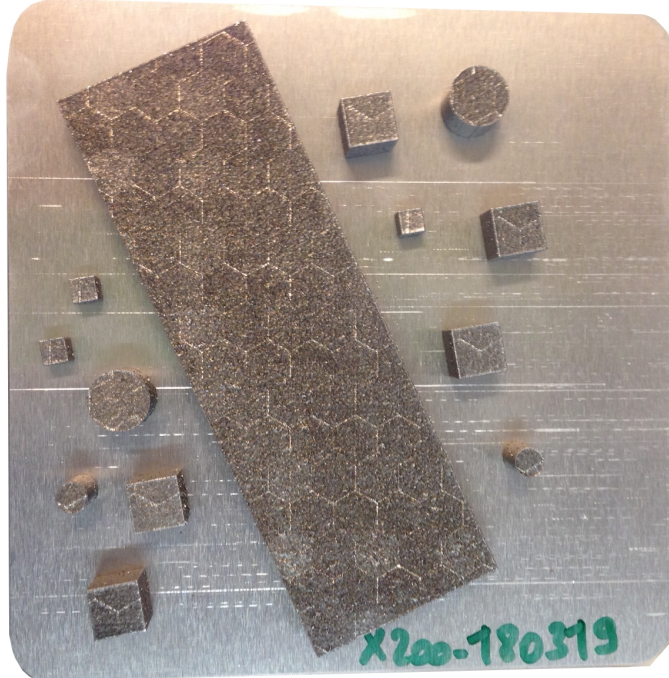


FIGURE A.15: Photography of the manufacturing plate after completion of the fabrication of batch X200-180319

A.2.9 Batch X200-180417



FIGURE A.16: Photography of the manufacturing plate after completion of the fabrication of batch X200-180417

Appendix B

Tensile properties details

The measured tensile properties for every tested specimens are gathered in this section. Young's modulus values that are in parenthesis were not used in the average computations of sections 4.3 and 4.4, as the corresponding samples slipped between the grips during the tests. A non-linear behaviour was indeed observed.

B.1 As-built samples

Specimen	Contour	E [GPa]	σ_y [MPa]	σ_u [MPa]	ϵ_f [%]
X200-180417-1	Yes	(74.6)	271.8	366.4	2.2
X200-180417-2	Yes	68.2	291.4	388.3	2.4
X200-180417-3	Yes	64.7	276	-	-
X200-180417-16	Yes	64.7	259.3	368.0	2.3
X200-180417-17	Yes	66.1	255.4	406.4	3.0
X200-180417-A	No	62.0	255.3	379.2	2.8

TABLE B.1: Tensile mechanical properties of the as-built specimens from batch X200-180417

B.1.1 Heat treated samples

Specimen	Contour	HT	E [GPa]	σ_y [MPa]	σ_u [MPa]	ϵ_f [%]
X200-180417-13	Yes	150°C (2h)	70.9	290.2	436.2	2.8
X200-180417-14	Yes	150°C (2h)	67.9	286.8	442.7	2.9
X200-180417-B	Yes	150°C (2h)	66.5	287.6	446.2	3.5
X200-180417-10	Yes	200°C (2h)	72.5	245.9	393.4	2.8
X200-180417-11	Yes	200°C (2h)	71.7	244.8	370.6	2.4
X200-180417-7	Yes	250°C (2h)	71.3	231.1	334.5	16.6
X200-180417-8	Yes	250°C (2h)	69.6	239.2	347.4	16.4
X200-180417-9	Yes	250°C (2h)	71.0	227.7	$\simeq 328.7$	-
X200-180417-4	Yes	300°C (2h)	(81.6)	168.9	249.6	29.6
X200-180417-5	Yes	300°C (2h)	68.3	172.4	256.24	29.8
X200-180417-6	Yes	300°C (2h)	69.5	168.5	$\simeq 242.5$	-

TABLE B.2: Tensile mechanical properties of the heat treated specimens from batch X200-180417

Appendix C

Extract of Vickers hardness conversion table (HV10)

Diagonal length [mm]	0	1	2	3	4	5	6	7	8	9
0.34	160	160	159	158	157	156	155	154	153	152
0.35	151.4	150.5	149.7	148.8	148.0	147.1	146.3	145.5	144.7	143.9
0.36	143.1	142.3	141.5	140.7	140.0	139.2	138.4	137.7	136.9	136.2
0.37	135.5	134.7	134.0	133.3	132.6	131.9	131.2	130.5	129.8	129.1
0.38	128.4	127.7	127.1	126.4	125.8	125.1	124.5	123.8	123.2	122.6
0.39	121.9	121.3	120.7	120.1	119.5	118.9	118.3	117.7	117.1	116.5
0.40	115.9	115.3	114.8	114.2	113.6	113.1	112.5	111.9	111.4	110.9
0.41	110.3	109.8	109.3	108.7	108.2	107.7	107.2	106.6	106.1	105.6
0.42	105.1	104.6	104.1	103.6	103.1	102.7	102.2	101.7	101.2	100.8
0.43	100.3	99.8	99.4	98.9	98.5	98.0	97.6	97.1	96.7	96.2
0.44	95.8	95.3	94.9	94.5	94.1	93.6	93.2	92.8	92.4	92.0
0.45	91.6	91.2	90.8	90.4	90.0	89.6	89.2	88.8	88.4	88.0
0.46	87.6	87.3	86.9	86.5	86.1	85.8	85.4	85.0	84.7	85.3
0.47	84.0	83.6	83.2	82.9	82.5	82.2	81.8	81.5	81.2	80.8
0.48	80.5	80.2	79.8	79.5	79.2	78.8	78.5	78.2	77.9	77.6
0.49	77.2	76.9	76.6	76.3	76.0	75.7	75.4	75.1	74.8	74.5
0.50	74.2	73.9	73.6	73.3	73.0	72.7	72.4	72.1	71.9	71.6
0.51	71.3	71.0	70.7	70.5	70.2	69.9	69.6	69.4	69.1	68.8
0.52	68.6	68.3	68.1	67.8	68.5	67.3	67.0	66.8	66.5	66.3
0.53	66.0	65.8	65.5	65.3	65.0	64.8	64.5	64.3	64.1	63.8
0.54	63.6	63.4	63.1	62.9	62.7	62.4	62.2	62.0	61.7	61.5

TABLE C.1: Extract of Vickers hardness conversion table (HV10)

Appendix D

Procedure for the confidence intervals computation

D.1 Apparent relative density

The hydrostatic weighting method requires to weight the analysed samples two times; once in air and once in water. The measurements data of the two weightings are subjected to a certain spreading - especially large in the case of underwater measurements. Both of the tests imprecisions must thus be taken into account when computing the confidence intervals (CI) for $\rho_{a,rel}$. The following procedure was followed:

- Computation of the standard deviation SD_x for the two data samples of observed mass values $\{x_1, x_2, \dots, x_N\}$ with the formula below:

$$SD_x = \sqrt{\frac{\sum_{i=1}^N (x_i - \bar{x})^2}{N - 1}}$$

where N the sample size and \bar{x} is the mean of the observed values.

- Determination of the CI range at a 95 [%] confidence level for each data sample with the following formula:

$$CI = \bar{x} \pm 1.96 \frac{SD_x}{\sqrt{N}}$$

- Use of the mean values incremented by the extreme values of the CI for both W_a and W_w in the formula:

$$\rho_a = \frac{W_a}{W_a - W_w} \cdot \rho_w$$

so as to maximise the absolute value of the difference with \bar{x} . This difference is then equal to the CI half length for a 95 [%] confidence level. One should note that the following hypotheses were made: the method is unbiased and the tests are depending one on another. The latter hypothesis maximises the CI. It is used for reasons of caution. The validity of the hypotheses is discussed in section 5.2.

D.2 Vickers hardness

Hardness measurements of a given sample are also prone to having a certain variability. CI must thus be computed to assess the method precision. The CI is first calculated for the data sample composed of the mean diagonals length of the indents. For this purpose, one follows the same two first steps as for the hydrostatic weighting. The CI range is then multiplied by 800 to find the hardness's one. This is done in accordance with the observation that the maximal hardness variation for a change of 0.001 [mm] is 0.8 [HV] in table C.1 for $H_v < 147.1$ [HV].

Appendix E

Reproducibility study additional plots

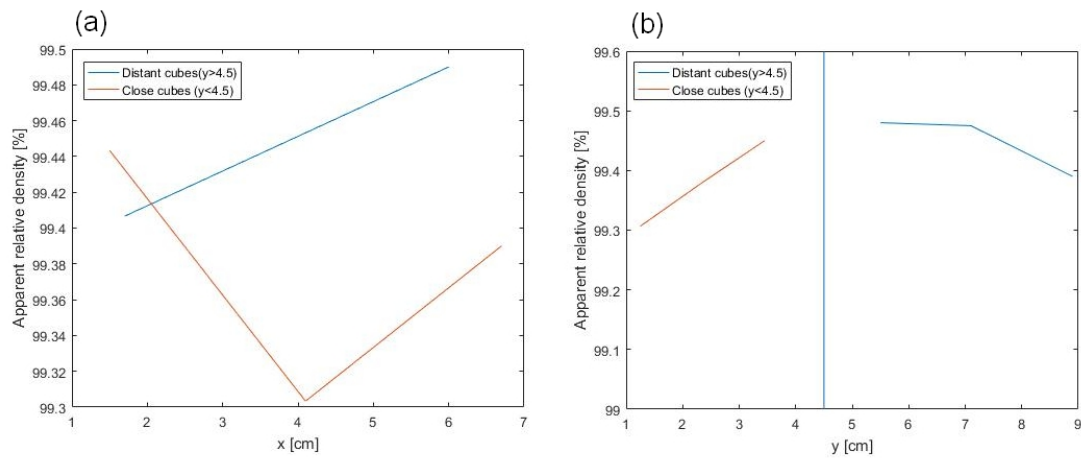


FIGURE E.1: Apparent relative density of batch X200-180109 type ($P=0.75 \text{ P}_{\max}$; $v_s=1200 \frac{\text{mm}}{\text{sec}}$) samples as a function of the (a) x coordinate (b) y coordinate

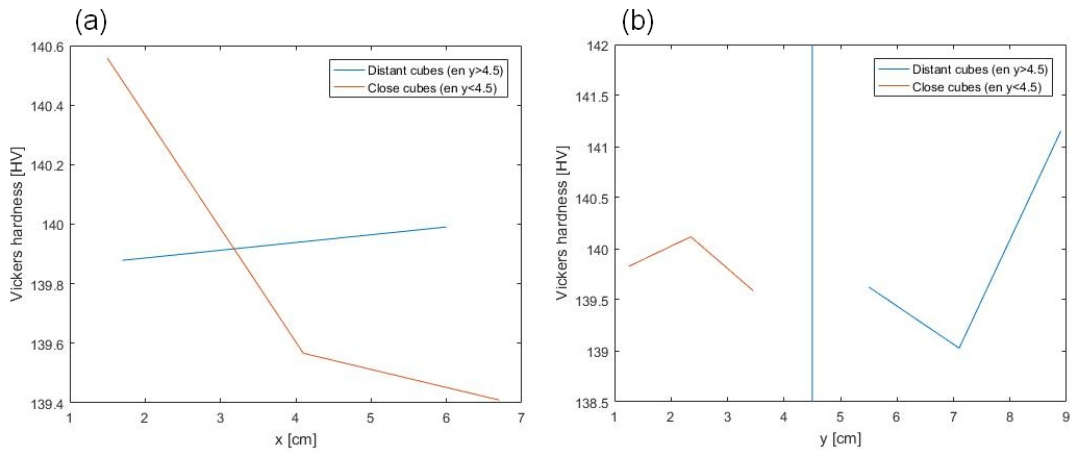


FIGURE E.2: Vickers hardness of batch X200-180109 type ($P=0.75 \text{ P}_{\max}$; $v_s=1200 \frac{\text{mm}}{\text{sec}}$) samples as a function of the (a) x coordinate (b) y coordinate

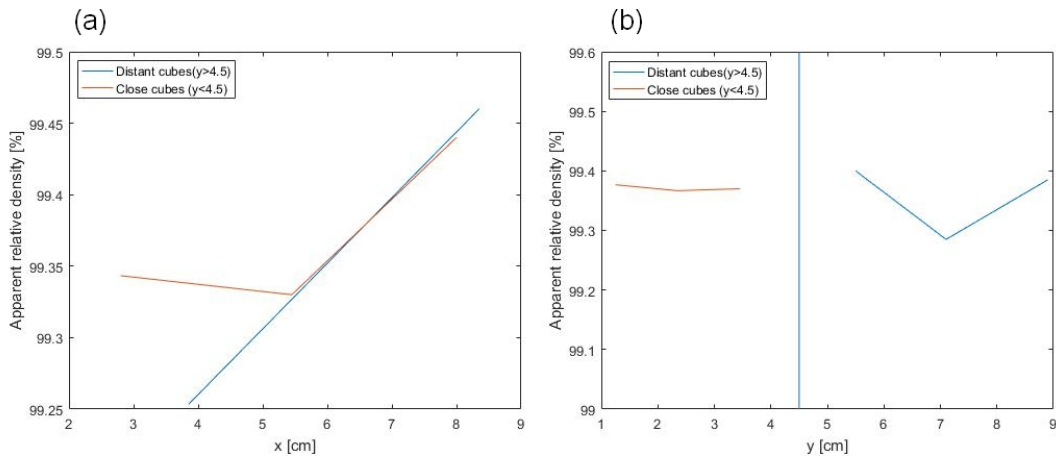


FIGURE E.3: Apparent relative density of batch X200-180109 type ($P=0.75 \text{ Pmax}$; $v_s=900 \frac{\text{mm}}{\text{sec}}$) samples as a function of the (a) x coordinate (b) y coordinate

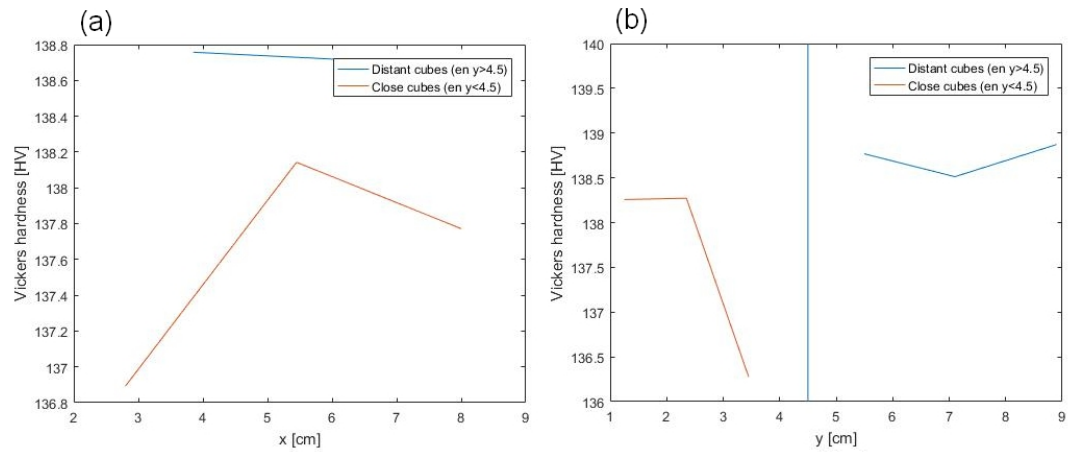


FIGURE E.4: Vickers hardness of batch X200-180109 type ($P=0.75 \text{ Pmax}$; $v_s=900 \frac{\text{mm}}{\text{sec}}$) samples as a function of the (a) x coordinate (b) y coordinate

Bibliography

- [1] *3D Systems Inc, Direct metal printers: Metal Additive Manufacturing with the ProXTM DMP 3D printers.* 2016. URL: https://www.3dsystems.com/sites/default/files/2017-01/3D-Systems_DMP_Tech_Specs_USEN_2017.01.23_WEB.pdf (visited on 13/04/2018).
- [2] Nesma T. Aboulkhair et al. 'Improving the fatigue behaviour of a selectively laser melted aluminium alloy: Influence of heat treatment and surface quality'. In: *Mater. Des.* 104 (2016), pp. 174–182. URL: <https://www.sciencedirect.com/science/article/pii/S0264127516306426>.
- [3] Nesma T. Aboulkhair et al. 'On the formation of AlSi10Mg single tracks and layers in selective laser melting: Microstructure and nano-mechanical properties'. In: *Journal of Materials Processing Tech.* 230.Complete (2016), pp. 88–98. URL: <https://www.sciencedirect.com/science/article/pii/S0924013615302028>.
- [4] Nesma T. Aboulkhair et al. 'On the Precipitation Hardening of Selective Laser Melted AlSi10Mg'. In: *Metall. Mater. Trans. A* 46 (2015), pp. 3337–3341. URL: <https://link.springer.com/article/10.1007/s11661-015-2980-7>.
- [5] Nesma T. Aboulkhair et al. 'Reducing porosity in AlSi10Mg parts processed by selective laser melting'. In: *Additive Manufacturing* 1-4 (2014). Inaugural Issue, pp. 77–86. URL: <http://www.sciencedirect.com/science/article/pii/S2214860414000062>.
- [6] Nesma T. Aboulkhair et al. 'Selective laser melting of aluminum alloys'. In: *MRS Bulletin* 42.4 (2017), 311–319. URL: <https://www.cambridge.org/core/journals/mrs-bulletin/article/selective-laser-melting-of-aluminum-alloys/EC1799D2905FA070C95CCAB8A91BF64D>.
- [7] Nesma T. Aboulkhair et al. 'The microstructure and mechanical properties of selectively laser melted AlSi10Mg: The effect of a conventional T6-like heat treatment'. In: *Materials Science and Engineering: A* 667 (2016), pp. 139–146. URL: <http://www.sciencedirect.com/science/article/pii/S0921509316304890>.
- [8] *Aerospace Specification Metals Inc., Aluminum 6061-T6; 6061-T651.* 2000. URL: <http://asm.matweb.com/search/SpecificMaterial.asp?bassnum=ma6061t6> (visited on 27/05/2018).
- [9] Emil Arbtin and Glenn Murphy. 'Correlation of Vickers hardness number, modulus of elasticity, and the yield strength for ductile metals'. In: *Ames Laboratory ISC Technical Reports*. 50 (1953), pp. 1–27. URL: https://lib.dr.iastate.edu/cgi/viewcontent.cgi?article=1057&context=ameslab_iscreports.
- [10] *ASTM E837-13a, Standard Test Method for Determining Residual Stresses by the Hole-Drilling Strain-Gage Method.* ASTM International. 2013. URL: <http://www.astm.org/>.
- [11] *Beckman Coulter, Inc. - COULTER LS SERIES Product Manual.* 2011. URL: <https://www.beckmancoulter.com/wsportal/techdocs?docname=4237214EA.pdf>.

- [12] Erhard Brandl et al. 'Additive manufactured AlSi10Mg samples using Selective Laser Melting (SLM): Microstructure, high cycle fatigue, and fracture behavior'. In: *Materials & Design* 34 (2012), pp. 159 –169. URL: <http://www.sciencedirect.com/science/article/pii/S0261306911005590>.
- [13] *Concept Laser - The technology*. URL: <https://www.concept-laser.de/en/technology.html> (visited on 10/06/2018).
- [14] John Daintith. *A Dictionary of Physics*. Oxford University Press, 2009. URL: <http://www.oxfordreference.com/view/10.1093/acref/9780199233991.001.0001/acref-9780199233991>.
- [15] Pauline Delroisse et al. 'Effect of strut orientation on the microstructure heterogeneities in AlSi10Mg lattices processed by selective laser melting'. In: *Scripta Materialia* 141 (2017), pp. 32 –35. URL: <https://www.sciencedirect.com/science/article/pii/S1359646217304256>.
- [16] B. Denkena, M. Reichstein and L. de Leon Garcia. 'Milling Induced Residual Stresses in Structural Parts out of Forged Aluminum Alloys'. In: *Sixth International Conference on HIGH SPEED MACHINING* (2007). Conference paper, pp. 1–4. URL: http://www.transport-research.info/sites/default/files/project/documents/20121115_114306_73510_CIRP_HSM_2007.pdf.
- [17] EOS GmbH – electro optical systems, *Material data sheet: EOS aluminium AlSi10Mg*. 2014. URL: http://gpiprototype.com/images/PDF/EOS_Aluminium_AlSi10Mg_en.pdf (visited on 21/05/2018).
- [18] Verhaeghe G, Hilton P and Stuart Barnes. 'Achieving Low-Porosity Laser Welds in Aerospace Aluminium Alloy'. In: 3 (Sept. 2003), pp. 1–7. URL: <https://www.twi-global.com/technical-knowledge/published-papers/achieving-low-porosity-laser-welds-in-aerospace-aluminium-alloy-september-2003/>.
- [19] G2MT Laboratories - *Residual Stress Measurement by Center Hole Drilling per ASTM E 837*. URL: <http://www.g2mtlabs.com/residual-stress-measurement-rosette-hole-drilling-astm-837/> (visited on 28/05/2018).
- [20] A. Ghosh et al. 'Effect of tempering conditions on dynamic deformation behaviour of an aluminium-lithium alloy'. In: *Materials & Design* 81 (2015), pp. 1 – 10. URL: <http://www.sciencedirect.com/science/article/pii/S0261306915002320>.
- [21] Christian Haase et al. 'Exploiting Process-Related Advantages of Selective Laser Melting for the Production of High-Manganese Steel.' In: *Materials* 10(1).56 (2017). URL: <https://www.ncbi.nlm.nih.gov/pubmed/28772416>.
- [22] Éva Hidvégi and Elisabeth Kovács-Csetényi. 'Study of the loss of magnesium in an AlMgSi alloy'. In: *Materials Science and Engineering* 27.1 (1977), pp. 39 –43. URL: <http://www.sciencedirect.com/science/article/pii/0025541677901926>.
- [23] Ahmed H.Maamoun et al. 'Thermal post-processing of AlSi10Mg parts produced by Selective Laser Melting using recycled powder'. In: *Mater. Sci. Eng. A* 682 (2017), 509–517. URL: <https://www.sciencedirect.com/science/article/pii/S2214860418300617>.
- [24] N.E. Hodge, R.M. Ferencz and J.M. Solberg. 'Implementation of a thermo-mechanical model for the simulation of selective laser melting'. In: *Computational Mechanics* 54 (2014), pp. 33–51. URL: <https://link.springer.com/article/10.1007/s00466-014-1024-2>.

- [25] Simon Hoeges. *Additive manufacturing technologies: 6 Unique Benefits Of Selective Laser Melting*. 2017. URL: <http://sintermedia.gkn.com/blog/the-advantages-of-selective-laser-melting> (visited on 12/04/2018).
- [26] Foroogh Hosseinzadeh. *Research activity*. URL: http://technology.open.ac.uk/materials/staff/Staff_fh-2.htm (visited on 28/05/2018).
- [27] Lijin Huang et al. 'Numerical study of keyhole instability and porosity formation mechanism in laser welding of aluminum alloy and steel'. In: 252 (Oct. 2017), pp. 421–431. URL: <https://www.sciencedirect.com/science/article/pii/S0924013617304600>.
- [28] INCONEL® alloy 718. Special Metals Corporation. 2007. URL: http://www.specialmetals.com/assets/smc/documents/inconel_alloy_718.pdf.
- [29] S J. Vonk, G S. Hoppin and K W. Benn. 'Hot Isostatic Pressing of Aluminum Alloy Castings'. In: (June 1981), pp. 1–64. URL: <http://www.dtic.mil/dtic/tr/fulltext/u2/a105562.pdf>.
- [30] Frank I. Katch. 'Apparent Body Density and Variability during Underwater Weighing'. In: *Research Quarterly. American Association for Health, Physical Education and Recreation* 39.4 (1968), pp. 993–999. URL: <https://shapeamerica.tandfonline.com/doi/abs/10.1080/10671188.1968.10613450>.
- [31] K. Kempen et al. 'Mechanical Properties of AlSi10Mg Produced by Selective Laser Melting'. In: *Physics Procedia* 39 (2012). *Laser Assisted Net shape Engineering* 7 (LANE 2012), pp. 439 –446. URL: <https://www.sciencedirect.com/science/article/pii/S1875389212025862>.
- [32] Karolien Kempen et al. 'Microstructural analysis and process optimization for selective laser melting of AlSi10Mg'. In: *Solid Freeform Fabrication Symposium Proceedings* (2011). Conference paper, pp. 484–495. URL: <https://sffsymposium.engr.utexas.edu/Manuscripts/2011/2011-37-Kempen.pdf>.
- [33] L.P. Lam et al. 'Phase analysis and microstructure characterisation of AlSi10Mg parts produced by Selective Laser Melting'. In: *Virtual and Physical Prototyping* 10 (2015), pp. 207–215. URL: <https://www.tandfonline.com/doi/full/10.1080/17452759.2015.1110868>.
- [34] K.-H. Leitz et al. 'Multi-physical simulation of selective laser melting'. In: *Metal Powder Report* 72.5 (2017), pp. 331–338. URL: <http://www.sciencedirect.com/science/article/pii/S0026065716300200>.
- [35] Wei Li et al. 'Effect of heat treatment on AlSi10Mg alloy fabricated by selective laser melting: Microstructure evolution, mechanical properties and fracture mechanism'. In: *Materials Science and Engineering: A* 663 (2016), pp. 116 –125. URL: <http://www.sciencedirect.com/science/article/pii/S0921509316303033>.
- [36] Xiao Peng Li et al. 'Tailoring Commercially Pure Titanium Using Mo₂C During Selective Laser Melting'. In: *Solid Freeform Fabrication 2017: Proceedings of the 28th Annual International* (Aug. 2017). Conference paper, pp. 160–166. URL: <https://lirias2repo.kuleuven.be/bitstream/handle/123456789/603230/TailoringCommerciallyPureTitaniumUsingMo2Cdu.pdf;jsessionid=B4F612E23F2E71C694B54B386?sequence=1>.

- [37] X.P. Li et al. 'The role of a low-energy-density re-scan in fabricating crack-free Al85Ni5Y6Co2Fe2 bulk metallic glass composites via selective laser melting'. In: *Mater. Des.* 63 (2014), 407–411. URL: https://www.researchgate.net/publication/263968566_The_role_of_a_low-energy-density_re-scan_in_fabricating_crack-free_Al85Ni5Y6Co2Fe2_bulk_metallic_glass_composites_via_selective_laser_melting.
- [38] Rene Lippert and Roland Lachmayer. 'A Design Method for SLM-Parts Using Internal Structures in an Extended Design Space'. In: (Sept. 2018), pp. 14–23. URL: https://www.researchgate.net/publication/319509485_A_Design_Method_for_SLM-Parts_Using_Internal_Structures_in_an_Extended_Design_Space.
- [39] Bochuan Liu et al. 'Investigazition the effect of particle size distribution on processing parameters optimisation in selective laser melting process'. In: (Jan. 2011). Conference paper, pp. 227–238.
- [40] Los Alamos National Laboratory - *The Contour Method for Measuring Residual Stress*. URL: <http://www.lanl.gov/contour/> (visited on 28/05/2018).
- [41] Materialise - Aluminum (AlSi10Mg). URL: <http://www.materialise.com/en/manufacturing/materials/aluminum> (visited on 14/05/2018).
- [42] MechaniCalc - *Material Stress-Strain Curve*. URL: <https://mechanicalc.com/calculators/material-stress-strain-curve/> (visited on 09/05/2018).
- [43] Anne Mertens et al. 'Thermal Treatments of AlSi10Mg Processed by Laser Beam Melting'. In: *Proceedings of the 26th International Solid Freeform Fabrication Symposium*. Austin, TX, 2015, pp. 1007–1016.
- [44] Anne I. Mertens, Jocelyn Delahaye and Jacqueline Lecomte-Beckers. 'Fusion-Based Additive Manufacturing for Processing Aluminum Alloys: State-of-the-Art and Challenges'. In: *Advanced Engineering Materials* 19.8 (2017), p. 1700003. URL: <https://onlinelibrary.wiley.com/doi/abs/10.1002/adem.201700003>.
- [45] Todd M. Mower and Michael J. Long. 'Mechanical behavior of additive manufactured, powder-bed laser-fused materials'. In: *Materials Science and Engineering: A* 651 (2016), pp. 198 –213. URL: <http://www.sciencedirect.com/science/article/pii/S092150931530530X>.
- [46] OHSU - *Inductively Coupled Plasma Mass Spectrometry*. 2018. URL: <https://www.ohsu.edu/xd/research/research-cores/elemental-analysis/about/icp-ms.cfm> (visited on 02/06/2018).
- [47] P.C. Paris et al. 'Stresses and crack tip stress intensity factors around spherical and cylindrical voids and inclusions of differing elastic properties and with misfit sizes'. In: (Jan. 2009), pp. 485–502. URL: https://www.researchgate.net/publication/293181115_Stresses_and_crack_tip_stress_intensity_factors_around_spherical_and_cylindrical_voids_and_inclusions_of_differing_elastic_properties_and_with_misfit_sizes.
- [48] K.G. Prashanth, S. Scudino and J. Eckert. 'Defining the tensile properties of Al-12Si parts produced by selective laser melting'. In: *Acta Materialia* 126 (2017), pp. 25 –35. URL: <http://www.sciencedirect.com/science/article/pii/S135964541630982X>.
- [49] K.G. Prashanth et al. 'Microstructure and mechanical properties of Al-12Si produced by selective laser melting:Effect of heat treatment'. In: *Mater. Sci. Eng. A* 590 (2014), pp. 153–160. URL: <https://www.sciencedirect.com/science/article/pii/S0921509313011180>.

- [50] Noriko Read et al. 'Selective laser melting of AlSi10Mg alloy: Process optimisation and mechanical properties development'. In: *Materials & Design* (1980-2015) 65 (2015), pp. 417–424. URL: <http://www.sciencedirect.com/science/article/pii/S0261306914007468>.
- [51] Renishaw plc, *AlSi10Mg-0403 powder for additive manufacturing data sheet*. 2015. URL: <http://resources.renishaw.com/en/download/data-sheet-alsi10mg-0403-400-w-powder-for-additive-manufacturing--73122> (visited on 15/04/2018).
- [52] Idan Rosenthal, Adin Stern and Nachum Frage. 'Microstructure and Mechanical Properties of AlSi10Mg Parts Produced by the Laser Beam Additive Manufacturing (AM) Technology'. In: *Metallogr. Microstruct. Anal.* 3 (2014), 448–453. URL: <https://link.springer.com/article/10.1007/s13632-014-0168-y>.
- [53] Idan Rosenthal, Adin Stern and Nachum Frage. 'Strain rate sensitivity and fracture mechanism of AlSi10Mg parts produced by Selective Laser Melting'. In: *Mater. Sci. Eng. A* 682 (2017), 509–517. URL: <https://www.sciencedirect.com/science/article/pii/S0921509316314344>.
- [54] Alessandro Salmi et al. 'Experimental analysis of residual stresses on AlSi10Mg parts produced by means of Selective Laser Melting (SLM)'. In: *10th CIRP Conference on Intelligent Computation in Manufacturing Engineering - CIRP ICME '16*. Vol. 62. 2017, pp. 458–463.
- [55] Sartorius AG, *Sartorius BP121S Installation And Operating Instructions Manual*. 2000. URL: <https://www.manualslib.com/products/Sartorius-Bp121s-3748053.html> (visited on 15/04/2018).
- [56] Ming Tang, P. Chris Pistorius and Jack L. Beuth. 'Prediction of lack-of-fusion porosity for powder bed fusion'. In: *Additive Manufacturing* 14 (2017), pp. 39–48. URL: <http://www.sciencedirect.com/science/article/pii/S2214860416300471>.
- [57] Lore Thijss et al. 'Fine-structured aluminium products with controllable texture by selective laser melting of pre-alloyed AlSi10Mg powder'. In: *Acta Materialia* 61 (2013), 1809–1819. URL: <https://www.sciencedirect.com/science/article/pii/S1359645412008592?via%3Dihub>.
- [58] Total Materia - Heat treating of aluminum and aluminum alloys. URL: <https://www.totalmateria.com/page.aspx?ID=CheckArticle&site=ktn&NM=7> (visited on 30/05/2018).
- [59] U. Tradowsky et al. 'Selective laser melting of AlSi10Mg: Influence of post-processing on the microstructural and tensile properties development'. In: *Mater. Des.* 105 (2016), 212–222. URL: <https://www.sciencedirect.com/science/article/pii/S0264127516306712?via%3Dihub>.
- [60] F. Trebuna et al. *Fine-structured aluminium products with controllable texture by selective laser melting of pre-alloyed AlSi10Mg powder*. 2008. URL: <https://hrcak.srce.hr/file/30578> (visited on 14/05/2018).
- [61] Francesco Trevisan et al. 'On the Selective Laser Melting (SLM) of the AlSi10Mg Alloy: Process, Microstructure, and Mechanical Properties'. In: 10 (Jan. 2017), pp. 1–23. URL: <https://www.ncbi.nlm.nih.gov/pmc/articles/PMC5344617/>.
- [62] Naor Elad Uzan et al. 'Fatigue of AlSi10Mg specimens fabricated by additive manufacturing selective laser melting (AM-SLM)'. In: *Materials Science and Engineering: A* 704 (2017), pp. 229–237. URL: <http://www.sciencedirect.com/science/article/pii/S0921509317310316>.

- [63] M. Vashista and S. Paul. 'Correlation between full width at half maximum (FWHM) of XRD peak with residual stress on ground surfaces'. In: *Philosophical Magazine* 92.33 (2012), pp. 4194–4204. URL: https://www.researchgate.net/publication/287922828_Correlation_between_full_width_at_half_maximum_FWHM_of_XRD_peak_with_residual_stress_on_ground_surfaces.
- [64] Bey Vrancken. 'Study of Residual Stresses in Selective Laser Melting'. PhD thesis. KU Leuven, 2016.
- [65] Lianfeng Wang et al. 'Investigation of Performance and Residual Stress Generation of AlSi10Mg Processed by Selective Laser Melting'. In: *Advances in Materials Science and Engineering* 2018 (2018), pp. 1 –12. URL: <https://www.hindawi.com/journals/amse/2018/7814039/ref/>.
- [66] Ruyao Wang and Weihua Lu. 'Direct electrolytic Al–Si alloys (DEASA)—an undercooled alloy self-modified structure and mechanical properties'. In: *Electrolysis* (2012), pp. 107–140. URL: <https://www.intechopen.com/books/electrolysis/direct-electrolytic-al-si-alloys-deasa-an-undercooled-alloy-self-modified-structure-and-mechanical-p>.
- [67] Robert C Weast. *CRC Handbook of Chemistry and Physics 53rd Edition*. CRC Press, 1973. URL: <http://jupiter.plymouth.edu/~jsduncan/courses/2012-Spring/Techniques/Exams/DensityOfWater-vs-Temp.pdf>.
- [68] Christian Weingarten et al. 'Formation and reduction of hydrogen porosity during selective laser melting of AlSi10Mg'. In: *Journal of Materials Processing Technology* 221 (2015), pp. 112 –120. URL: <http://www.sciencedirect.com/science/article/pii/S0924013615000564>.
- [69] XRF Scientific - *What is ICP Spectroscopy?* 2015. URL: <https://www.xrfscientific.com/what-is-icp-spectroscopy/> (visited on 02/06/2018).
- [70] Chor Yen Yap et al. 'Review of selective laser melting: Materials and applications'. In: 2 (Dec. 2015), p. 041101. URL: https://www.researchgate.net/publication/286497734_Review_of_selective_laser_melting_Materials_and_applications.
- [71] Yan Zhou et al. 'Investigation on the scan strategy and property of 316L stainless steel-Inconel 718 functionally graded materials fabricated by selective laser melting'. In: *The Proceedings of the 26th Solid Freeform Fabrication Symposium* (Aug. 2015). Conference paper, pp. 700–707. URL: https://www.researchgate.net/publication/284260951_Investigation_on_the_scan_strategy_and_property_of_316L_stainless_steel-Inconel_718_functionally_graded_materials_fabricated_by_selective_laser_melting.